Strojniški vestnik

Journal of Mechanical Engineering

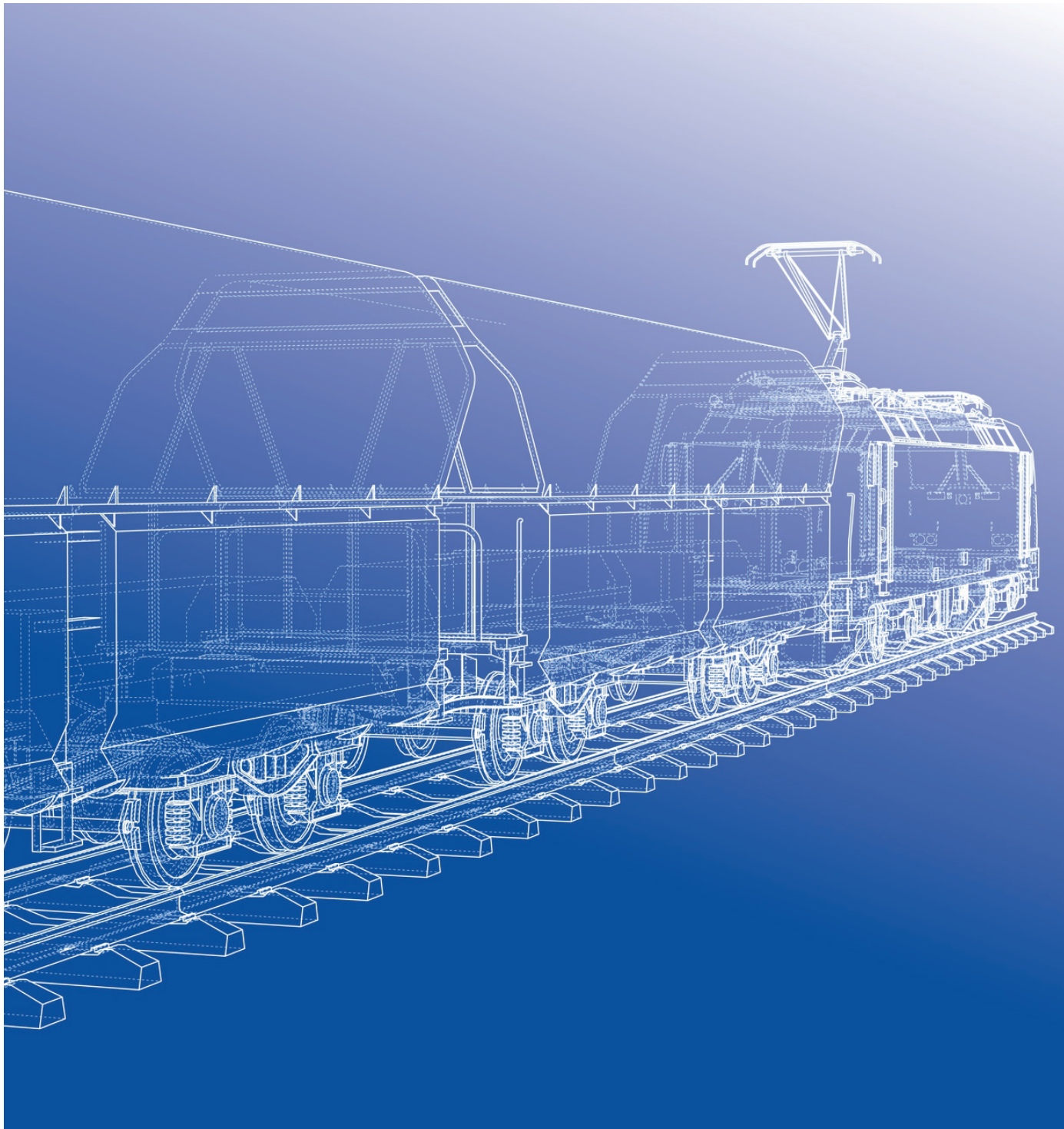

VOL 71 ▪ NO 11-12 ▪ Y 2025

Strojniški vestnik – Journal of Mechanical Engineering (SV-JME)

Aim and Scope
The international journal publishes original and (mini)review articles covering the concepts of materials science, mechanics, kinematics, thermodynamics, energy and environment, mechatronics and robotics, fluid mechanics, tribology, cybernetics, industrial engineering and structural analysis.
The journal follows new trends and progress proven practice in the mechanical engineering and also in the closely related sciences as are electrical, civil and process engineering, medicine, microbiology, ecology, agriculture, transport systems, aviation, and others, thus creating a unique forum for interdisciplinary or multidisciplinary dialogue.
The international conferences selected papers are welcome for publishing as a special issue of SV-JME with invited co-editor(s).

Editorial Office:
University of Ljubljana, Faculty of Mechanical Engineering
SV-JME, Aškerčeva 6, 1000 Ljubljana, Slovenia
Phone: +386 (0)1 4771 137
info@sv-jme.eu, http://www.sv-jme.eu

Technical Editor: Pika Škraba

Print: Grafika Gracer d.o.o. printed in 190 copies

President of Publishing Council:
Jernej Klemenc
University of Ljubljana, Faculty of Mechanical Engineering, Slovenia

Vice-President of Publishing Council:
Matej Vesenjak
University of Maribor, Faculty of Mechanical Engineering, Slovenia

Founders and Publishers:
University of Ljubljana, Faculty of Mechanical Engineering, Slovenia
University of Maribor, Faculty of Mechanical Engineering, Slovenia
Association of Mechanical Engineers of Slovenia
Chamber of Commerce and Industry of Slovenia,
Metal Processing Industry Association

Founding Editor:
Bojan Kraut
University of Ljubljana, Faculty of Mechanical Engineering, Slovenia

ISSN 0039-2480, ISSN 2536-2948 (online)

General information:
Strojniški vestnik – Journal of Mechanical Engineering is published in 6 double issues per year.

Institutional prices include print & online access: institutional subscription price and foreign subscription €100,00 (the price of a single issue is €20,00); general public subscription and student subscription €50,00 (the price of a single issue is €10,00). Prices are exclusive of tax. Delivery is included in the price. The recipient is responsible for paying any import duties or taxes. Legal title passes to the customer on dispatch by our distributor. Single issues from current and recent volumes are available at the current single-issue price. To order the journal, please complete the form on our website. For submissions, subscriptions and all other information please visit: *http://www.sv-jme.eu.*

You can advertise on the inner and outer side of the back cover of the journal. The authors of the published papers are invited to send photos or pictures with short explanation for cover content.

Every manuscript submitted to the SV-JME undergoes a peer-review process. We would like to thank the reviewers who have taken part in the peer-review process. SV-JME is indexed / abstracted in: SCI-Expanded, Compendex, Inspec, ProQuest-CSA, SCOPUS, TEMA. The list of the remaining bases, in which SV-JME is indexed, is available on the website.

The journal is subsidized by Slovenian Research and Inovation Agency.

Strojniški vestnik - Journal of Mechanical Engineering is available on *https://www.sv-jme.eu*.

Contents

Strojniški vestnik - Journal of Mechanical Engineering
Volume 71, (2025), Number 11-12
Ljubljana, November - December 2025
ISSN 0039-2480
Published every two months

ON THE COVER
We open with a striking technical drawing of a train, which is an emblem of engineering precision and motion. This issue starts with an article examining the dynamic performance of the C80 railway wagon, focusing on the influence of wheel polygons and the typical mode shapes of the car body. The second contribution presents a two-stage optimal design methodology for metro underframe structures, uniting topology, size, and shape optimization. Together, these works showcase cutting-edge approaches that advance safety, efficiency, and structural excellence in modern rail transport. Following this topic, the issue continues with a selection of further engaging and insightful contributions.

Image courtesy: iStock.com, credit: cherezoff

Dynamic Performance of C80 Railway Wagon Under the Influence of Wheel Polygons and Typical Mode Shapes of the Car Body

Yuru Li[1,2] ✉ – Gangjian Zhou[2] – Xiangwei Li[1] – Tao Zhu[3] – Shangchao Zhao[1] – Chunlei Zhao[1] – Junke Xie[2] – Shoune Xiao[3]

[1] CRRC Qiqihar Rolling Stock Co., Ltd., China
[2] Henan University of Science and Technology, College of Vehicle and Traffic Engineering, China
[3] Southwest Jiaotong University, State Key Laboratory of Rail Transit Vehicle System, China

✉ lyr@haust.edu.cn

Abstract *To investigate the influence of typical mode shapes and wheel polygons on the dynamic characteristics of railway freight car body, this study takes railway freight wagon C80 as the research object. Vehicle-level and system-level finite element models of the C80 railway wagon were developed, revealing that the lateral and vertical stiffness of railway freight cars significantly affects system mode. Furthermore, co-simulation using NASTRAN and SIMPACK was used to establish a fully flexible dynamic model of the C80 wagon. The influence of typical modal frequencies on the dynamic performance of the wagon was analyzed considering the wheel polygon and wear parameters. The results show that suppressing the torsional mode shape of the railway wagon reduces its impact on the derailment coefficient, wheel load reduction rate, axle transverse force and overturning coefficient by over 40 %. When the train speed corresponds to the polygon order, the wheel load reduction rate increases with the polygon wear depth under both the 10th order and 18th order conditions, by as much as 14.4 % when wear depth increases from 0.01 mm to the 0.05 mm for the 18th order condition. In addition, under the 6th order, 10th order, 16th order and 18th order polygon conditions, suppressing the torsional mode notably increased the wheel load reduction rate, especially under the 6th order polygon condition. This research provides valuable guidance for optimizing suspension parameters and controlling polygonal wear in railway wagons, offering a guiding basis for enhancing their dynamic performance of railway wagons.*

Keywords *full flexibility, C80 railway wagon, dynamic models, wheel polygons suspension parameters*

Highlights

- *Built first fully flexible C80 wagon model via Nastran–Ansys co-simulation.*
- *FE results show lateral/vertical stiffness strongly affects wagon system modes.*
- *Findings guide suspension design and help control wear, boosting dynamic performance.*

1 INTRODUCTION

The polygonization of railway wagon wheels (the periodic non-roundness of the wheelset) aggravates the impact of wheels and rails, resulting in increased vibration, noise, and fatigue damage of components, and even posing potential safety risks. At the same time, the suspension parameters of the running part, including spring rate, damping coefficient and positioning stiffness, directly affect the running smoothness of railway wagons, curving abilities, and wheel-rail interaction. Therefore, it is necessary to conduct a systematic study on the combined influence of wheel polygonization and suspension parameters on dynamic performance of railway wagons.

The polygonal wear of railway vehicles is essentially a periodic irregularity resulting from uneven circumference wear, typically with an order number between 1 and 30, and a wave depth of approximately 1 mm [1]. This phenomenon excites the bogie through wheel-rail contact, reduces the fatigue life of components, and deteriorates the dynamic performance of the train [2]. Therefore, the polygon wear of the wheels has become a persistent long-term issue in railway operation. Extensive research—both experimental and theoretical—has been conducted to investigate the formation mechanisms and dynamic effects of wheel polygonization. Li et al. [3] systematically analyzed its impact on the running stability of the vehicle through field measurement and numerical simulation, revealing that for polygon orders of 1 to 10 with a wave depth of 0.2 mm, the critical speed drops to just 61 km/h, significantly affecting stability. Tao et al. [4] and Cai et al. [5] studied the 6th to 8th order polygon wear in metro vehicles traveling at 70 km/h and identified the wheel-rail P2 force as the root cause of polygon formation. Yang et al. [6] used the rigid-flexible coupling model. They found that considering wheelset and track elasticity and applying multi-cut re-profiling technology effectively reduces flange polygon wear in heavy-haul trains. Recently, Jin et al. [7] highlighted the emergence of high-order wheel polygons, whose associated high-frequency vibrations accelerate fatigue damage in bogies and track components. Zhou et al. [8] proposed that the 4th order bending resonance of the wheelset was the main reason for the 20th order polygon wear, considering the non-Hertz contact and track irregularities. Johansson and Nielsen [9] as well as Johansson and Andersson [10] identified the vertical anti-resonance of the track at 165 Hz as the main reason in the growth of 14th to 20th order polygon wheel roughness. Similarly, Ye et al [11] and Yang et al. [12] showed through modal and dynamic simulation analyses that the rail B3 mode induces resonance in the wheel-rail system, driving the high-order polygonization. Wu et al. [13] confirmed experimentally that the coupling resonance of the framework plays a key role in the forming higher-order polygons.

Additional studies linked polygonal wear to fatigue damage in vehicle components. Fu et al. [14] identified low-frequency wheel-rail impacts as the cause of fatigue cracks in the bogie frame. Wang et al. [15] found that the rail corrugations combined with wheel polygons was the main contributor of fatigue damage of the bogie

frame. Liu et al. [16], Song et al. [17] and Wu et al. [18] using rigid-flexible coupling dynamics models, demonstrated the wheel polygons produce large fluctuations in wheel-rail interaction forces, where short-wavelength components excite high-frequency vibrations in rails and sleepers. Barke et al. [19] analyzed in detail their adverse on both vehicle components and track systems. Zhang et al. [20] found that high-order wheel polygons with the equivalent roughness generate stronger wheel-rail noise and internal noise, reducing passenger comfort.

The suspension system of railway vehicle, comprising primary and secondary suspension, also plays a crucial role in dynamic properties of vehicles. Thomas et al. [21] studied and verified the effects of suspension, curve settings, and track defects on vehicle traverse and roll angle. Park et al. [22] studied the effects of suspension system, wheel-rail creep coefficient, and track excitation on vehicle lateral stability. Based on the rigid-flexible coupling dynamic model considering the flexibility of the frame, Ma et al. [23] considered frame flexibility and demonstrated that non-diagonal spring stiffness greatly affects curve-passing speed. Guan et al. [24] found that reducing wheelset mass and inertia while increasing suspension stiffness and damping improves the critical speed of the hunting motion. Xiao et al. [25] used UM software to analyze CRH2 EMU dynamics and found that the vertical and lateral stiffness of the primary springs and damping of the secondary transverse shock absorbers dominate the vibration response. Lei et al. [26] used SIMPACK to assess a subway vehicle performance, showing that the influence of a series of suspension longitudinal and lateral stiffness on the nonlinear critical velocity first increases and then decreases. Mousavi Bideleh et al. [27] emphasizes that optimized suspension parameters can effectively reduce wheel and rail wear and enhance driving safety.

To broaden the scope of the literature review and strengthen the scientific context, it is essential to include research addressing the structural behavior and optimization of railway vehicles based on their dynamic behavior, particularly focusing on bogie frames and car bodies, which share many dynamic interaction aspects with the C80 freight wagon analyzed in this study. As the primary interface between vehicle and track, the railway bogie plays a critical role in transmitting and distributing loads arising from track irregularities and operational dynamics. Several studies have investigated bogie frame design through structural and topological optimization combined with dynamic analysis, highlighting that geometry, stiffness distribution, and material selection substantially influence fatigue life, vibration response, and stability [28-31]. The car body, as the primary load-bearing structure of the railway vehicle, has been extensively studied not only in terms of its mechanical strength but also to its dynamic behavior, which plays a fundamental role in the overall performance and safety of freight wagons. Recent research emphasizes that the natural mode shapes of the car body, particularly lateral, vertical, and torsional vibrations, significantly influence key dynamic parameters such as derailment coefficients, axle forces, and wheel wear. In particular, investigations on the C80 freight car revealed that specific modal frequencies, together with wheel polygonal wear, can markedly affect the vehicle's dynamic response.

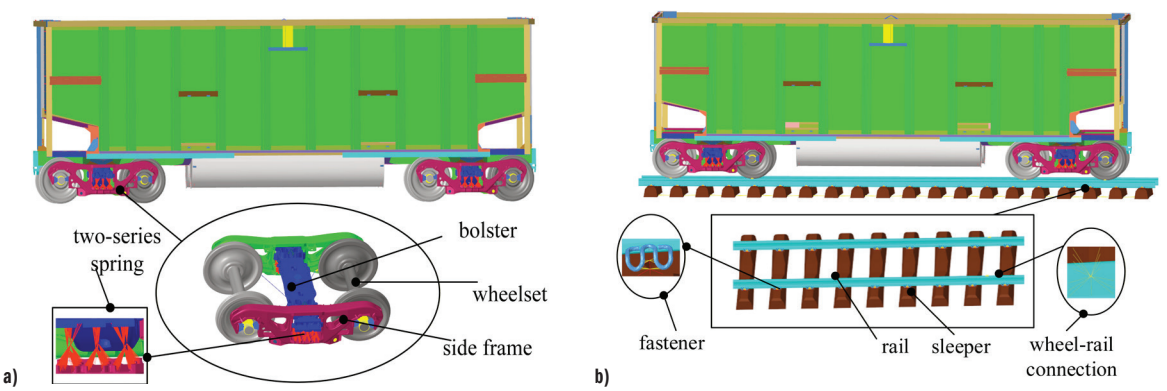

Fig. 1. Construction of the finite element model of the C80 railway wagon; a) vehicle-level C80 railway freight car, and b) system-level C80 railway freight car

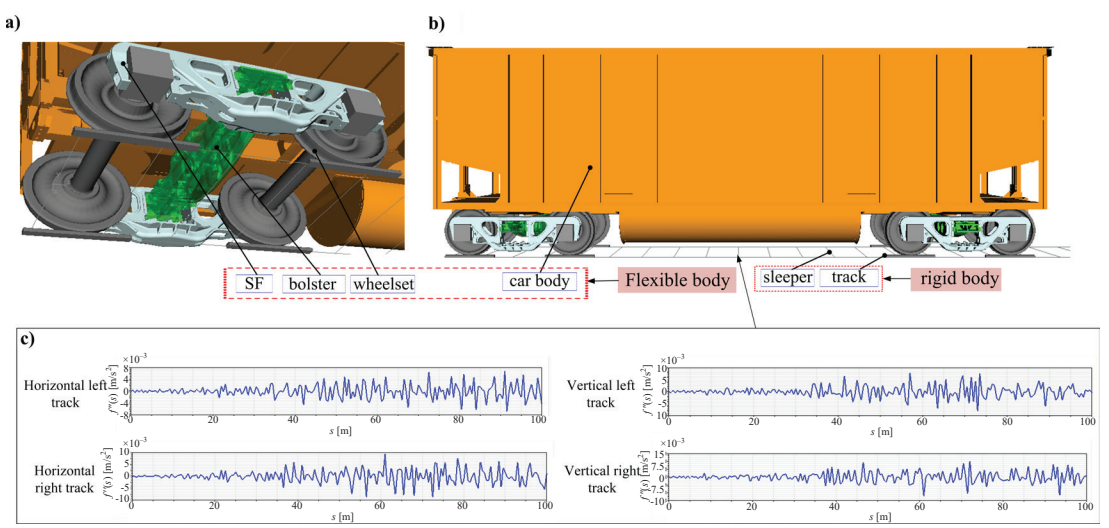

Fig. 2. A fully flexible model of the C80 railway wagon; a) partial enlarged view of the running section, b) fully flexible model of the C80railway wagon, and c) orbital spectral excitation

Through detailed finite element modeling and advanced co-simulation methods, these studies demonstrate that controlling or suppressing certain torsional mode shapes can lead to substantial improvements in dynamic stability and reductions in critical dynamic loads. Within this context, incorporating the dynamic modal characteristics of the car body into structural design provide a valuable perspective, as it offers an important complement to traditional approaches focused primarily on structural optimization and weight reduction, ultimately contributing directly to safer and more efficient freight vehicle designs [32-35]. Comparative analyses between conventional and modern lightweight materials show that tailored material-structure combination can achieve an optimal balance between mass reduction and dynamic performance, offering insights directly applicable to freight wagon design. Zhou et al. [36] and Yu et al. [37] studied the vibration responses of railway vehicles and provided an effective reference for the preliminary design of secondary suspension of railway vehicles.

The above studies show that wheel polygonization, together with the parameters of the first-series and two-series suspension, have an important impact on the dynamic performance of the vehicle system. However, research specifically addressing the interaction between first-series suspension parameters and typical modes in the dynamic performance of railway wagons remains insufficient and requires further investigation. In this paper, the modal characteristics of the C80 wagon are analyzed by developing both vehicle-level and system-level finite element models. The effects of first-series and second-series suspension parameters on the modal frequencies are examined, and the corresponding typical mode shapes most relevant to dynamic behavior are identified.

2 METHODS

Taking the C80 railway wagon as the research object, which consists of four primary components: the car body, side frame, rocker and wheelset, as shown in Fig. 1, vehicle-level and system-level C80 railway wagon finite element models are established using finite element software.

Firstly, finite element models of the car body, bolster, and side frame (SF) were established in NASTRAN, and both BDF and OP2 files were generated. These files were then imported into SIMPACK to generate the FBI file containing the modal and stiffness information. Based on this data, a dynamic model of the railway wagon was established in SIMPACK. The flexible car body, bolster, wheelset, and side frame were subsequently imported to replace the rigid counterparts, resulting in a fully flexible dynamic model of the railway wagon on a rigid track, as shown in Fig. 2b. Figure 2a presents a partially enlarged view of the running section of the C80 railway wagon, while Fig. 2c shows the orbital spectral excitation used in simulation. The vehicle model assumes a fixed wheelbase of 8.2 m, an axle load of 25 t, and a total load of 80 t.

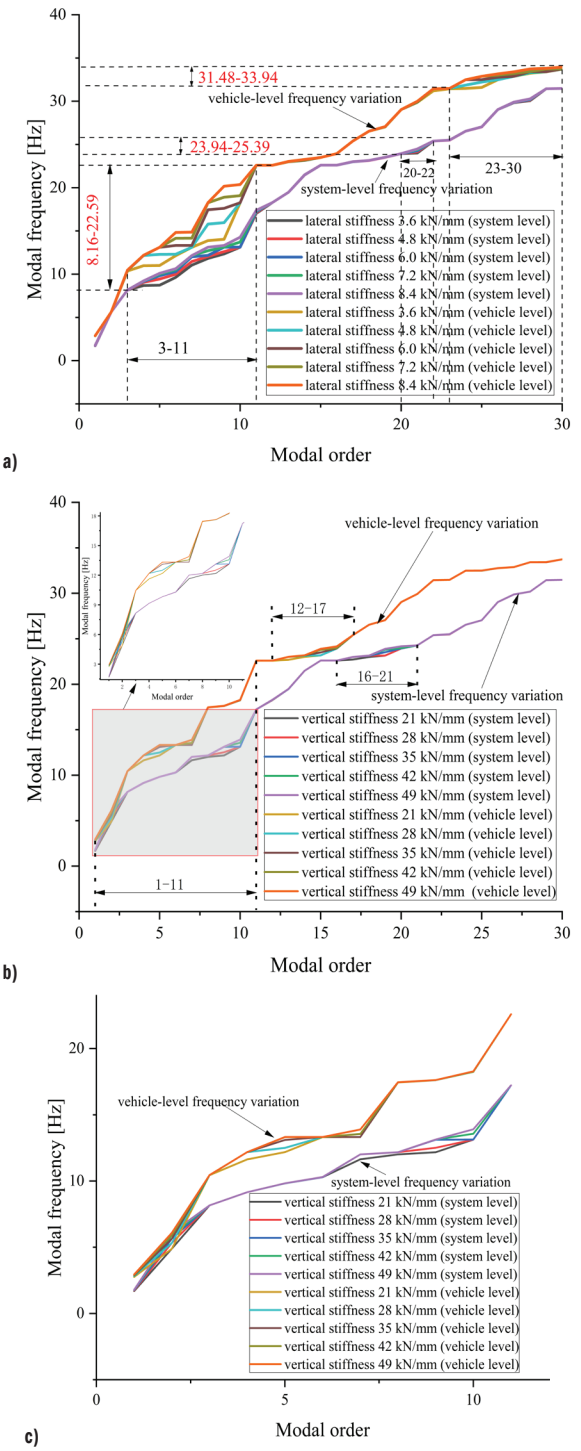

Fig. 3. Variation of mode attitude frequency under different: a) transverse stiffnesses, b) vertical stiffnesses, and c) local diagram of vertical stiffness

3 RESULTS AND DISCUSSION

3.1 Influence of a Series of Lateral and Vertical Stiffness

To analyze the influence of first-series lateral and vertical stiffnesses on the system modal frequency, parametric variations were introduced based on the original lateral stiffness of 6 kN/mm and vertical stiffness of 35 kN/mm. A variation range of ±40 % was applied. Accordingly, the lateral stiffness was set to 3.6 kN/mm, 4.8 kN/mm, 7.2 kN/mm, and 8.4 kN/mm, while the vertical stiffness was varied to 21 kN/mm, 28 kN/mm, 42 kN/mm, and 49 kN/mm. For each stiffness configuration, the first 30 modal frequencies were obtained through vehicle-level, system, and finite element calculations and were compared with the modal frequencies of the initial lateral and vertical stiffness. The comparison results are shown in Fig. 3.

As shown in Fig. 3a, both the vehicle-level and the system-level modal frequency increase with the rise in lateral stiffness, particularly in the 3rd to 11th order, where the changes are the most pronounced. At higher modal orders, the system-level frequencies show noticeable variation only in the 20th to 22nd order, while the vehicle-level modal frequency exhibit changes mainly in the 23rd to 30th modes. In these ranges, the modal frequencies increase respectively from 8.16 Hz to

22.59 Hz, 23.94 Hz to 25.39 Hz, and 31.48 Hz to 33.94 Hz, indicating that the modal frequencies within these three segment ranges are highly sensitive to changes in lateral stiffness. Similarly, Fig. 3b shows that both vehicle-level and system-level modal frequencies increase with vertical stiffness in the 1st to 11th order range, and the modal frequency rise from 1.79 Hz to 17.22 Hz. Sensitivity to vertical stiffness also appears in the mid-order modes: the 12th to 17th vehicle level modes and the 16th to 21st modal frequencies increase from 22.59 Hz to 25.39 Hz and from 22.6 Hz to 24.28 Hz, respectively. This indicates that modal frequencies in these three-segment range are strongly sensitive to changes in vertical stiffness. Overall, the first series of lateral and vertical stiffness have a significant influence on the modal frequency of the system, and thus the modal frequencies associated with the typical vibration modes of both the railway wagon and the railway freight car can be effectively adjusted by changing the suspension parameters of the first series.

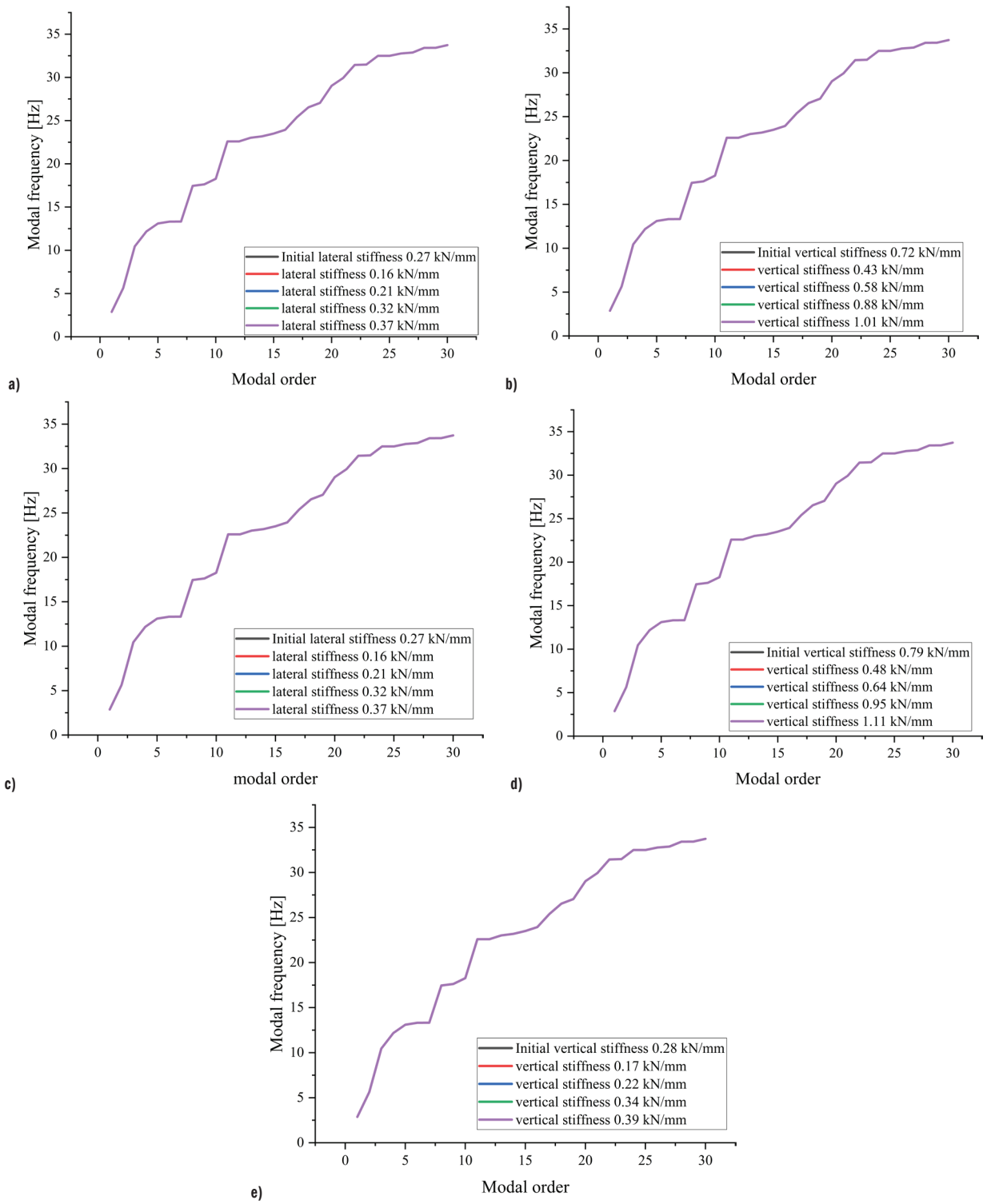

Fig. 4. Comparison with initial stiffness; a) transverse stiffness of the middle pillow spring, b) vertical stiffness of the middle pillow spring, c) transverse stiffness of the hinge spring, d) vertical stiffness of hinge springs, and e) vertical stiffness of damping springs

3.2 Effect of Bi-Series Transverse and Vertical Stiffness on Modal Frequency

To analyze the influence of the lateral and vertical stiffness of the spring and hinge, as well as the vertical stiffness of the damping spring, on the system's modal characteristics, a parametric study was conducted based on the C80 finite element model. In the baseline model, the lateral and vertical stiffness of the spring and hinge set to 0.27 kN/mm and 0.72 kN/mm, respectively, while the vertical stiffness of the damping spring was set to 0.28 kN/mm. For the sensitivity analysis, the lateral stiffness of the spring and hinge was varied at 0.16 kN/mm, 0.21 kN/mm, 0.32 kN/mm, and 0.37 kN/mm, while the vertical stiffness was set to 0.43 kN/mm, 0.58 kN/mm, 0.87 kN/mm, and 1.01 kN/mm. Additionally, the vertical stiffness of the damping spring was modified to 0.17 kN/mm, 0.22 kN/mm, 0.34 kN/mm, and 0.39 kN/mm. Through calculation, the modal frequencies and shapes of the first 30 modes were obtained, and the comparative results are shown in Fig. 4.

As shown in Fig. 4, the modal frequencies corresponding to different transverse and vertical stiffness values of the pillow spring, hinge spring, and damping spring were compared with those obtained under the initial stiffness parameters. The results indicate that, across all tested stiffness variations, the modal frequency changes remain below 1 %. This demonstrates that the lateral stiffness of the intermediate spring and hinge spring have a negligible influence on the system's modal frequency.

3.3 The Influence of Typical Mode Shapes on the Dynamic Performance of the Car Body

Through the measured excitation load of line loading as shown in Fig. 2c, the basic parameters of the railway wagon dynamic model were defined as follows: the car body load is 80 t, and the running speed is 70 km/h. For the first-series suspension, the stiffness values in the X, Y and Z directions are 3250 kN/m, 1500 kN/m, 8750 kN/m, respectively, while the corresponding damping values are 3250 Ns/m, 1500 Ns/m and 8750 Ns/m. For the second-series suspension, the stiffness values in the X, Y and Z directions are set to 0 kN/m, 0 kN/m, 460.45 kN/m and with all damping components set to 0 Ns/m. The rigid-flexible coupling dynamic model is solved using the Dell T7920 workstation with 10-core CPU parallel computation. Based on this configuration, the dynamic performance indices of the fully flexible C80 railway wagon, including derailment coefficient, wheel weight reduction rate, axle transverse force, and overturning coefficient, are obtained through dynamic simulation.

3.3.1 Effect of a Single Mode Shape on Dynamics

To quantify the influence of the typical mode shape of the car body on the dynamic performance of the railway wagon, the fully dynamic mode was used to analyze the influence of the primary modal for bending, torsion, and respiration. The dynamic performance index after the inhibition was compared with the initial dynamic performance index. The influence of different typical mode shapes on dynamic performance was then obtained. The comparison results are shown in Fig. 5.

As shown in Fig. 5a, suppressing different mode shapes has only a minimal effect on the derailment coefficient, and in all cases, the resulting values remain slightly lower than those in the initial (unsuppressed) state. In contrast, the effects of mode-shape suppression on the wheel load reduction rate varies significantly. Inhibition of the transverse bending and respiration mode shapes results in changes less than 1 %. However, the inhibition of torsional mode shapes leads to a pronounced increase, rising by 9.8 % to a value of 0.26 compared with the initial state. This finding highlights that torsional mode shapes play a dominant role in governing wheel load reduction rate behavior.

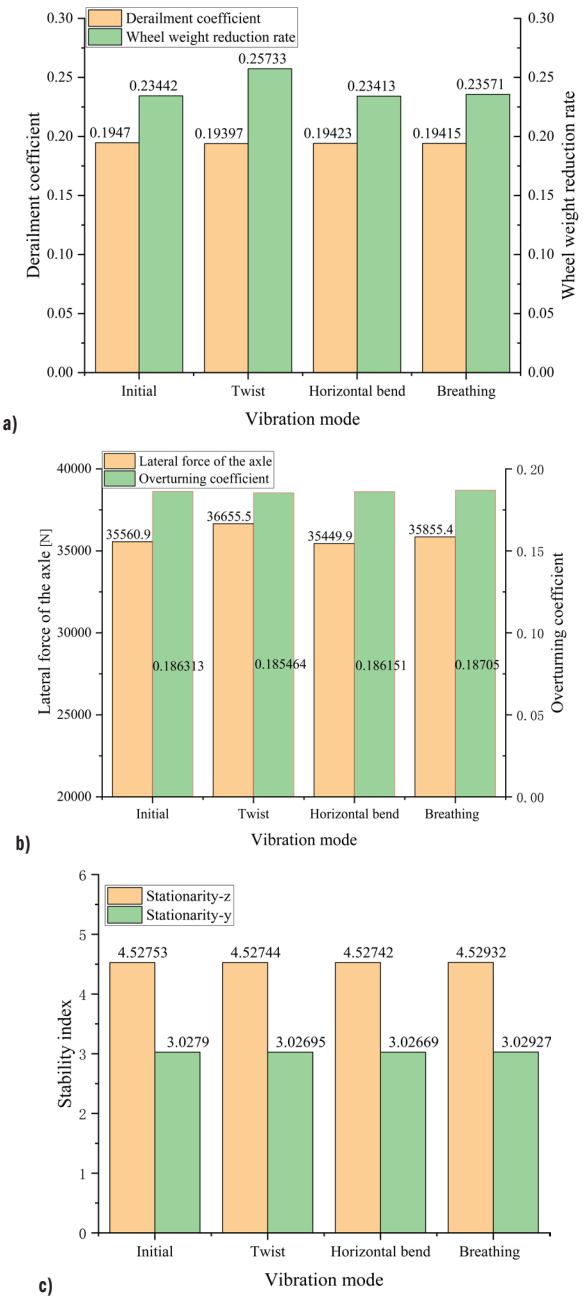

Fig. 5. Comparison of the dynamic performance of railway wagons; a) derailment coefficient and wheel weight reduction rate, b) axle transverse force and overturning coefficient, and c) stationarity index

For Fig. 5b, different mode shapes have a significant effect on the transverse force of the axle. When the torsional mode shape is inhibited, the transverse force increases sharply to 36.66 kN (peak value) when the torsional mode representing an increase of approximately 3 % compared with the initial conditions. In contrast, the transverse force of the inhibition transverse mode shape decreases to 35.45 kN, the lowest value among the four mode shapes and about 0.3 % below the initial value. Suppression of the breathing mode causes a slight increase to 35.86 kN, which remains about 2.2 % lower than the torsional mode shape. The appearance of its typical mode shapes helps to reduce the transverse force of the

axle, providing an important reference for improving the vibration control strategies of railway wagons. For the overturning coefficient, suppressing the various mode shapes results in only marginal influence compared with the initial one. For Fig. 5c, the variation of the lateral and vertical stationarity indexes of the railway wagon relative to the initial state is below 0.1 % for all three mode-shape suppression scenarios (torsional, transverse bending, and respiratory mode shapes). This indicates that the torsional, transverse bending, and breathing mode shapes on the stationarity of railway wagons exert only a minimal influence of heavy trains during the operation.

Table 1. Dynamical indicators of typical mode shapes affect the weights

Serial number	Dynamic index	Typical vibration mode [%]		
		Twist	Horizontal bend	Breathing
1	Derailment coefficient	41.83	31.32	26.85
2	Wheel weight reduction rate	93.58	1.15	5.27
3	Lateral force of the axle	72.97	7.4	19.63
4	Overturning coefficient	48.57	9.27	42.16
5	Stationarity-y	27.46	34.97	37.57
6	Stationarity-z	4.52	5.53	89.95

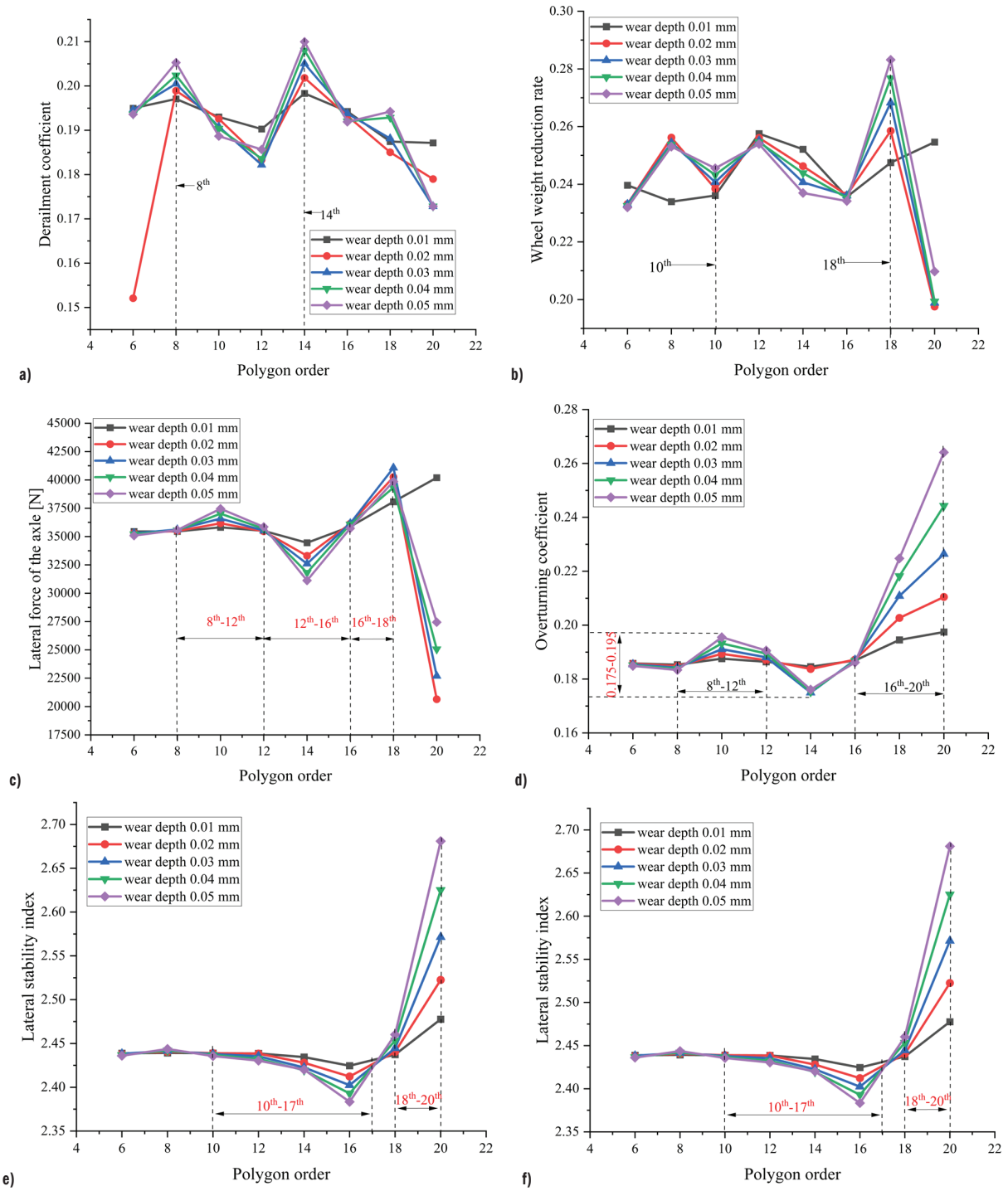

Fig. 6. Dynamic performance of railway wagons at different depths; a) derailment coefficient, b) wheel weight reduction rate, c) lateral force of the axle, d) overturning coefficient, e) lateral stability index, and f) vertical stability index

3.3.2 Typical Mode Shape Weighting Effects

To analyze the influence of the typical mode shapes of the C80 car body on the dynamic performance indexes, the torsional, lateral bending and respiration mode shapes were individually suppressed. The resulting variation rates of each dynamic performance index relative to the initial dynamic indicators were obtained. By normalizing these variation rates, the corresponding influence weights of three typical mode shapes under each dynamic metric were obtained, as shown in Table 1.

It is shown in Table 1, that the torsional mode shape exhibits the highest influence weights on the derailment coefficient, wheel weight reduction rate, axle transverse force and overturning coefficient, with corresponding values of 41.83 %, 93.58 %, 72.97 %, and 48.57 %, respectively. The lateral and vertical stationarity indexes are dominated by the respiratory mode shape, reaching 37.57 % and 89.95 %, respectively. Therefore, their influence must be carefully considered in structural design and suspension parameter optimization.

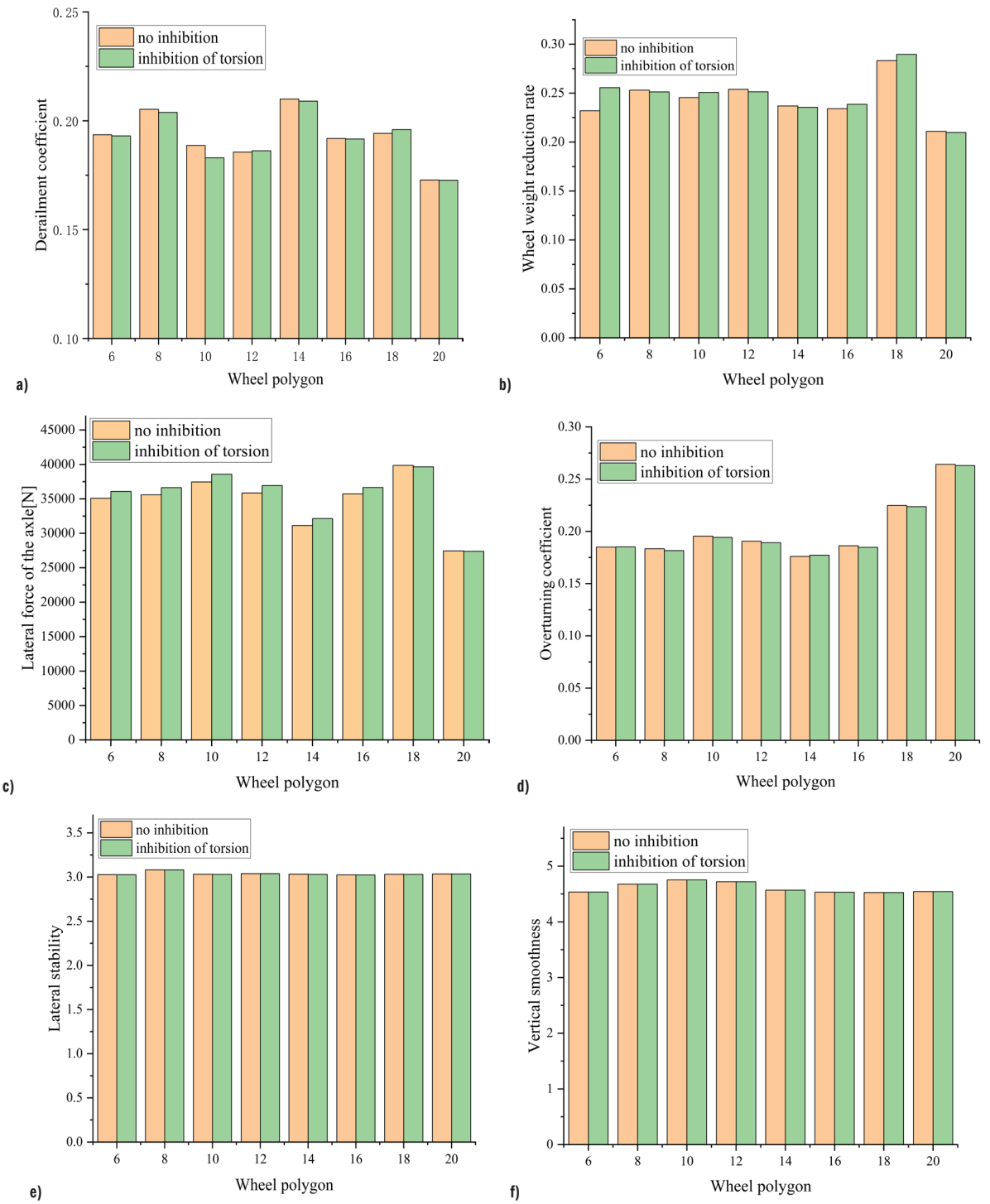

Fig. 7. Comparison of the dynamic performance of railway wagons with or without suppressed torsional mode shapes; a) derailment coefficient, b) wheel weight reduction rate, c) lateral force of the axle, d) overturning coefficient, e) lateral stability, and f) vertical smoothness

3.4 Effect of Wheel Polygons and Typical Mode Shapes on Dynamic Performance

3.4.1 Influence of Wheel Polygons

Based on the fully flexible dynamic model of the railway wagon, the dynamic performance of the heavy vehicle operating at a speed of 70 km/h on the straight track was studied. The 6th, 8th, 10th, 12th, 14th, 16th, 18th, and 20th order wheel polygons were introduced, with corresponding wear depths of 0.01 mm, 0.02 mm, 0.03 mm, 0.04 mm, and 0.05 mm. The simulation results for all condition are shown in Fig. 6.

As shown in Fig. 6a, when the vehicle speed and the polygon order remain constant, the derailment coefficient increases with increasing polygon wear depth under the 8th and 14th order conditions. These two polygon orders exert a more pronounced destabilizing effect on the derailment coefficient during the operation of heavy-haul railway, therefore, special attention should be given. For Fig. 6b, at the constant vehicle speed and wheel polygon order, the wheel weight reduction rate increases as the polygon wear depth grows, particularly under the 10th and 18th order conditions. The increase is especially significant for the 18th order condition, where the wear depth of 0.05 mm is 14.4 % higher compared with the wear depth of 0.01 mm. This finding highlights the necessity of controlling the wear depth to mitigate wheel load reduction rate.

For Fig. 6c, when the speed and the polygon order remain constant, the axle transverse force increases with the polygon wear depth at orders 8th to 12th and 16th to 18th. In contrast, the axle transverse force decreases as the polygon wear depth increases within the 12th to 16th order range, indicating that the axle transverse force is inhibited by the wear depth at the 12th to 16th order. As shown in Fig. 6d, when the vehicle speed and the wheel polygon order are constant, the overturning coefficient increases with the increase of the polygon wear depth for the 8th to 12th and 16th to 20th orders. This effect is especially pronounced for higher-order polygons: under the 20th order condition, the overturning coefficient at a wear depth 0.05 mm is 33.76 % higher than that at 0.01 mm. To ensure the operation safety of railway wagons, it is necessary to impose safety limits on the polygon abrasion depth under different working conditions.

From Fig. 6e, when the vehicle speed and polygon order remain constant, the lateral stationarity index decreases with increasing polygon wear depth for the 10th to 17th orders. In contrast, for the 18th to 20th polygon orders, the lateral stationarity index increases as the wear depth increases. This indicates that wear depth inhibits lateral stationarity index in the 10th to 17th orders, whereas for higher-order polygons (18th to 20th) excessive wear depth leads to a rapid deterioration of lateral stationarity. For Fig. 6f, when the vehicle speed and polygon order remain constant, the vertical (sag) stationarity index decreases with increasing polygon wear depth for the 9th to 16th order conditions. This trends indicate that the lateral stationarity index is relatively insensitive to wear depth within 9th to 16th order conditions.

3.4.2 Effect of Torsional Mode Shapes on Dynamic Performance

To analyze the dynamic performance under torsional mode-shape conditions, the influence of inhibiting and not inhibiting torsional mode shape were evaluated using the fully flexible railway wagon dynamic model. Wheel polygons of 6th, 8th, 10th, 12th, 14th, 16th, 18th and 20th orders were set, with a fixed wear depth of 0.05 mm and the running speed of 70 km/h. The resulting dynamic performance indices under both conditions were compared, and the comparison results are presented in Fig. 7.

As shown in Fig. 7a, the derailment coefficient remains below the safety limit of 1.0 regardless of whether the torsional mode shape is suppressed. In addition, the maximum variation increases by 3 % under the 10th order condition compared with the non-inhibition condition. This indicate that although the torsional mode shape does influence the derailment coefficient of the railway wagon, its overall effect remains limited. For Fig. 7b, the behavior of the wheel load reduction rate is strongly dependent on the relationship between the wheel polygon order and the torsional mode frequencies. At the 8th, 12th, 14th and 20th order polygon conditions, the characteristic frequencies are close to the torsional vibration mode frequencies. This suppresses the torsional vibration condition of the vehicle. Compared to the situation without suppression, the wheel load reduction rate decreases. Therefore, based on the wheel polygon, choosing to suppress the torsional vibration can reduce the wheel load reduction rate. After suppressing the torsional vibration at the 6th, 10th, 16th and 18th order, the vibration balance is disrupted. Compared to the situation without suppression, the wheel load reduction rate increases relative to the unsuppressed case. Especially in the 6th order condition, where suppression causes the wheel load reduction rate to rise by 9.85 %, indicating the significant impact of the wheel load reduction rate.

For Fig. 7c, except for the 18th and 20th order polygon conditions, the axle transverse force under torsional-mode suppression is greater than that without inhibition. Especially, under the 14th order condition, the transverse force increases by 3.3 %, indicating that the torsional mode shape has a measurable influence on the axle transverse force of railway wagons. As shown in Fig. 7d, except for the 6th and 14th order working conditions, the overturning coefficient of the inhibited torsional mode shape generally decreases. This indicates that torsional mode shape can effectively reduce the overturning coefficient of railway wagons. From Figs. 7e and the variations in both the lateral and vertical stationarity indexes remain below 1 % under the condition of inhibiting torsional mode shapes. This indicates that the torsional mode shapes exert only a minimal influence on the transverse and vertical stationarity indicators.

4 CONCLUSION

1. A modal finite element simulation model was established based on the C80 railway freight car. Both the vehicle-level modal frequency and the system-level modal frequency increase as the first series lateral and vertical stiffness increase. Across all conditions, the system-level modal frequency remains lower than the corresponding vehicle-level modal frequency.
2. When vehicle speed and wheel polygon order are fixed, in the 8th to 12th and 16th to 20th order working conditions, the overturning coefficient increases with the polygonal wear depth. Notably, the 0.05 mm abrasion depth in the 20th order working condition increases by 33.76% compared with the 0.01 mm abrasion depth. This demonstrates that the wheel polygon wear depth has a pronounced effect on overturning stability.
3. Suppressing torsional vibration mode for 8th, 12th, 14th and 20th wheel polygons reduces the wheel load reduction rate by 1 % compared with the unsuppressed case. This suggests that targeted torsional-mode control can improve wheel–rail load distribution for specific polygon orders. However, under the 6th order, 10th order, 16th order and 18th orders suppressing torsional mode increases the wheel weight reduction rate compared with that without inhibition, especially under the 6th order condition, where the wheel weight reduction rate increases by 9.85 %. This indicates that torsional mode shape can also deteriorate wheel weight reduction rate performance of railway wagons.

Collectively, the study on the dynamic performance of C80 railway freight cars under the influence of wheel polygon shapes and typical body vibration modes provides important engineering guidance highlighting the coupled influence of wheel polygonal wear and typical car-body vibration modes on derailment safety, wheel unloading behavior, and overall running stability.

References

[1] Nielsen, J.C.O., Johansson, A. Out-of-round railway wheels-a literature survey. *Proc Inst Mech Eng F-J Rail Rapid Transit* 214 79-91 (2000) **DOI:10.1243/0954409001531351**.

[2] Zhang, F., Wu, P., Wu, X., He, X., Zhang, M. et al. Analysis of the influence of polygons on axle boxes of high-speed train wheels. *J Vibr Measur Diagn* 38 1063-1068 (2018) **DOI:10.16450/j.cnki.issn.1004-6801.2018.05.029**. (in Chinese)

[3] Li, H., Li, L., Zhang, Y., Ye, C., Sun, Y., Yu, X., et al. Research on the influence of wheel profile wear coupled with wheel polygon on the dynamic response of vehicles. *J Railway Sci Eng* 21 4240-4252 (2024) **DOI:10.19713/j.cnki.43-1423/u.T20232081**. (in Chinese)

[4] Tao, G., Wen, Z., Liang, X., Ren, D., Jin, X. An investigation into the mechanism of the out-of-round wheels of metro train and its mitigation measures. *Vehic SystDynam* 57 1-16 (2019) **DOI:10.1080/00423114.2018.1445269**.

[5] Cai, W., Chi, M., Tao, G., Wu, G., Wu, X., Wen, Z. Experimental and numerical investigation into formation of metro wheel polygonalization. *Shock Vibr* 2019 1538273 (2019) **DOI:10.1155/2019/1538273**.

[6] Yang, Y., Chai, F., Liu, P., Ling, L., Wang, K., Zhai, W. On the polygonal wear evolution of heavy-haul locomotive wheels due to wheel/rail flexibility and its mitigation measures. *Chin J Mech Eng* 37 16 (2024) **DOI:10.1186/s10033-024-01001-z**.

[7] Jin, X., Wu, Y., Liang, S., Wen, Z., Wu, X., Wang, P. Characteristics, mechanism, influences and countermeasures of polygonal wear of high-speed train wheels. *J Mech Eng* 56 118-136 (2020) **DOI:10.3901/JME.2020.16.118**. (in Chinese)

[8] Zhou, Z., Liu, Y., Guo, T., Wang, T., Huo, W. Study on the mechanism of polygonal wear in wheels based on wheel-rail contact normal force. *Int Conf Artif Intell Autonom Transp. Springer Nature* 458-465 (2024) **DOI:10.1007/978-981-96-3969-4_49**.

[9] Johansson, A., Nielsen, J. Out-of-round railway wheels-wheel-rail contact forces and track response derived from field tests and numerical simulations. *Proc Inst Mech Eng F-J Rail Rapid Transit* 217 135-146 (2003) **DOI:10.1243/095440903765762878**.

[10] Johansson, A., Andersson, C. Out-of-round railway wheels-a study of wheel polygonalization through simulation of three-dimensional wheel-rail interaction and wear. *Vehic Syst Dynam* 43 539-559 (2005) **DOI:10.1080/00423110500184649**.

[11] Ye, Y., Qu, S., Wei, L., Li, D., Huang, C., Wang, J. et al. Localized rail third-order bending mode causes high-order polygonization of high-speed train wheels. *Mech Syst Signal Proces* 223 111816 (2025) **DOI:10.1016/j.ymssp.2024.111816**.

[12] Yang, X., Tao, G., Li, W., Wen, Z. On the formation mechanism of high-order polygonal wear of metro train wheels: Experiment and simulation. *Eng Failure Analys* 127 105512 (2021) **DOI:10.1016/j.engfailanal.2021.105512**.

[13] Wu, Y., Du, X., Zhang, H., Wen, Z., Jin, X. Experimental analysis of the mechanism of high-order polygonal wear of wheels of a high-speed train. *J Zhejiang Univ-Scie A* 18 579-592 (2017) **DOI:10.1631/jzus.A1600741**.

[14] Fu, D., Wang, W., Dong, L. Analysis on the fatigue cracks in the bogie frame. *Eng Fail Anal* 58 307-319 (2015) **DOI:10.1016/j.engfailanal.2015.09.004**.

[15] Wang, B., Xie, S., Jiang, C., Along, Q., Sun, S., Wang, X. An investigation into the fatigue failure of metro vehicle bogie frame. *Eng Fail Anal* 118 104922 (2020) **DOI:10.1016/j.engfailanal.2020.104922**.

[16] Liu, X., Zhai, W. Analysis of vertical dynamic wheel/rail interaction caused by polygonal wheels on high-speed trains. *Wear* 314 282-290 (2014) **DOI:10.1016/j.wear.2013.11.048**.

[17] Song, Y., Zhang, X., Sun, B. Influence of polygonal wear on dynamic performance of wheels on high-speed trains. *Tehn Vjest* 28 27-33 (2021) **DOI:10.17559/TV-20190103105240**.

[18] Wu, X., Rakheja, S., Qu, S., Wu, P., Zeng, J., Ahmed, A.K.W. Dynamic responses of a high-speed railway car due to wheel polygonalisation. *Vehic Syst Dyn* 56 1817-1837 (2018) **DOI:10.1080/00423114.2018.1439589**.

[19] Barke, D.W., Chiu, W.K. A review of the effects of out-of-round wheels on track and vehicle components. *Proc Inst Mech Eng F-J Rail Rapid Trans* 219 151-175 (2005) **DOI:10.1243/095440905X8853**.

[20] Zhang, J., Han, G., Xiao, X., Wang, R., Zhao, Y., Jin, X. Influence of wheel polygonal wear on interior noise of high-speed trains. *Chi High-Speed Rail Tech* 373-401 (2018) **DOI:10.1007/978-981-10-5610-9_20**.

[21] Thomas, D., Berg, M., Stichel, S. Measurements and simulations of rail vehicle dynamics with respect to overturning risk. *Vehic Syst Dyn* 48 97-112 (2010) **DOI:10.1080/00423110903243216**.

[22] Park, J.H., Koh, H.I., Kim, N.P. Parametric study of lateral stability for a railway vehicle. *J Mech Sci Tech* 25 1657-1666 (2011) **DOI:10.1007/s12206-011-0421-0**.

[23] Ma, S., Wang, H., Yao, Y., Ding, W. Stability analysis of high-speed vehicles considering the non-diagonal stiffness of a series of steel springs and frame flexibility. *Mech Des Manuf* 6 300-304 (2023) **DOI:10.19356/j.cnki.1001-3997.20230307.005**. (in Chinese)

[24] Guan, Q., Wen, Z., Chi, M., Liang, S. Phase synchronization modal analysis of wheelset hunting motion. *J Mech Eng* 57 279-288 (2021) **DOI:10.3901/JME.2021.24.279**. (in Chinese)

[25] Xiao, Q., Cheng, Y., Luo, J., Zhou, S., Zhou, Q., Cao, T. Sensitivity analysis of high-speed train wheel vibration influenced by vehicle-track coupling. *J Traff Transp Eng* 21 160-169 (2021) **DOI:10.19818/j.cnki.1671-1637.2021.06.012**. (in Chinese)

[26] Lei, X., Wang, Z., Luo, K. Research on the dynamic performance of Nanchang metro vehicles. *J Rail Sci Eng* 14 2460-2466 (2017) **DOI:10.19713/j.cnki.43-1423/u.2017.11.025**.

[27] Mousavi Bideleh, S.M., Berbyuk, V. Global sensitivity analysis of bogie dynamics with respect to suspension components. *Multibody Syst Dyn* 37 145-174 (2016) **DOI:10.1007/s11044-015-9497-0**.

[28] Cascino, A., Meli, E., Rindi, A. A new strategy for railway bogie frame designing combining structural-topological optimization and sensitivity analysis. *Vehicles* 6 651-665 (2024) **DOI:10.3390/vehicles6020030**.

[29] Cascino, A., Meli, E., Rindi, A. . Development of a design procedure combining topological optimization and a multibody environment: Application to a tram motor bogie frame. *Vehicles* 6 1843-1856 (2024) **DOI:10.3390/vehicles6040089**.

[30] Luo, R.K., Gabbitas, B.L., Brickle, B.V. Fatigue life evaluation of a railway vehicle bogie using an integrated dynamic simulation. *Proc Inst Mech Eng F-J Rail Rapid Transit* 208 123-132 (1994) **DOI:10.1243/PIME_PROC_1994_208_242_02**.

[31] Luo, R.K., Gabbitas, B.L., Brickle, B.V. Dynamic stress analysis of an open-shaped railway bogie frame. *Eng Fail Anal* 3 53-64 (1996) **DOI:10.1016/1350-6307(95)00030-5**.

[32] Cascino, A., Meli, E., Rindi, A. Dynamic size optimization approach to support railway carbody lightweight design process. *Proc Inst Mech Eng F-J Rail Rapid Transit* 237 871-881 (2022) **DOI:10.1177/0954409722114093**.

[33] Tang, J., Zhou, Z., Chen, H., Wang, S., Gutiérrez, A. Research on the lightweight design of GFRP fabric pultrusion panels for railway vehicle. *Compos Struct* 286 115221 (2022) **DOI:10.1016/j.compstruct.2022.115221**.

[34] Cascino, A., Meli, E., Rindi, A. Comparative analysis and dynamic size optimization of aluminum and carbon fiber thin-walled structures of a railway vehicle car body. *Materials* 18 1501 (2025) **DOI:10.3390/ma18071501**.

[35] Cascino, A., Meli, E., Rindi, A. A strategy for lightweight designing of a railway vehicle car body including composite material and dynamic structural optimization. *Rail Eng Sci* 31 340-360 (2023) **DOI:10.1007/s40534-023-00312-6**.

[36] Zhou, L., Wang, G., Sun, K., Li, X. Trajectory tracking study of track vehicles based on model predictive control. *Stroj Vest-J Mech E* 65 329-342 (2019) **DOI:10.5545/sv-jme.2019.5980**.

[37] Yu, Y., Song, Y., Zhao, L., Zhou, C. Analytical formulae and applications of vertical dynamic responses for railway vehicles. *Stroj Vest-J Mech E* 69 73-81 (2023) **DOI:10.5545/sv-jme.2022.375**.

Acknowledgement *The authors would like to thank for the support for ties work by Research Program supported by General Program of Henan Provincial Natural Science Foundation (Project No.: 252300421908), China, Open Project of the State Key Laboratory of Rail Transit Vehicle System (RVL2509), China and by Heilongjiang Provincial Postdoctoral Science Project (grant numbers LBH-Z23041), China.*

Received: 2025-07-10, revised: 2025-09-24, 2025-10-22, accepted: 2025-10-29 *as Original Scientific Paper.*

Declaration of Conflicting Interests *The author(s) declared no potential conflicts of interest with respect to the research, authorship, and/or publication of this article.*

Data Availability *The data that supports the findings of this study are available from the corresponding author upon reasonable request.*

Author Contribution *Yuru Li: Conceptualization, Methodology, Formal analysis, Investigation, Visualization, Writing–original draft; Gangjian Zhou: Formal analysis, Investigation, Visualization, Writing–review and editing; Xiangwei Li: Formal analysis, Investigation; Tao Zhu: Formal analysis, Investigation; Shangchao Zhao: Formal analysis, Investigation; Chunlei Zhao: Formal analysis, Investigation; Junke Xie: Conceptualization, Formal analysis, Investigation; Shoune Xiao: Conceptualization, Formal analysis, Investigation, Supervision.*

Dinamično obnašanje železniškega vagona C80 pod vplivom poligonalnosti koles in značilnih oblik nihanja karoserije

Povzetek *Za raziskavo vpliva značilnih oblik nihanja in poligonalnosti koles na dinamične lastnosti karoserije železniškega tovornega vagona je bil v tej raziskavi izbran vagon C80. Razvita sta bila model na ravni vozila in model na ravni sistema z metodo končnih elementov, ki sta pokazala, da bočna in navpična togost tovornih vagonov pomembno vplivata na sistemske lastne oblike. Nadalje je bila z uporabo so-simulacije med programoma NASTRAN in SIMPACK vzpostavljena popolnoma fleksibilna dinamična simulacija vagona C80. Analiziran je bil vpliv značilnih lastnih frekvenc na dinamično obnašanje vagona ob upoštevanju poligonalnosti koles in parametrov obrabe. Rezultati kažejo, da omejitev torzijske oblike nihanja vagona zmanjša njen vpliv na koeficient iztirjenja, stopnjo zmanjšanja obremenitve koles, prečno silo osi in koeficient prevračanja za več kot 40 %. Ko se hitrost vlaka ujema z redom poligonalnosti koles, se stopnja zmanjšanja obremenitve koles povečuje z globino obrabe pri poligonalnosti 10. in 18. reda. Pri slednjem se ob povečanju globine obrabe z 0,01 mm na 0,05 mm poveča za kar 14,4 %. Poleg tega je bilo ugotovljeno, da omejitev torzijske oblike bistveno poveča stopnjo zmanjšanja obremenitve koles pri poligonalnosti 6., 10., 16. in 18. reda, zlasti pri poligonalnosti 6. reda. Raziskava nudi smernice za optimizacijo parametrov vzmetenja in nadzor poligonalne obrabe koles pri železniških vagonih ter predstavlja teoretično osnovo za izboljšanje njihove dinamične zmogljivosti.*

Ključne besede *popolna fleksibilnost, železniški vagon C80, dinamični modeli, poligonalnost koles, parametri vzmetenja*

Two-Stage Optimal Design of Metro Underframe Structures: Based on Topology-Size-Shape Co-Optimization Methodology

Delei Du – Yana Li – Jian Song – Zhengping He – Jianxin Xu ✉
Key Laboratory of Railway Industry on Safety Service Key Technologies for High-speed Train, CRRC College, Dalian Jiaotong University, China
✉ xujianxinxjx@163.com

Abstract *The design of the metro body structure must balance both safety and cost indicators. The underframe is not only the main load-bearing component of the metro body but also accounts a significant portion of its overall mass. To reduce operational costs and enhance the safety performance of the metro body, this paper focuses on optimizing the design of the underframe. A two-stage optimization approach was proposed, addressing the limitation of existing methods and the challenges in balancing realistic operating conditions with manufacturability. First, manufacturing constraints were incorporated using the variable density method, and topology optimization of the underframe sub-model was carried out with the objective of minimizing flexibility-weighted strain energy. Next, the rough topology was refined through parametric optimization after determining the approximate shape of the cross section, resulting in a more precise model. The results show that the proposed optimization method reduces underframe mass by about 4.7 % while lowering the maximum deflection of the metro car body under the maximum vertical load case by 0.601 mm. This demonstrates that the proposed framework efficiently combines optimization capabilities with simplicity.*

Keywords *underframe, structural optimization, collaborative optimization, lightweighting*

Highlights

- *Joint topology, size and shape were optimized for reducing performance errors in reconfigured shapes.*
- *Multi-case weighting strategy simplified the calculation for varied engineering conditions.*
- *Improvement of vertical load form, closer to the actual environment, increasing the reliability of optimization.*
- *The mass of the underframe was reduced by 4.7 %, and the maximum vertical displacement was reduced by 0.601 mm.*

1 INTRODUCTION

Structural optimization design is an important part of the design process of locomotive body. Based on the form the of optimization, it can be clasified into topology optimization, size optimization, and shape optimization [1]. The rapid development of computers has created favorable conditions for the progress of optimal design, and the theory itself has become increasingly mature and widely applied in engineering practice [2-4]. Among these methods, topology optimization focuses on determining the optimal material distribution within a given design domain [5]. As a powerfull tool for the initial stage of structural design, topology optimization identifies topological configurations that represent the main transmission paths of physical information within the structure. This enables engineers to analyze how different shapes influence physical fields by interpreting these results [6-8]. In recent years, the research on topology optimization has intensified. Bai et al. [9] obtained hollow structures by the moving deformable component method, and achieved the first explicit 3D topology optimization for hollow structures by combining the internal and external topological description functions. Later, multi-material topology optimization was achieved by describing coating material distibution with multiple level set functions [10]. Similary, Guo et al. [11] combined the advantages of explicit and implicit topology optimization to introduce a new method for multi-material applications. Although these developmens mark significant progress, topology optimization still faces challenges that limit its full implementation in engineering practice.

Size optimization, as a parametric optimization tool, treats material dimensions as design variables [12]. Shape optimization, on the other hand, allows for small modifiations to an existing structure to further exploit its mechanical performance [13,14]. Both size and shape optimization serve as structural refinement optimization tools that fine-tune dimensions and geometric details, thereby complementing the challenges of directly appling topology optimization results in engineering [15,16]. In recent years, researchers have increasingly combined these three optimization methods to form a two- or three-stage optimization frameworks, which have proven effective in numerous cases. For example, Tomás and Marti [17] applied shape optimization combined with size optimization in the design of a concrete shell, confirming the value of refinement optimization. Zhu et al. [18] utilized topology and size optimization for lightweight wind turbine blades design, achieving a 3 % reduction in mass. Wang et al. [19] combined topology optimization with shape optimization to develop an optimization algorithm for spatial steel frames with adaptable cross-section structures. Similarly, Zhao et al. [20] proposed a topology and size optimization strategy considering displacement, stress and stability constraints.

However, a single optimization method often cannot support engineers in designing structures that meet engineering realities while coping with complex environments. For this reason, researchers have approached the problem in two main ways. On the one hand, optimization algorithms have been refined to address specific requirements [21-23]. On the other hand, improving a particular algorithm is not always universally accepted, as its applicability may be limited. Therefore, some researchers changed the method the way optimization models impose working conditions to make the results more practical and reliaible. Bai et al. [24] investigated the three-point bending characteristics of a double rectangular thin-walled tube and analyzed its crashworthiness by equating the energy characteristics under those conditions. Sha et al. [25] proposed a multi-case topology

optimization method adapted for robots, enabling lightweight design while accounting for changes in robot posture. Golubin [26] derived a first-order necessary condition for optimal solutions based on geometrically preferred conical dyads, providng a reliable scheme for resolving optimization conflicts in structures subject to different working conditions. Zhu et al. [27] transformed the homogeneous load condition of the locomotive underframe into an equivalent centralized load condition. This approach solved the common problem in topology optimization where low strain energy leads to missing material in the middle region of the underframe.

Although structural optimization methods have been studied in depth, optimization of railroad locomotives has mainly focused on dimensions [28], materials [29] or individual components [30]. However, optimizing the entire locomotive body still presents challenges in practical application [31,32]. In this context, this paper proposes a two-stage optimization method to improve the structural performance of subway car bodies. In this paper, topology optimization serves mainly as a structural reshaping tool, while size and shape optimization act as refinement tools. The optimization strategy unfolds sequentially across two main stages. In the initial stage, topology optimization performed using a variable density approach with manufacturing constraints, targeting the minimization of flexibility-weighted strain energy. This process yields an initial material layout. In the second stage, this layout is refined through parametric optimization, combining dimensional optimization (to adjust plate thickness) and shape optimization (to refine the geometry of corrugated plate nodes). This synergistic approach ensures the attainment of high-performance structural solutions without compromising manufacturability. In the topology optimization stage, 3D optimization is superior to 2D optimization in terms of material distribution [3]. Therefore, the chassis model was discretized into solid elements, and a multiple-case equally weighted compromise planning method is used to simsplify the multi-objective function problem into a single-objective function problem [33]. The model is then reconstructed according to the topology results, with the upper and lower bounds for size optimization defined by sensitivity values. Finally, the cross-sectional shapes are refiened through shape optimization. To better simulate actual engineering conditions, vertical loads are applied incrementally as step loads toward the middle section before size optimization. The results show that this form of optimization method effectively reduces reconstruction error from topology results and produces a more accurate cross-section layout of the underframe.

2 METHODS AND MATERIALS

2.1 Topology Optimization

Topology optimization determines the optimal material distribution that maximizes structural stiffness. Based on the material distribution cloud diagram from the topology result, the main force transmission path of the underframe can be determined, which in turn provides guidance for the preliminary layout of the corrugated plate. To further quantify the influence of the material properties on structural stiffness, it is necessary to establish the relationship between the material's elastic modulus and its density. This relationship can be expressed as a functional dependence of the elastic modulus on the density:

$$E(\rho_e) = E_{\min} + \rho_e^p (E_0 - E_{\min}), \quad \rho_e \in [0,1]. \tag{1}$$

In Equation (1), ρ_e represents the relative density of the material, which serves as thedesign variable in topology optimization. E_0 is the elastic modulus of the original material, while $E_{\min}$ is the elastic modulus to elements that are effectively removed during optimization. The parameter p denotes the penalty coefficient within solid isotropic material with penalization (SIMP) algorithm, which controls the material removal rate, defined as $p \in (1,5]$. Generally, larger values of p enhance the suppression of intermediate densities, which makes the material distribution closer to a clear 0-1 (void-solid) state. However, excessively high penalty values can substantially increase the burden of computation.Therefore, in practical engineering applications, $p=3$ is most commonly adopted [5].

In multi-stiffness optimization, the optimal topology varies across different working conditions. Since real engineering applications must withstand multiple load conditions, combining these conditions yields results that are more representative of practical performance. In this paper, we establish a mathematical model for multi-stiffness topology optimization and implement it in OptiStruct using a custom function. By applying the compromise planning method, the multi-objective problem is transformed into a single-objective problem, enabling a balanced and computationally efficient solution.

$$C(\rho) = \left[\sum_{k=1}^{m} \omega_k^p \left(\frac{C_k(\rho) - C_k^{\min}}{C_k^{\max} - C_k^{\min}} \right)^p \right]^{\frac{1}{p}}. \tag{2}$$

In Equation (2), ρ is the design variable, $C(\rho)$ objective function defined by compliance, m total number of conditions, ω_k weighted compliance value of the k^{th} working condition. Since stiffness maximization is typically equivalent to the compliance minimization, this formulation is standard in structural optimization. Notation p is the penalty coefficient, and $C_k(\rho)$ represent a compliance function, and $C_k^{\max}$ and $C_k^{\min}$ are the maximum and minimum values, respectively.

In addition, minimum and maximum member size constraints are considered in the optimization process to prevent occurrence of free cells and excesive material accumulation. The minimum member size constraint is enforced through the density filtering function, ensuring that structural features remain manufacturable and mechanically meaningful.

$$\tilde{\rho}_i = \frac{\sum_{j\in\Omega(i)} \omega_{ij}\rho_j}{\sum_{j\in\Omega(i)} \omega_{ij}}, \quad \omega_{ij} = \max\left(0, r_{\min} - \left\|\mathbf{x}_i - \mathbf{x}_j\right\|\right), \tag{3}$$

where $\tilde{\rho}_i$ is the filtered design variable, ρ_j original material density, ω_k weight coefficient, and $\Omega(i)$ neighborhood centered on cell i with radius r, where $r_{\min}$ coresponds to the minimum member size radius.

The maximum member size constraint is enforced using inverse density filtering, ensuring that overly large structural members do not form during the optimization process.

$$\tilde{\rho}_e = 1 - \frac{\sum_{i\in\Omega(i)} \omega_{ij}(1-\rho_j)}{\sum_{i\in\Omega(i)} \omega_{ij}}, \quad \Omega(i) = \left\{ j \mid \left\|\mathbf{x}_j - \mathbf{x}_e\right\| \le r_{\max} \right\}. \tag{4}$$

At this point $r_{\max}$ is the maximum size radius. In summary, the mathematical model for the subway underframe section based on the compromise planning method can be expressed as follows:

$$\text{find: } \rho = (\rho_1, \rho_2, \ldots, \rho_n)^T,$$

$$\min: C(\rho) = \left[\sum_{k=1}^{m} \omega_k^p \left(\frac{C_k(\rho) - C_k^{\min}}{C_k^{\max} - C_k^{\min}} \right)^p \right]^{\frac{1}{p}},$$

$$\text{s.t.}: \sum_{k=1}^{m} \left(\sum_{j=1}^{n} V_j \rho_j^k \right) - V_z \le 0,$$

$$\tilde{\rho}_i = \frac{\sum_{j\in\Omega(i)} \omega_{ij}\rho_j}{\sum_{j\in\Omega(i)} \omega_{ij}}, \quad \tilde{\rho}_e = 1 - \frac{\sum_{i\in\Omega(i)} \omega_{ij}(1-\rho_j)}{\sum_{i\in\Omega(i)} \omega_{ij}},$$

$$0 < \rho_{\min} \le \rho_j < 1, \quad j = 1,2,\ldots,n, \quad k = 1,2,\ldots,m.$$

In the above formula, V_j is volume of the j^{th} cell, V_z maximum volume in the design space of the model, and s.t. the constraint", while n is a total number of units in the design domain. In this paper, the volume fraction was used as the constraint.

2.2 Plate Thickness Size Optimization

Sensitivity analysis is an analytical method used to investigate how sensitive a system's response is to changes in model parameters, arising either from variations in operating states or from internal modification of the model itself. The response sensitivity with respect to a design variable can be expressed as follows:

$$[\mathbf{K}]\{\mathbf{U}\} = \{\mathbf{P}\}. \tag{5}$$

Taking partial derivatives on both sides of the above equation, respectively.

$$\frac{\partial[\mathbf{K}]}{\partial x_i}\{\mathbf{U}\} + [\mathbf{K}]\frac{\partial\{\mathbf{U}\}}{\partial x_i} = \frac{\partial\{\mathbf{P}\}}{\partial x_i}. \tag{6}$$

Vector **U** partial derivatives:

$$\frac{\partial\{\mathbf{U}\}}{\partial x_i} = [K]^{-1}\left(\frac{\partial\{\mathbf{P}\}}{\partial x_i} - \frac{\partial[\mathbf{K}]}{\partial x_i}\{\mathbf{U}\}\right). \tag{7}$$

In Equation (7), $\partial\{\mathbf{U}\}/\partial x_i$ represents the sensitivity of the objective function with respect to the design variable x_i. In this paper, the traditional approach to sensitivity analysis is adopted, while also considering the setting of constraint objectives during size optimization. Accordingly, both displacement sensitivity and mass sensitivity are selected as the primary reference sensitivity values in the analysis.

Based on the determined layout of the corrugated plate cross-section, the chassis section was further refined by optimizing the cross-sectional area of the reinforcing plate. Bending resistance is one of the key criteria for evaluating vehicle structural performance; therefore displacement parameters of the model are considered in the optimization process of this paper. The specific optimization model is formulated as follows:

find: $X = \{x_1, x_2, ..., x_{15}\}$,
min: $U_{size} = \min \mathbf{u}(d)$,
s.t.: $x_{\min} \le x_i \le x_{\max}$,
$\sigma_{\max} - 90$ MPa ≤ 0,

$$\sum_{i=1}^{n} mass_{xi} - 1.1 mass_z \le 0,$$

where X is the design variable, U_{size} maximum displacement of the model node, $\mathbf{u}(d)$ displacement vector, $x_{\min}$, $x_{\max}$ upper and lower limits of the thickness of the reinforcing plate, $\sigma_{\max}$ maximum stress under the constraints of the model, $mass_{xi}$ mass of the i^{th} design variable, and $mass_z$ mass of the current structural model.

It was worth noting that, according to the EN 12663:2010 standard [34], the factor of safety for the yield strength of the body material must exceed 1.5. However, since this study focuses specifically on the underframe, more conservative stress constraints as well as higher mass redundancy are adopted. Section 2.3 adheres to the same constraint rules for constraints, maintaining consistency across the design process.

2.3 Shape Optimization

Shape optimization integrates geometric modeling, structural analysis and optimization [35]. It is an optimization design technique that refines structural boundaries or shapes by adjusting the node positions of the finite element model. Once the underframe cross-section structure is determinded, shape optimization can be applied to make localized structural distribution adjustments of the corrugated reinforcing plate. These refinements enhace the structural stiffness or strength while ensuring compliance with the principle of stiffness coordination. The specific optimization model is defined as follows:

find: $S = (s_1, s_2, ..., s_{28})^T$,
min: $U_{shape} = \min \mathbf{r}(d)$,
s.t.: $S_m \le S_i \le S_l$,
$\sigma_{\max} - 60$ MPa ≤ 0,

$$\sum_{i=1}^{n} mass_{xi} - 1.1 mass_{z1} \le 0,$$

where S is the design variable representing shape optimization control displacement matrix, U_{shape} maximum displacement of the model node, $\mathbf{r}(d)$ displacement vector, S_m, S_l upper and lower limits of the node displacement of the reinforcing plate, $\sigma_{\max}$ maximum stress under the constraints of the model, and $mass_{xi}$ mass of the i^{th} design variable. $mass_{z1}$ is the mass of the current structural model.

2.4 Subway Underframe Section Status

The research object of this paper was the head section of a specific subway model, focusing on the original underframe cross-section structure, as shown in Fig. 1c. The body structure consist of large cross-section aluminum profiles combined with plate welding, while the underframe is made of aluminum alloy 6005A-T6. The 6000-series aluminum alloys are known for their excellent bending performance and are widely applied in the manufacturing of complex extruded parts. After finite element simplification, the main dimensions of the chassis were defined as follows: excluding the side beams, the transverse width of the chassis is 2500 mm, five corrugated plates are overlapped, each with a thickness of 2.5 mm, and the surface plate thickness is 2.8 mm.

Passengers in a train are in direct contact with the floor, which was subjected to vertical loads.The bending stiffness of the underframe is therefore a key criterion for evaluating the safety of the locomotive. During the process of structural optimization, the maximum displacement of the model can seve as a reference parameter, or it can be defined directly as both a target and a constraint condition.

In the optimization process, the boundary conditions can be defined with reference to the operating conditions of the metro body. In this paper, the operating conditions of the metro were established in accordance with [34], taking into account the calculation standards and detailes outlined in Section 2.5.

2.5 Load Conditions

The cross-section of the selected metro underframe is a hollow aluminum alloy plate with a corrugated structure, divided into five overlapping segments. This configuration provides good ductility, low weight, and high impact resistance. To ensure that the simulated load conditions closely reflect actual engineering scenarios and to improve the accuracy of load path calculation, four static strength conditions were selected: maximum vertical load, longitudinal tensile load, longitudinal compressive load and torsion load .

Table 1. The reference load case of the subway

Conditions	Load case description	Load
LC01	Maintenance mass and maximum overload	$g \times (m_1 + m_4)$
LC02	Compression condition	1200 kN
LC03	Tensile condition	960 kN
LC04	Torsional condition	40 kNm

g is gravitational acceleration; m_1 car body weight, and m_4 passenger mass in overloaded conditions

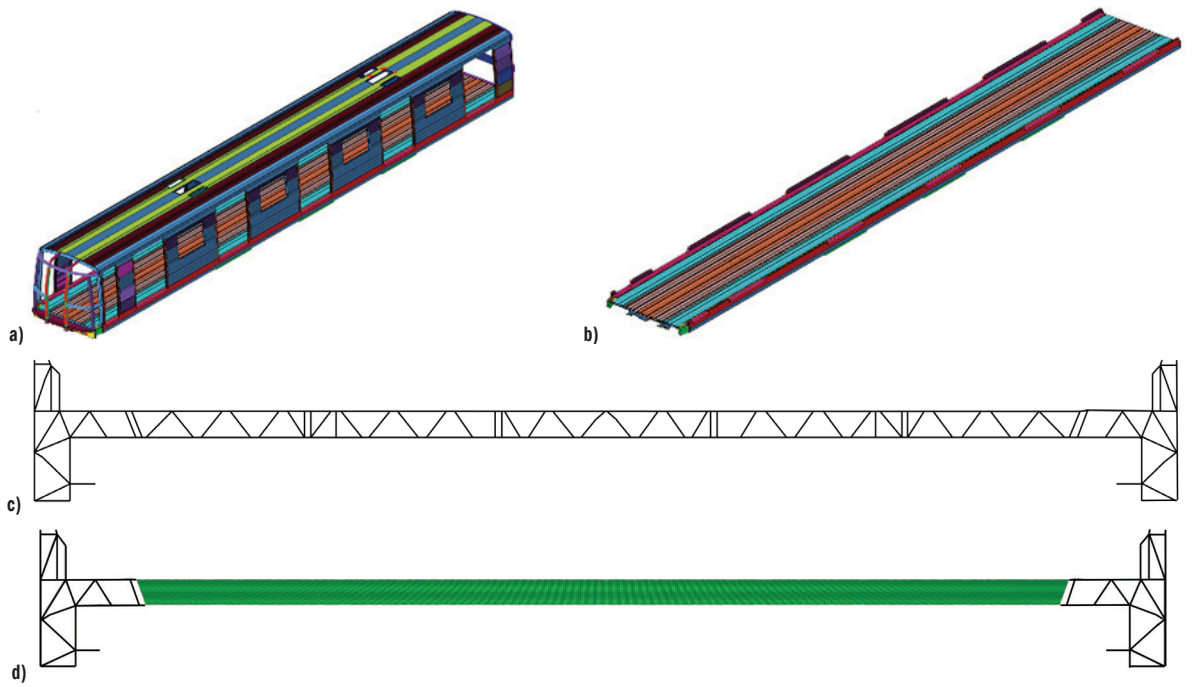

Fig. 1. Metro underframe structure and design domains; a) metro car body structure diagram, b) underframe structure diagram, c) underframe side beams, and d) underframe design domains

As presented in Fig. 1, the design domain represents the primary region for applying model loads. The constraints were imposed at the lap joints between the side beams and the bottom frame. From this design domain, the arrangement, shapes, and dimensions of the corrugated plates were developed and optimized. The corresponding optimization results and their analysis are presented in Section 3.

3 RESULTS AND DISCUSSION

The optimization process of the metro underframe cross-section was carried out in two stages. In the first stage, topology optimization was applied to reconfigure the layout of the cross-section corrugated plates. In the second stage, parameterized size optimization was performed to refine the corrugated plate thickness, while shape optimization was conducted by adjusting the relative position of the upper and lower nodes of the corrugated plates.

3.1 One Stage Topology Optimization and Result Analysis

Submodels were typically established by extracting submodel boundary moments or displacements under specific operating conditions, depending on the capabilities of the software [36,37]. However, in the case of metro bodies, the application is constrained by the length of the body. The submodel boundary conditions of the chassis section are only valid at the intercepted position in the chassis, which means that the resulting topological configuration cannot be directly applied to the entire vehicle [38].

Therefore, this paper establishes the model shown in Fig. 1d, setting the finite element model in the design domain as a solid element to better observe the force transfer path under loading. According to the topology optimization rules for the metro underframe, the volume of the topology configuration accounts for 0.3 of the design domain. At the same time, based on the compromise planning method, equal weighting was applied, with the maximum vertical load used as the primary working condition. Four groups of different forms of topological configurations with different forms were obtained. By summarizing these four groups of configurations, a resonstructed underframe section was derived to produce a rough new cross-sectional shape. The advantage of this approach is that it allows observation under different combinations of working conditions, highlighting the common force-bearing regions, while avoiding conflicts between conditions, e.g., combining tensile and compressive states.

According to the optimization rules described above, the iterations for four combined condition models converged within 54 to 67 steps. The corresponding material layout contours and the reconstructed model cross-section structure after convergence are shown in Fig. 2.

The topological cloud cross-section was roughly divided into three regions, A, B, and C, according to the material retention density, and the four topological clouds in Fig. 3 were summarized accordingly. Region A is located near the edge beams, experiancing the largest bending moments. As a result, the material retention density was generally higher. However, the boundaries of the material retention zones were diffuze, and reinforcing plates tendet to intersect. To avoid stress concentration, this region was reconstructed with a triangular reinforcing plate structure, connected at both ends. During verification of the rough model, high stress concentrations were observed at the edges, so an additional reinforcing plate was added in the middle of the section to meet this requirement. In region C, most of the material was removed, and a distinct topological configuration appeared only when torsional loading carried a greater weight. Since torsional loading is a frequent operational condition for the metro bodies, a reinforcing plate was added to be placed in the middle of the section to meet this requirements. Region B had a wider span with clearer topological configuration. The force transsmition paths were more consistent across all four combined loading conditions. However, reinforcing plates in certain locations had significant effect on stress and displacement. For simplification, the reiforcing plates in B region were reduced as shown in Fig. 3 above. Finally, considering manufacturability, the optimized underframe was divided into five spliced segments. The lap joints relied on two parallel reinforcing plates, with parallel edges at the overlap boundaries, as illustrated in Fig. 3.

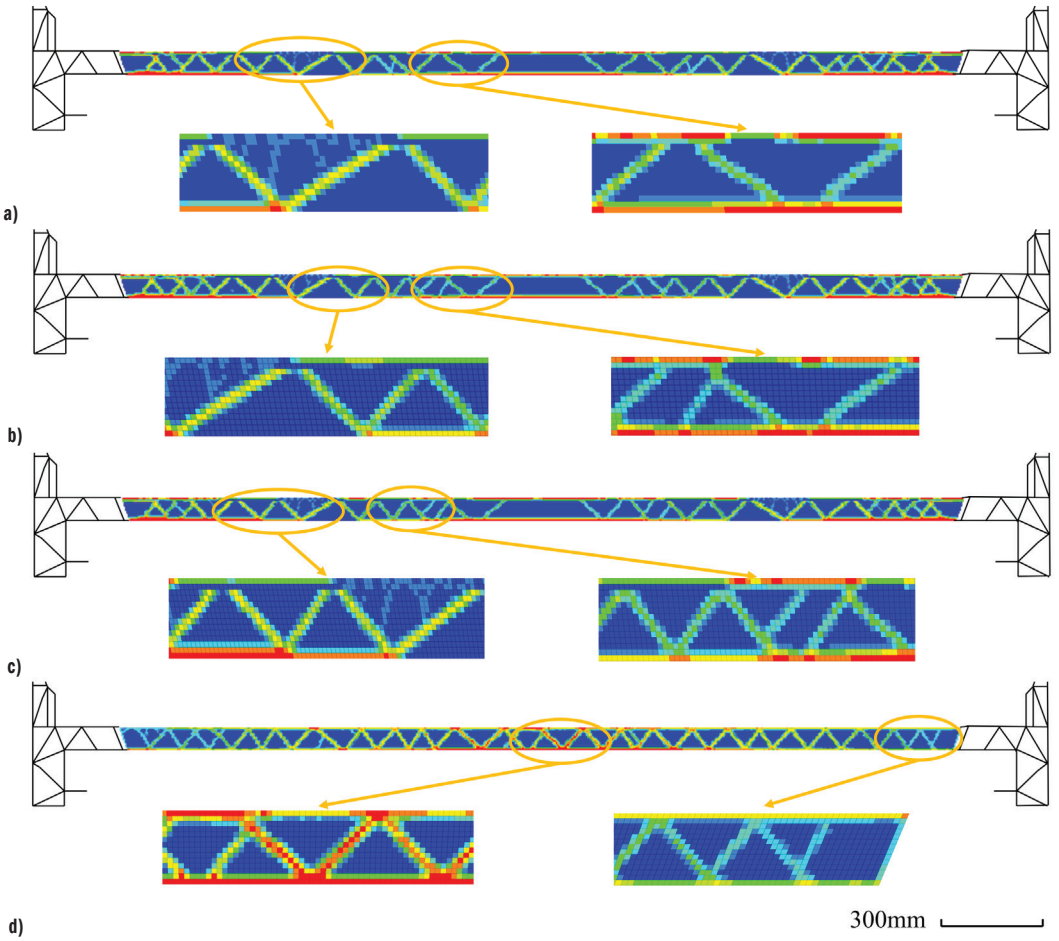

Fig. 2. Topological configuration and rough cross section structure ; a) maintenance mass and maximum overload & compression condition with 1200 kN; b) maintenance mass and maximum overload & tensile condition with 960 kN, c) maintenance mass and maximum overload & torsional condition, and d) maintenance mass and maximum overload & compression condition with 1200 kN

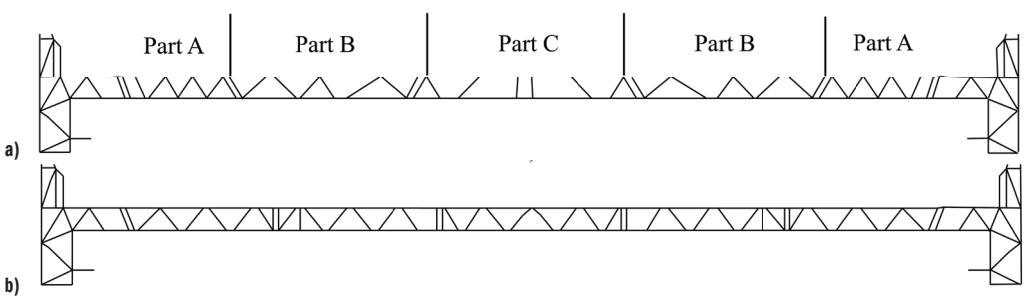

Fig. 3. Comparison of cross-section shapes of chassis; a) reconstructed section, and b) original section

3.2 Two Stage Size Optimization and Result Analysis

To comprehensively evaluate the impact of parameter changes on the models for each part of the design variables, relative sensitivity [39,40] was adopted in this paper as the basis for the design optimization scheme. Relative sensitivity is defined as the ratio of displacement sensitivity to mass sensitivity, enabling a more comprehensive assessment of design variable sensitivity.

The maximum synthetic displacement in the computational model was 2.991 mm, with the maximum displacement point located in the middle of the computational model. To analyze sensitivity to plate thickness, 9 nodes were extracted from the upper and lower surfaces of the longitudinal section passing through this point, The initial thickness of all plates was 2.5 mm. Finally, the calculated sensitivity data were weighted equally. Since metro underframes are tipically left-right symmetric structures, and the reinforcement plates follow the same symmety, only one side of the model was considered as a reference for optimization. On this side, 20 reinforcement plates were present. To reduce the computational workload while maintaining engineering relevance, these 20 reinforcing plates were categorized into 15 component combinations according to their stress conditions.

Based on the magnitude of the absolute sensitivity values, the degree to which Objective function 1 responds to changes in the design variables can be determined. Therefore, taking the absolute value of the sensitivity parameter of each component for comparison, the 15 design variables were categorized into four categories with similar sizes: The first category has a sensitivity range of 57 to 84. The design variable was limited to between 70 % of the initial plate thickness and a maximum of 3 mm. The second category has sensitivity range of 187 to 294. Compared with the first group, these

design variables show much larger sensivitivity changes. Therefore, their maximum plate thickness was increased from 5 mm to 6 mm. The third category falls within a sensitivity range of 436 to 656, which is significantly higher. For this group, the design variables were set to 70 % of the initial plate thickness and a maximum plate thickness of 8 mm. The fourth category shows the larger sensitivity ranging from 941 to 1066. Taking process requirements into account, the maximum thickness limit for this group of design variables was further expaned to 10 mm.

Considering the engineering reality, the vertical load of the underframe is complex. In this study, the distribution form of the maximum vertical load was modified, and the resulting optimization outcomes were sorted out using the mathematical expectation method. According to the sensitivity rules, the calculated dimensions are shown in Table 2, and the coresponding comparisons are ilustrated in Fig. 4.

Table 2. Design variable parameters

Variable class	Comp.	Opt. value 1 [mm]	Opt. value 2 [mm]	Opt. value 3 [mm]	Expect. sort. [mm]	Adj. value [mm]
First	S5	1.75	1.75	1.88	1.79	1.80
	S6	1.75	1.75	1.99	1.83	1.80
	S8	1.75	1.75	1.75	1.75	1.80
	S11	1.75	1.75	1.75	1.75	1.80
	S12	1.75	1.75	1.75	1.75	1.80
Second	S2	5.58	5.43	5.00	5.34	5.50
	S7	2.53	2.54	4.23	3.10	3.00
	S10	2.20	4.67	6.21	4.36	4.50
	S13	3.25	3.23	5.00	3.83	3.80
	S15	1.75	1.75	3.01	2.17	2.00
Third	S1	1.75	1.75	1.88	1.79	1.80
	S14	4.74	4.67	6.21	5.21	5.00
Fourth	S3	1.75	1.75	1.75	1.75	1.80
	S4	1.75	1.75	1.75	1.75	1.80
	S9	3.80	3.63	5.17	4.20	4.00

where Comp. stands for component, Opt. value for optimization value, Expect. sort. for expectation sorting and Adj. value for adjustment value

3.3 Two Stage Shape Optimization and Result Analysis

The shape optimization technique in OptiStruct allows manual definiton of deformation nodes to optimize the model geometry. As shown in Fig. 5, nodes were placed at the connection between the reinforcing plate and the upper and lower surfaces of the underframe, reflecting the actual engineering needs. A total of 28 points of interest were selected, where the deformation nodes were permitted to vary in the range of ±5 mm in the *y*-direction.

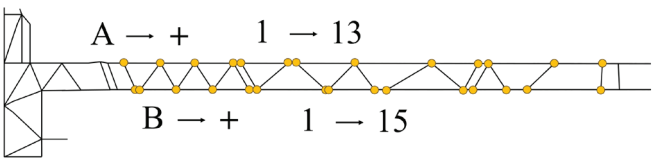

Fig. 5. Positive direction and deformation point serial number

The shape optimization was performed under the original vertical load condition, and an optimization model based on the control handle was established. After two optimization iterations, the deformation analysis showed that the displacement of the deformation point occures along the *y*-axis. The optimal solution was reached under the constraint that the deformation distance was limited to ±5 mm. Considering the manufacturing process requirements, the regularized displacement and direction of the deformation points are shown in Table 3.

Shape optimization is an effective approach to avoid local stress concentrations and achieve locally optimal solutions. As shown in Table 3, the displacement of each node was successfully controlled within ±5 mm. Among them, the symbols "+" and "–" denote the node displacement directions, and this asymmetric displacement pattern reflects the targeted adjustment of the load path. At the same time, it could be observed that the actual displacement of most nodes utilized only about 50 % of the allowable range, or even less. This indicate that, after completing the size optimization stage, the model had no obvious defects, but still retained potential for further improvement. This outcone verifies the effectiveness of shape optimization stage in enhancing local performance.

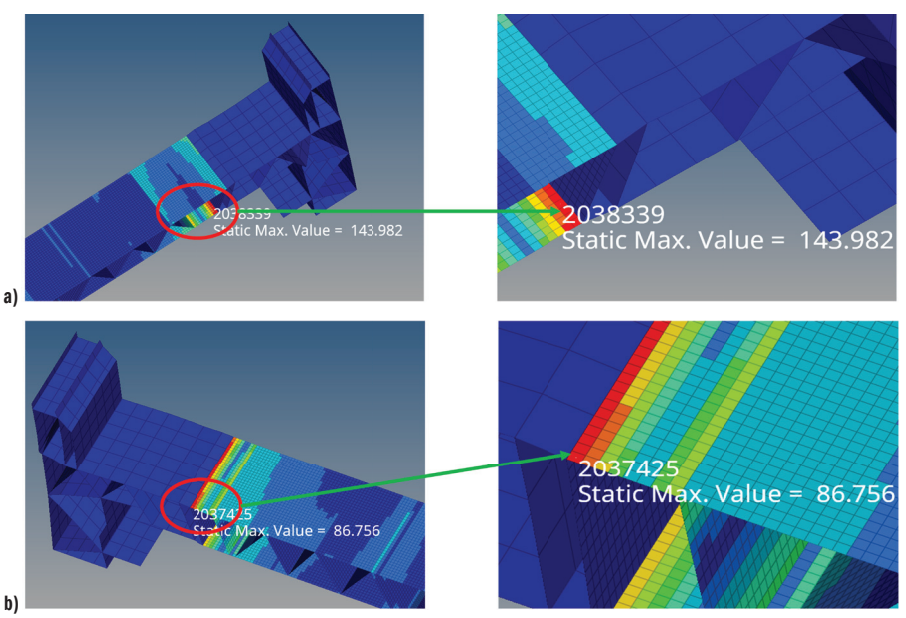

Fig. 4. Size optimization comparison chart of maximum stress; a) before size optimization, and b) after size optimization

Table 3. Graphical representation showing the displacement and direction of deformation points

Point (up)	Distance [mm]	Point (down)	Distance [mm]
A1	-2.6	B1	+1.8
A2	-2.2	B2	-1.7
A3	-2.3	B3	-2.5
A4	-2.3	B4	+2.6
A5	+2.3	B5	+2.4
A6	-1.7	B6	-2.5
A7	+2.1	B7	+1.3
A8	+2.3	B8	-1.3
A9	+2.5	B9	+1.9
A10	+2.5	B10	-2.1
A11	+2.3	B11	+2.6
A12	-2.0	B12	-2.4
A13	-2.3	B13	+2.0
		B14	-2.2
		B15	-2.6

3.4 Optimization Results Analysis

The optimized results are summarized in Table 4, which compares the key performance parameters of the subway car body before and after the two-stage optimization. The evaluation focuses on three indicators: mass, stress and maximum vertical displacement. After optimization, the mass was reduced from 7.354 tons to 7.170 tons, achieving a weight reduction of 0.184 tons, which significantly meets the lightweighting objective. The maximum stress increased only slightly, from 86.91 MPa to 87.12 MPa, a negligible change of 0.19 MPa. This value ramains far below the yield strength of 6005A-T6 aluminum alloy (≥ 215 MPa), thereby fully complying with the EN 12663 standard [34] requirement of a safety factor ≥1.5. At the same time, the maximum vertical displacement decreased from 22.691 mm to 22.090 mm, representing an improvement of 0.601 mm. These data fully verify the effectiveness of the proposed two-stage optimization method, which improves both structural lightweighting and performance enhancement while ensuring compliance with safety standards.

Table 4. Optimize the front and rear car body performance parameters

	Mass [t]	Stress [MPa]	Maximum vertical displacement [mm]
Front	7.354	86.91	22.691
Rear	7.17	87.12	22.090
Difference value	0.184	–0.19	0.601

4 CONCLUSION

This paper proposed a novel two-stage optimization method for the subway car body underframe, based on multiple operating conditions with a focus on both simplicity and efficiency. The optimized results achieved a correction of 0.601 mm for the maximum vertical displacement while satisfying all structural performances. Additionally, the mass of underframe was reduced by 0.184 t, (4.7 % of the mass of underframe). The following conclusions can be drawn from the research results:

a. Traditional single-optimization approaches are unsuitable for complex operating conditions, wheras the proposed method effectively overcomes this limitations.
b. The layout of the corrugated plate should account for stress concentration at the connection between the upper and lower underframes to ensure the stability and safety of the structure.
c. The introduction of multi-condition weighted strategies offers a practical and efficient solution to simplify computational complexity in multi-objective optimization.
d. The weight ratios of different working conditions significantly influence the optimization results, Therefore, adjusting these ratios can bring the outcomes closer to engineering reality, offerring a promising direction for future research.

References

[1] Lee, H.J., Mancini, J.A., Joshipura, I., Spadaccini, C.M., Loh, K.J. Selective heating through Y-junction waveguide designed by acoustic shape optimization. *Adv Eng Mater* 25 2200756 (2023) **DOI:10.1002/adem.202200756**.

[2] Qin, L.Y., Yang, S.Y., Li, H.Z., Dai, J.C., Wang, G.S., Ling, Q.S., Chen, Z.W. Crashworthiness design of bionic-shell thin-walled tube under axial impact. *J Mech Sci Tec* 37 3427-3436 (2023) **DOI:10.1007/s12206-023-0608-1**.

[3] Liu, Z.J., Cho, S., Takezawa, A., Zhang, X.P., Kitamura, M. Two-stage layout-size optimization method for prow stiffeners. *Int J Nav Archit Ocean Eng* 11 44-51 (2019) **DOI:10.1016/j.ijnaoe.2018.01.001**.

[4] Cho, J.G., Koo, J.S., Jung, H.S. A lightweight design approach for an EMU carbody using a material selection method and size optimization. *J Mech Sci Tech* 30 673-681 (2016) **DOI:10.1007/s12206-016-0123-8**.

[5] Eschenauer, H.A., Olhoff, N. Topology optimization of continuum structures: A review. *Appl Mech Rev* 54 331-390 (2001) **DOI:10.1115/1.1388075**.

[6] Qi, L., Zhou, J.X., Jin, P.C., Wang, M.M., Su, Y.Z., Zhou, H.Y., Liu, G.C., Song, L.R. Low noise optimization of two-stage gearbox housing structure based on acoustic contribution analysis and topology optimization. *J Mech Sci Tech* 37 4533-4544 (2023) **DOI:10.1007/s12206-023-0810-1**.

[7] Tejani, G.G., Savsani, V.J., Patel, V.K., Savsani, P.V. Size, shape, and topology optimization of planar and space trusses using mutation-based improved metaheuristics. *J Comput Des Eng* 5 198-214 (2018) **DOI:10.1016/j.jcde.2017.10.001**.

[8] Yvonnet, J., Da, D. Topology optimization to fracture resistance: a review and recent developments. *Arch Comput Meth Eng* 31 2295-2315 (2024) **DOI:10.1007/s11831-023-10044-9**.

[9] Bai, J., Zuo, W. Hollow structural design in topology optimization via moving morphable component method. *Struct Multidisc Optim* 61 187-205 (2020) **DOI:10.1007/s00158-019-02353-0**.

[10] Bai, J., Zuo, W. Multi-material topology optimization of coated structures using level set method. *Compos Struct* 300 116074 (2022) **DOI:10.1016/j.compstruct.2022.116074**.

[11] Guo, Y., Liu, C., Guo, X. Shell-infill composite structure design based on a hybrid explicit- implicit topology optimization method. *Compos Struct* 337 118029 (2024) **DOI:10.1016/j.compstruct.2024. 118029**.

[12] Grihon, S., Krog, L., Bassir, D. Numerical optimization applied to structure sizing at AIRBUS: a multi-step process. *Int J Simul Multidisc Des Optim* 3 432-442 (2009) **DOI:10.1051/ijsmdo/2009020**.

[13] Gui, C., Bai, J., Zuo, W. Simplified crashworthiness method of automotive frame for conceptual design. *Thin Wall Struct* 131 324-335 (2018) **DOI:10.1016/j.tws.2018.07.005**.

[14] Bai, J., Li, Y., Zuo, W. Cross-sectional shape optimisation for thin-walled beam crashworthiness with stamping constraints using genetic algorithm. *Int J Vehicle Des* 73 (2017) **DOI:10.1504/IJVD.2017.082582**.

[15] Sekulski, Z. Least-weight topology and size optimization of high speed vehicle-passenger catamaran structure by genetic algorithm. *Mar Struct* 22 691-711 (2009) **DOI:10.1016/j.marstruc.2009.06. 003**.

[16] Bai, J., Zhao, Y., Meng, G., Zuo, W. Bridging topological results and thin-walled frame structures considering manufacturability. *J Mech Des* 143 091706 (2021) **DOI:10.1115/1.4050300**.

[17] Tomás, A., Martí, P. Shape and size optimisation of concrete shells. *Eng Struct* 32 1650-1658 (2010) **DOI:10.1016/j.engstruct.2010.02.013**.

[18] Zhu, J., Cai, X., Ma, D.F., Zhang, J.L., Ni, X.H. Improved structural design of wind turbine blade based on topology and size optimization. *Int J Low-Carbon Tech* 17 69-79 (2022) **DOI:10.1093/ijlct/ctab087**.

[19] Wang, C., Du, Z., Zhang, Z., Guo, X. Collaborative optimization of topology and cross-sectional shape for space frame structures. *Chin J Theor Appl Mech* 57 937-947 (2025) **DOI:10.6052/0459-1879-24-534**.

[20] Zhao, L., Li, Y., Cai, J., Yi, J., Zhou, Q., Rong, J. Integrated topology and size optimization for frame structures considering displacement, stress, and stability constraints. *Struct Multidisc Optim* 67 48 (2024) **DOI:10.1007/s00158-024-03766-2**.

[21] Körpe, D.S., Güzelbey, I.H. NACA four-digit airfoil series optimization: a comparison between genetic algorithm and sequential quadratic programming. *J Mech Sci Tech* 37 2375-2382 (2023) **DOI:10.1007/s12206-023-0414-9**.
[22] Garcia-Andrés, X., Gutiérrez-Gil, J., Martínez-Casas, J., Denia F.D. Wheel shape optimization approaches to reduce railway rolling noise. *Struct Multidisc Optim* 62 2555-2570 (2020) **DOI:10.1007/s00158-020-02700-6**.
[23] Hu, M.Z., Wang, H.X., Wei, P.T., Liu, G.S., Zhang, L., He, Z. Q., Liu, H.J. Multi-objective optimization of a co-rotating twin-screw gear transmission system based on heuristic search. *J Mech Sci Tech* 37 5831-5841 (2023) **DOI:10.1007/s12206-023-1022-4**.
[24] Bai, J., Meng, G., Wu, H., Zuo, W. Bending collapse of dual rectangle thin-walled tubes for conceptual design. *Thin Wall Struct* 135 185-195 (2019) **DOI:10.1016/j.tws.2018.11.014**.
[25] Sha, L.S., Lin, A.D., Xi, Q., Kuang, S.L. A topology optimization method for robot light-weight design under multi-working conditions and its application on upper-limb powered exoskeleton. *International Conference on Artificial Intelligence and Electromechanical Automation* 17-22 (2020) **DOI:10.1109/AIEA51086.2020.00011**.
[26] Golubin, A.Y. A Note on optimality conditions for multi-objective problems with a euclidean cone of preferences. *J Optim Theory Appl* 166 791-803 (2015) **DOI:10.1007/s10957-014-0698-0**.
[27] Zhu, Y., Liao, L., Ma, R., Yao, S. Research on collaborative optimization of high-speed train car body section profiles. *J Railway Sci Eng* (2025) **DOI:10.19713/j.cnki.43-1423/u.T20250747**.
[28] Liu, Y., Yang, B., Xiao, S. N., Zhu, T., Yang, G., Xiu, R. Parameter study and multi-objective optimization for crashworthiness of a B-type metro train. *P I Mech Eng F-J Rai* 236 91-108 (2022) **DOI:10.1177/ 09544097211008283**.
[29] Wang, J., Yang, B., Tian, H., Wang, W., Sang, X. Optimization design and mechanical performance study of carbon fiber-reinforced composite load-carrying structures for subway driver cabin. *Materials* 18 2524 (2025) **DOI:10.3390/ma18112524**.
[30] Guo, W., Xu, P., Yang, C., Guo, J., Yang, L., Yao, S. Machine learning-based crashworthiness optimization for the square cone energy-absorbing structure of the subway vehicle. *Struct Multidisc Optim* 66 182 (2023) **DOI:10.1007/s00158-023-03629-2**.
[31] Wang, D., Xu, P., Xiao, X., Kong, L., Che, Q., Yang, C. Multiobjective and multicollision scenario reliability-based design optimization of honeycomb-filled composite energy-absorbing structures for subways. *Struct Multidisc Optim* 65 238 (2022) **DOI:10.1007/s00158-022-03343-5**.
[32] Liu, W., Wu, C., Chen, X. An eigenfrequency-constrained topology optimization method with design variable reduction. *Stroj Vestn-J Mech E* 70 159-169 (2024) **DOI:10.5545/sv-jme.2023.739**.
[33] Yu, Y., Song, Y., Zhao, L., Zhao, C. Analytical formulae and applications of vertical dynamic responses for railway vehicles. *Stroj Vestn-J Mech E* 69 73-81 (2023) **DOI:10.5545/sv-jme.2022.375**.
[34] EN 12663:2010. *Railway applications - Structural requirements of railway vehicle bodies - Part 1: Locomotives and passenger rolling stock (and alternative method for freight wagons).* (2010) European Committee for Standards, Brussels.
[35] Hsu, Y.L. A review of structural shape optimization. *Comput Ind* 25 3-13 (1994) **DOI:10.1016/0166-3615(94)90028-0**.
[36] Falconi, D.C.J., Walser, A.F., Singh, H., Schumacher, A. Automatic generation, validation and correlation of the submodels for the use in the optimization of crashworthy structures. Schumacher, A., Vietor, T., Fiebig, S., Bletzinger, KU., Maute, K. (eds.) *Advances in Structural and Multidisciplinary Optimization: Proceedings of the 12th World Congress of Structural and Multidisciplinary Optimization* 1558-1571 Springer, Cham (2018) **DOI:10.1007/978-3-319-67988-4_117**.
[37] Ozturk, U.E. Efficient method for fatigue based shape optimization of the oil sump carrying a differential case in four wheel drive vehicles. *Struct Multidisc Optim* 44 823-830 (2011) **DOI:10.1007/s00158-011-0678-z**.
[38] Sracic, M.W., Elke, W.J. Effect of boundary conditions on finite element submodeling. *Nonlinear Dynam* 1 163-170 (2019) **DOI:10.1007/978-3-319-74280-9_16**.
[39] Tanino, T. Sensitivity analysis in multiobjective optimization. *J Optim Theory Appl* 56 479-499 (1988) **DOI:10.1007/BF00939554**.
[40] Ranjbar, H., Ahmadi, H. Sheshdeh, R.K., Ranjbar, H. Application of relative sensitivity function in parametric optimization of a tri-ethylene glycol dehydration plant. *J Nat Gas Sci Eng* 25 39-45 (2015) **DOI:10.1016/j.jngse.2015.04.028**.

Declaration of Competing Interest *The authors declare that they have no known competing financial interests or personal relationships that could have appeared to influence the work reported in this paper.*

Acknowledgements *The Science and Technology Project Plan of Transportation Department of Liaoning Province (202246), the Fundamental Research Funds for the Provincial Universities of Liaoning (LJ212410150009) and the paper is supported by the Foundation of Liao Ning Educational Department (LJKMZ20220842). The author would like to express his gratitude to its support to this research.*

Received 2025-03-04, revised 2025-08-03, accepted 2025-09-11
as Original Scientific Paper 1.01.

Data Availability *The data supporting the findings of this study are included in the article.*

Author Contribution *Delei Du: Formal analysis, Funding acquisition, Project administration, Writing-original draft, Writing-review & editing. Yana Li: Writing-review & editing. Jian Song: Methodology, Writing-review & editing. Zhengping He: Writing-review & editing. Data curation, Resources, Writing-review & editing. Jianxin Xu: Conceptualization, Methodology, Writing-review & editing.*

Dvostopenjska optimizacija zasnove spodnjega okvirja metroja na osnovi metodologije hkratne optimizacije topologije, velikosti in oblike

Povzetek *Zasnova konstrukcije karoserije metroja mora zadoščati uravnoteženju varnostnih in stroškovnih kazalnikov. Spodnji okvir ni le glavni nosilni element karoserije metroja, temveč predstavlja tudi pomemben delež njene skupne mase. Ta članek se osredotoča na zmanjšanje obratovalnih stroškov in izboljšanje varnostne zmogljivosti karoserije metroja z optimizacijo zasnove spodnjega okvirja. Predlagan je bil dvostopenjski pristop k optimizaciji, ki nadgrajuje omejitve obstoječih metod in obravnava izzive pri uravnoteženju realnih obratovalnih pogojev s tehnologičnostjo. Najprej so bile v postopek vključene proizvodne omejitve z uporabo metode spremenljive gostote, pri čemer je bila izvedena topološka optimizacija delnega modela spodnjega okvirja z namenom minimizacije deformacijske energije, uteženе glede na prožnost. Nato je bila groba topologija izboljšana s parametrično optimizacijo po določitvi približne oblike prereza, kar je privedlo do natančnejšega modela. Rezultati kažejo, da predlagana metoda optimizacije zmanjša maso spodnjega okvirja za približno 4,7 %, hkrati pa zmanjša največji upogibek karoserije metroja pri maksimalni navpični obremenitvi za 0,601 mm. To dokazuje, da predlagana metodologija učinkovito združuje optimizacijske zmogljivosti in preprostost.*

Ključne besede *spodnji okvir metroja, optimizacija strukture, kooperativna optimizacija, zmanjšanje mase*

Kinematics-based Tracking Control Method for Operational Robotic Arm Under Multi-Environmental Constraints

Li Zhou[1] ✉ – Yan Liu[2]

1 School of Mechanical and Electrical Engineering, Hunan City University, China
2 College of Information and Electronic Engineering, Hunan City University, China
✉ 13617375587@163.com

Abstract *The environmental hazards associated with coal mining operations are extremely high, making the use of robotic arms to replace manual labor crucial for improving both the safety and cost-effectiveness of the work process. To address the various environmental constraints, such as spatial limitations, obstacles, and internal and external disturbances, this study proposes a kinematic-based tracking and control method for mining robotic arm. The objective of this numerical study is to mitigate the impact of environmental constraints on the stability of robotic arms, ensuring that they can maintain high precision and stability in complex operating conditions. Simulation results showed that the proposed method enabled the robotic arm to achieve operational thrust peaks exceeding 13,968 N and screw torque peaks greater than 0.06 Nm. The system reached steady state in an average of 0.24 s, with an error reduction of 2.3 %. Compared to other methods, the disturbance tracker reduced the average error by 2 %, and the feedback controller decreased the prediction lag by 5 %. Overall, this method significantly enhances the accuracy and stability of robotic arms in coal mining operations, making it a promising approach for real-world applications.*

Keywords *coal mining operations, robotic arm, dynamics, multi-environmental constraints, tracking control*

Highlights

- *The control method for mining robot arm movement explicitly accounts for environmental constraints.*
- *Fifth-degree interpolation is applied to smooth motion control, enhance performance, and improve energy efficiency.*
- *A hybrid control strategy combines proportional-integral-derivative (PID) control with adaptive control to reduce errors and increase robustness.*

1 INTRODUCTION

Currently, most coal mines still rely on traditional manual operation methods. The high complexity and harsh conditions of coal mining environments expose miners to significant risks for prolonged periods. Moreover, work accuracy is often affected by environmental factors [1]. With the growing demand for improved safety and accuracy in coal mining and the advancement of automation and intelligent machinery, the prospect of unmanned coal mining is becoming increasingly feasible [2]. The key enabler of unmanned mining is the application of multi-joint robot arm (RA), which can perform the coal extraction tasks through coordinated joint rotation and displacement [3]. However, numerous internal and external disturbances limit the development of RA anthropomorphism. Therefore, achieving more accurate modeling parameters and effective tracking control remains a central challenge in the RA research [4]. Minimizing RA trajectory tracking errors through a combination of control schemes and anti-interference techniques is critical for advancing unmanned mining technology [5].

Many experts and scholars have conducted extensive research on control strategy for the dynamic modeling of RA, providing a solid foundation for subsequent trajectory planning. Lattanzi et al. [6] proposed a sliding-mode-based RA control technique aimed at addressing motion synchronization control issues. Their outcomes demonstrated that the approach could successfully develop a simulation model that satisfies the automation criteria of heavy-duty RAs. To quantify system perturbations, Li et al. [7] presented a neural network-based control technique. The outcomes revealed that this approach could accurately predict the degree environmental uncertainties affect RA, resulting precise location monitoring. Zahaf et al. [8] proposed an adaptive slip film-based control method that solved the disturbance prediction problems in hydraulic systems. Simulation tests quantified and compensated for external disturbances effectively [8]. Jouila et al. [9] proposed a control strategy based on calculus combinations that addresses the saturation problem of disturbance quantities during model construction. This method effectively improved the control strategy upon traditional control strategies, simplifying the simulation model construction process while enhancing effectiveness [9]. Cheng et al. [10] proposed a bias-correction-based control strategy, capable of learning from large amount of historical data to correct the bias in ongoing prediction task. The findings indicated that this technique successfully increased the RA's operational flexibility and response time while reducing excessive vibration [10].

Numerous researchers have also focused on enhancing the RA anti-interference tracking capabilities. Lei et al. [11] proposed a particle-swarm-based RA parameter algorithm optimization technique to increase the precision of joint position and velocity prediction accuracy. The findings illustrated that this method effectively addressed the effects of angular friction, self-weight, and inertia on trajectory deviation, thereby improving the tracking accuracy [11]. Liu et al. [12] developed a kinetic model based on moment calculations to quantify the influence of Coriolis and centrifugal forces on RA motion. The strategy was found to be effective in realizing moment compensation, ensuring regular control, and preventing tracking deviation. Liu et al. [13] proposed

a distributed neural adaptive fault-tolerant control method for multi-flexible RAs under combined interference from actuator failures, input saturation, and external disturbances. By employing a second-order auxiliary system to eliminate input saturation effect and reconstructing boundary dynamics as a second-order system using proportional-integral auxiliary variables″, the results successfully achieved cooperative fault-tolerant control in networked flexible RA systems. Liu et al. [14] proposed a hybrid control strategy using an infinite-dimensional disturbance observer for the vibration suppression and attitude tracking control of flexible RAs under external disturbances. The research established a mixed dynamic model that coupled partial and ordinary differential equations. Two types of control laws were designed to suppress vibration: boundary and distributed. The results verified global asymptotic stability and effectiveness in vibration suppression. In another work Liu et al. [15] proposed a boundary control strategy based on perturbation observers to address the vibration suppression issue in axially moving RAs with input constraints. Their research aimed to minimize the vibration offset of the RA's flexible components by designing boundary control laws and introducing auxiliary terms to address the actuator input saturation limit. Experimental validation confirmed the proposed approach's capability to achieve high-precision control of complex flexible mechanical systems in challenging conditions.

In summary, many methods have been proposed to address RA environmental constraints and tracking control strategies, contributing to the advancement of intelligent robotics. However, existing research still face limitations in maintaining high tracking control performance under compound disturbances and continuous operation requirements. In many cases, control accuracy and stability remain insufficient for the existing operational demands. To address these challenges, this study proposes a kinematic-based tracking control method for RA under multiple environmental constraints. It aims to enhance stability and control accuracy of the RA under multiple environmental constraints and composite interference conditions. The key innovation lies in the development of an RA dynamic simulation model capable of adapting to diverse environmental constraints while mitigating the effect of multiple disturbing factors. Moreover, the integration of multiple controllers reduces tracking errors and ensures the continuity and reliability of RA joint motion in multiple operation processes. The primary research contribution lies in the construction of perturbation trackers and error feedback controllers (EFCs), which effectively minimize tracking errors, ensure the continuity and reliability of the robotic arm's joint motion, and improve the adaptability under complex disturbance conditions. Compared to existing control schemes, the proposed method greatly improves RA's operational stability and tracking control performance in complex environments. It does so by enhancing prediction accuracy, reducing error, and minimizing control lag.

2 METHODS

In this section, the improved Denavit-Hartenberg (D-H) parametric method is first applied to construct the RA linkage coordinate system (CS), with its feasibility verified using both forward and inverse kinematics. The RA workspace is further derived to optimize its structural parameters. Subsequently, joint velocities and spatial mapping are performed using Jacobian matrix. Finally, trajectory planning is implemented using the fifth-degree interpolation method. To mitigate errors caused by various disturbing factors, an anti-disturbance tracker is employed in combination with adaptive tuning and a proportional-integral-derivative (PID) control strategy.

2.1 Modeling of Operational RA Kinematics Based on Multi-Environmental Constraints

At present, coal mining environments are still harsh and complex, which makes RAs susceptible to interference from internal and environmental factors. Therefore, the operational RA performance requirements have become increasingly stringent to ensure efficiency and safety in coal mining processes [16]. To construct a simulation model of an RA under multi-environmental constraints, it is essential to consider its full operational sequence. The main operation process begins with extending the RA to reach the target position, followed by fine-tuning the position using an adaptive control (AC) tracker. A camera is then used to detect the roadway conditions. Once the target hole is reached, the RA is used for ore excavation and handling [17]. The study begins with the structural design of the RA to satisfy the coupling with multi-environmental constraints [18]. Based on the improved D-H parameters (DHPs), the RA linkage CS is established on the three RA models, with the coordinate axes directions specified, as shown in Fig. 1 [19].

According to the RA linkage CS established in Fig. 1, the angular and linear parameters for each joint of RA are determined. Since the RA consists of multiple connecting rods and joints, a right-angle CS is established for each joint. Therefore, the positions and orientations of connecting rods and joints can be expressed using homogeneous transformation matrix to obtain the RA end position and orientation as shown in Eq. (1).

$$ {}_{i}^{i-1}T = \begin{bmatrix} \cos\theta_i & -\sin\theta_i\cos\alpha_i & \sin\theta_i\sin\alpha_i & a_i\cos\theta_i \\ \sin\theta_i & \cos\theta_i\cos\alpha_i & -\cos\theta_i\sin\alpha_i & a_i\sin\theta_i \\ 0 & \sin\alpha_i & \cos\alpha_i & d_i \\ 0 & 0 & 0 & 1 \end{bmatrix}. \quad (1) $$

Here, ${}_{i}^{i-1}T$ is the expression of the degree of association between two connecting rod coordinates i and $i-1$. θ_i is the angle of rotation of the Z_i rod around the X_i rod connected to the same joint. α_i is the angle of rotation of the X_i rod around the Z_i rod attached to the same

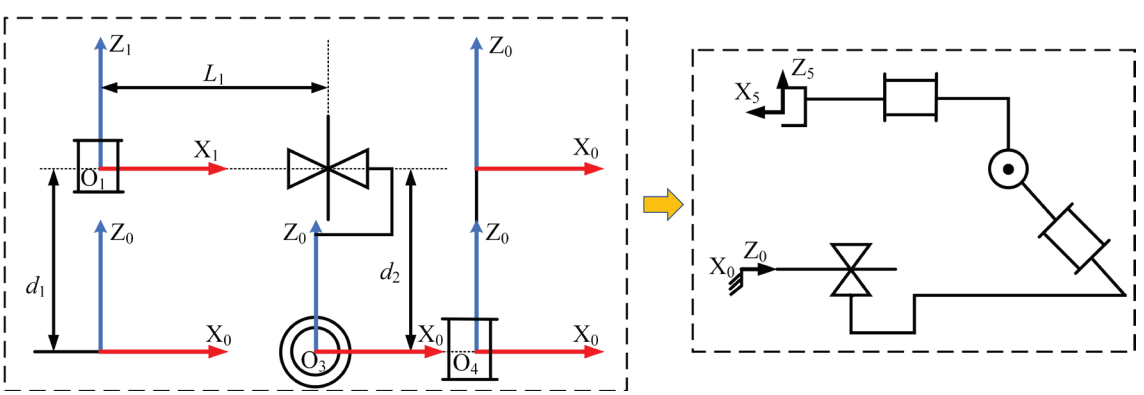

Fig. 1. Structural diagram of the coordinate system of the RA

joint. d_i denotes the displacement length along the X_i axis in the joint CSi. The established RACS and the final orientation are verified by positive kinematics. The positional-orientation correlation matrix of the RA can be obtained by substituting the joint angle (JA) parameters obtained from the CS established by improving the DHP into the transformation matrix and multiplying them as shown in Eq. (2).

$$\begin{bmatrix} {}^0R & {}^0P \\ 0 & 1 \end{bmatrix} = \begin{bmatrix} n_x & o_x & a_x & p_x \\ n_y & o_y & a_y & p_y \\ n_z & o_z & a_z & p_z \\ 0 & 0 & 0 & 1 \end{bmatrix}. \tag{2}$$

Here, n represents the unit direction vector of the X-axis of the end effector CS, o represents the unit direction vector representing the Y-axis of the end effector CS, a represents the unit direction vector representing the Z-axis of the end effector CS, p represents the origin position of the end effector CS, ${}^0R$ represents the final posture obtained by the robotic arm, and ${}^0P$ represents the final position obtained by the robotic arm. JA is a known parameter because the RA rotation angle has been obtained through the linkage CS at the beginning. The final position of the RA can be obtained by substituting the known JAs into its sub-transformation matrix. Thus, the positive kinematic analysis (KA) of the RA model can be verified. The following inverse KA of the RA is carried out. The six-degree-of-freedom joint rotation simulation model of the RA is constructed by applying MATLAB/Simulink R2022a, as shown in Fig. 2.

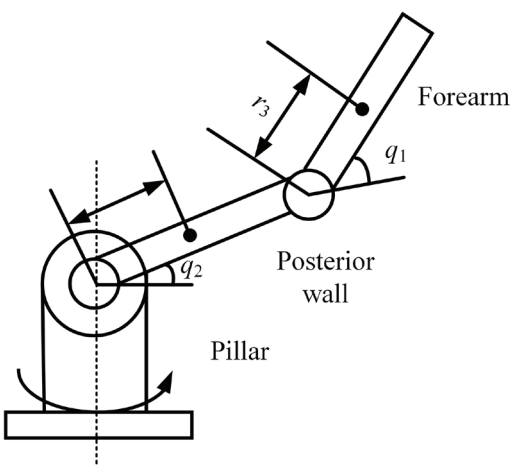

Fig. 2. Schematic diagram of a RA with two rotational joints

After the robot joints are built in MATLAB using DHP, the *Link* function is used to generate the associated connecting rods around the joints. Then the *Serial* class function is used to connect the joints and their corresponding connecting rods to form a complete robotic arm simulation model (RASM). The joint rotation angle (JRA) of the RASM is assumed to be 0°. Then the final position and orientation of the RA are obtained by solving its sub-transformation matrix using the kinetic *fkine* function, as shown in Eq. (3).

$$T = \begin{bmatrix} 1.000 & 0 & 0 & 0.196 \\ 0 & -1.000 & 0 & 0.038 \\ 0 & 0 & -1.000 & 0.052 \\ 0 & 0 & 0 & 1.000 \end{bmatrix}. \tag{3}$$

Here, T is the final position and orientation of the RA obtained by inverse KA. The simulation model's accuracy is evaluated by comparing its results with the final data obtained from the homogeneous transformation matrix corresponding to the inverse KA process, as described in reference [20]. To ensure the precise RA's handling and grasping of targets during the mining operation, additional control over its characteristics must be applied throughout its movement.

The RA simulation dynamics model is developed in MATLAB with the initial position defined as the starting point. Equation (4) illustrates the application of the fifth-degree polynomial interpolation approach to normalize the parameters associated with the motion velocity, acceleration, and final position of the RA.

$$\theta(t) = A_0 + A_1 t + A_2 t^2 + A_3 t^3 + A_4 t^4 + A_3 t^5. \tag{4}$$

Here, $\theta(t)$ denotes the JRA of the RA at time t. A_0 to A_5 denote the CSs of the corresponding link numbers, respectively. The structural parameters defined during robot planning are then used to generate the RA workspace. The rationality and correctness of the post-configuration structure are verified, and the details of the structure are further optimized. Following joint velocity calculation and spatial mapping via Jacobian matrix, the differential motion position of RA is obtained. Motion process optimization is then carried out as shown in Eq. (5).

$$F(x) = \alpha f_1(x) + \beta f_2(x). \tag{5}$$

Here, α and β denote the weighting coefficients. $F(x)$ represents the objective function to be optimized, while $f_1(x)$ refers to the matrix condition number, and $f_2(x)$ refers the blind zone of RA in the range of operating space. Given that the RA joint motion parameters are known, the joint moments are derived as shown in Eq. (6).

$$\tau = G(q) + V(q, \dot{q}) + M(q)\ddot{q}. \tag{6}$$

Here, τ denotes the joint moment, $M(q)$ represents the inertia matrix, and q. $\dot{q}$ and $\ddot{q}$ correspond to the joint gravity, inertia and centripetal force, respectively. $G(q)$ is the gravity vector, while $V(q, \dot{q})$ is the velocity of motion. This study explores decoupling calculations for joint torques using inverse dynamic analysis of the Jacobian matrix to address the dynamic coupling effect among multiple joints. In particular, the joint torque model is used to separate the inertia matrix, Coriolis force, and centrifugal force term. A feedforward compensation strategy is than implemented to compensate for the coupling torque of each joint in real time. Additionally, when used with the adaptive controller's online parameter adjustment function, this approach corrects nonlinear interference caused by joint coupling in real time. This reduces the influence of one joint on another.

2.2 Anti-Jamming-Based Trajectory Planning Strategy for Operational RA

The above study constructs a RASM that satisfies the forward and inverse dynamics. To further increase the usability of RA-based mining operations, the constructed RASM is next employed for motion trajectory planning and tracking control, as outlined in Fig. 3.

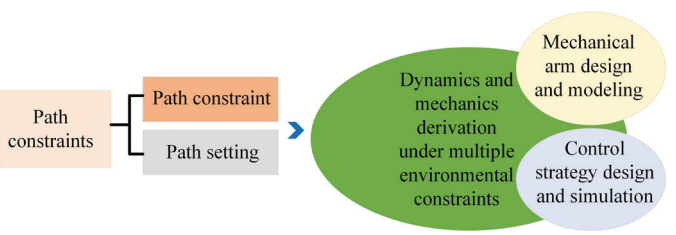

Fig. 3. Trajectory planning process diagram

Since the RA is mainly used to replace manual labor in hazardous production environments, it must operate reliably under dangerous and uncontrollable conditions [21]. Further adjustment and control of model parameters and motion states are required to enable robots to operate efficiently under such complex working conditions while

maintaining accuracy and flexibility comparable to that of human operators [22].

As illustrated in Fig. 3, the trajectory control process of the robotic arm is complex and intricate undertaking involving several key stages. These include the construction of the robotic arm simulation model, defining path constraints and settings, performing trajectory planning, implementing trajectory tracking and control, adjusting and optimizing parameters, and other critical tasks. By following the aforementioned steps, the robotic arm can achieve precise and efficient operation even under complex working conditions. Given the complexity of the operating environment, the process begins with planning an anti-interference route for the robot. Subsequently, an anti-disturbance tracker is designed to account for environmental noise amplification, thereby increasing the flexibility of the robot to the environmental conditions. This is shown in Eq. (7).

$$\begin{cases} \dot{\zeta}_1(t) = \zeta_2(t) \\ \dot{\zeta}_2(t) = -\gamma^2(\zeta_1(t) - v_k(t)) - 2\gamma\zeta_2(t) \end{cases}. \tag{7}$$

Here, $\dot{\zeta}_1(t)$ and $\zeta_2(t)$ denote the predicted speed and acceleration of the RA, respectively, $v_k(t)$ is the actual tracking speed, and γ refers to the influencing factors affecting tracking performance. To increase RA stability, a composite observer is used to predict and compensate for its interference, as shown in Eq. (8).

$$\begin{cases} \dot{\xi}(t) = -L^*(\xi(t) + p(x)) \\ \hat{d}_1(t) = \xi(t) + p(x) \end{cases}. \tag{8}$$

Here, $\hat{d}_1(t)$ and L^* are the predicted and actual values of environmental disturbances, respectively, $p(x)$ denotes the non-linear relationship among environmental factors, and $\dot{\xi}(t)$ denotes the observed intermediate variable. The disturbance prediction gain of the composite observer is shown in Eq. (9).

$$L = \frac{\partial p(x)}{\partial x}. \tag{9}$$

The anti-disturbance tracker is used to cope with the prediction and control environmental uncontrollable factors, incorporating adaptive tuning to address the drawback of feed-forward and robustness compensation. Adaptive tuning for controlling nonlinear factors in the RA has proven effective in the absence of time-varying external disturbances. However, in practical application scenarios, numerous operational errors and external state disturbances interfere with the control process, necessitating robust engineering [23,24]. The error values are output with an anti-disturbance tracker, as shown in Eq. (10).

$$e_1(t) = x_1(t) - z_1(t). \tag{10}$$

Here, $e_1(t)$ denotes the error value of the speed estimate, $x_1(t)$ represent the nonlinear relationship of the observed disturbances, and $z_1(t)$ is the actual disturbance factor output. To enhance robustness among independent joints, the entire RA operation process is controlled using the PID strategy following the motion-state decomposition of each joint. Then, the focus of control shifts to the telescopic joints. There, a backstepping adaptive method is applied to identify and adjust the parameters associated with the uncertainty factors of joint motion. The principle of PID control strategy is shown in Fig. 4.

As illustrated in Fig. 4, the PID control system primarily regulates the actual motion state of the telescopic joint by modulating the driving torque of the motor, thereby facilitating accurate tracking of the robotic arm. In particular, the PID controller consists of multiple PID control modules. Each module receives position and velocity error signals and calculates the corresponding control input to adjust the driving torque. This controls joint velocity and position. The backstepping AC approach is a recursive design method for uncertain control systems. It is based on the RA state feedback mechanism and addresses controller stability issues [25,26]. The principle of the method is shown in Fig. 5. The method begins by converting the complex motion states into simple sub-states using the RA state equation. The intermediate sub-states are then controlled using a virtual control law derived from the Lyapunov function. After updating the error-controlled sub-states, the entire motion state is controlled by recursive behavior, enabling the formulation of a complete control law for the overall system.

Inverse step adaptation effectively overcomes the functional control limitations of the controller. Noise measurements are performed across all sub-states of the RA, and all identified noise components of uncertainty are integrated into the external disturbance moment [27,28]. As a result, the RA dynamics equation is formulated in Eq. (11).

$$J\ddot{\theta}_L = \frac{1}{n}T_m - B\dot{\theta}_L + T_{dis}. \tag{11}$$

Here, $\ddot{\theta}_L$ and $\dot{\theta}_L$ denote the angular displacement and velocity of the RA load axis, respectively, J represents the gravity vector, T_m represents the input moment, B represents the time-varying component, T_{dis} represents the output moment, and n represents the joint variable. Parameter adjustment is performed using a hierarchical optimization strategy. The PID gains are initialized based on the frequency domain response [29], the adaptive rate matrix weights are optimized using the particle swarm optimization (PSO) algorithm, and the robust interval of the perturbation observation gain is verified using Monte Carlo sampling [30]. For AC addressing parameter

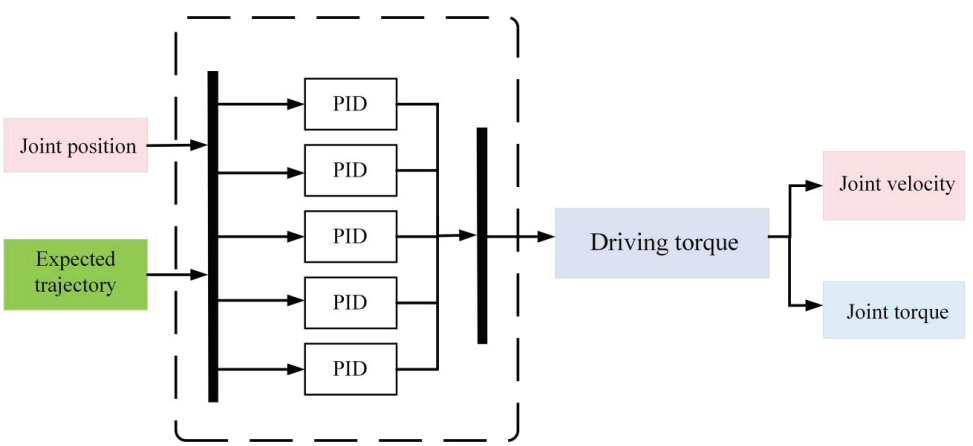

Fig. 4. Schematic diagram of PID control strategy

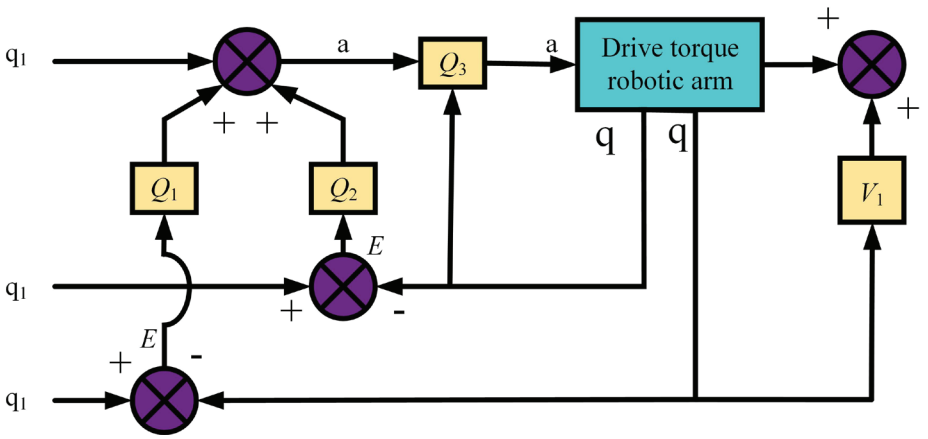

Fig. 5. Schematic diagram of back-stepping adaptive control

uncertainties in the controller, the first step is to define the final angle, as shown in Eq. (12).

$$\theta \in \Omega_\theta \triangleq \{\theta : \theta_{\min} \le \theta \le \theta_{\max}\}. \tag{12}$$

Here, Ω_θ denotes the set of robotic arm joint rotation angles (RAJRAs). θ denotes the current RAJRA. $\theta_{\min}$ is the force matrix of the minimum rotation angle within 1, 2, and 3 minutes. $\theta_{\max}$ is the force matrix for the maximum rotation angle over the same time intervals. The second step involves the Lyapunov function error expressed in Eq. (13).

$$V_2 = V_1 + \frac{1}{2}\theta_1 p^2 + \frac{1}{2}\tilde{\theta}^T \Gamma^{-1}\tilde{\theta}. \tag{13}$$

Here, V_1 and V_2 denote the angular velocity before and after control, respectively, θ_1 represents the current true JRA, $\tilde{\theta}$ is the error between the true angle and the predicted angle, and $\tilde{\theta}^T$ is the transpose of the JRA error. To ensure the stability of the Lyapunov-based control method, the quadratic function of the system state error is selected as the Lyapunov candidate function. This function includes a weighted sum of the squared of the JA error, angular velocity error, and parameter estimation error. By taking the derivative of the Lyapunov function along the closed-loop system trajectory and substituting the adaptive and backstep control laws, it is proven that the derivative consists of a negative-definite component from the error term and the bounded term from parameter estimation error. According to Barbalat's lemma, the joint angular error and the angular velocity error asymptotically converge to zero. This ensures that the negative semi-definite property of the Lyapunov function derivative is preserved under parameter uncertainty, thereby ensuring global asymptotic stability of the closed-loop system. Γ^{-1} denotes the inverse of the adaptive matrix of the controller parameters. The adaptive law governing the parameter matrix is shown in Eq. (14).

$$\dot{\hat{\theta}} = \Gamma \varphi p. \tag{14}$$

Here, $\dot{\hat{\theta}}$ denotes the adaptive law, Γ is the adaptive matrix of controller parameters, φ represents the error value between two adjacent sub-states, and p is the error value between two sub-states of RA. To cope with the constraints of the complex environment, the anti-interference tracker dynamically adjusts the trajectory interpolation parameters by monitoring the relative distance between the end of the robotic arm and the obstacles in real time. When path conflicts are detected, the adaptive controller triggers online parameter correction, re-plans the local path and constrains the joint acceleration to ensure the smooth movement of the robotic arm within a limited space. Meanwhile, the PID controller suppresses the nonlinear disturbances caused by sudden changes in constraints through error feedback, maintaining end-effector positioning accuracy. Analysis of the time derivative of the dynamic equation and the Lyapunov function show that, when combined with the adaptive law and JA constraint conditions, the quadratic function of the system state error retains a negative semi-definite characteristic [31]. According to Barbalat's lemma, as time approaches infinity, the system state error converges to zero. Under this condition, the control torque boundary is determined by three factors: the upper bound of the spectral norm of the system inertia matrix, the upper bound of the gravity term, and the upper bound of the disturbance observer's compensation torque. These factors ensure the control signal remains bound in the closed-loop system. For parameter adjustment and robustness enhancement, a hierarchical optimization strategy is employed. PID gains are initialized via frequency-domain response analysis, and the hierarchical optimization boundary is set to a step response overshoot of less than 15 % and a rise time of less than 0.1 s. The weight optimization of the adaptive rate matrix is optimized using the PSO algorithm. The objective function is defined as the weighted sum of the absolute error of the integral tracking performance and the energy consumption, and the number of iterations is set to 200. The robust interval of the perturbation observation gain (nominal value ±10 %) is verified by Monte Carlo sampling (sample size $N = 1000$), which evaluates the system stability under parameter perturbation. Sensitivity analysis disturbance conditions−such as ±20 % uncertainty of joint inertia and ±15 % deviation of load mass− are based on variation ranges observed in coal mine operations. The trade-offs in tuning are carefully considered. Increasing proportional gains improves steady-state accuracy, but it also increases the risk of overdraft and oscillation. Improving the adaptive rate can accelerate convergence, but it also raises the computational load. Expanding the robust gain range improves immunity to interference, but it may also reduce nominal performance. The selected technology has proved effective for dealing with multi-objective constraint problems [32]. The method demonstrates robustness by maintaining a trajectory tracking error below 2 % under the following disturbance conditions: uncertainty in joint inertia of ±20 %, deviation in load mass of ±15 %, position error of obstacles of no more than 0.2 meters, and a sudden change in light intensity of no more than 3000 lux. The computational complexity of the research methods mainly stems from the collaborative optimization of multiple controllers, real-time disturbance observer prediction, and dynamic adaptive parameter adjustment. Specifically, the fifth-degree interpolation method reduces the computational complexity of trajectory planning from traditional cubic interpolation $O(n^3)$ to $O(n^2)$ by imposing high-order smoothing constraints on the

joint motion trajectory. At the same time, it reduces the number of redundant computing nodes.

In actual coal mining operations, RA uses visual modules and LiDAR to collect real-time spatial information about the roadway. This data is used to identify the obstacle positions and assess lighting conditions, enabling initialization of the DHP model. Smooth joint trajectories are generated using a fifth-degree interpolation method, while the anti-interference tracker dynamically adjusts the interpolation parameters according to the environmental noise. When an obstacle is detected unexpectedly, the adaptive controller triggers local path replanning, constrains joint acceleration, and prevents collisions. The PID controller adjusts the driving torque of each motor joint in a closed-loop manner. Meanwhile, the backstepping adaptive controller adjusts the inertia matrix parameters in real time to accommodate sudden changes in load mass. The disturbance observer, using a composite observation gain, compensates for both weight of the robotic arm and external vibration interference.

3 RESULTS AND DISCUSSION

This section begins by evaluating the performance of the adaptive controller, the fifth-degree interpolation method, and the dynamic function used in the construction of RASM. Next, the actual operational performance of each joint in the simulation model is compared and analyzed. Finally, the RASM is tested under both internal and external disturbance environments, and its performance is compared with other tracking control strategies for comparative analysis of the error control effect.

3.1 Kinematic Modeling Test

The scaled-down test rig is used to simulate the actual working conditions, and the RASM is constructed in MATLAB based on the DHP table. The simulation model is tested to obtain the torque values of each joint of the RA. The simulation model of the RA structural design is verified in real mining environments. After validating both forward and reverse dynamics of the RA, the stability and accuracy of the RA in practical applications are further tested using collected data. Table 1 displays the RA's three-dimensional model derived from the DHPs of the connecting rod CSs.

Table 1. DHP parameter table of RASM

Joint	Joint angle	Z-axis offset [mm]	X-axis offset [mm]	Rotation angle around the X-axis	Range of variation
1	0°	0	1356	0	2000 mm
2	90°	0	3467	45	200 mm
3	0°	148	1732	45	−45°∼45°
4	0°	156	1246	0	3000 mm

The insufficient number of control parameter settings for RA can result in large errors, while excessive loading times in the simulation software slow down model construction. To address these issues, the loading time of the simulation RA model construction is set to 10 s, and the robot displacement step is set to 250. Figure 6 presents the RA simulation structural model, which is based on the Lyapunov function in the adaptive controller. The model illustrates the four workflow processes of telescoping, moving, digging, and carrying. The robotic arm consists of four links with simulated masses of 12.5 kg, 8.2 kg, 6.8 kg, and 4.5 kg, and corresponding lengths of 1356 mm, 3467 mm, 1732 mm, and 1246 mm, respectively. Simulation results indicate that the thrust peaks during telescopic operation are 14,275 N and 13,968 N. The screw torque peaks of mobile operation are 0.1553 Nm and 0.0613 Nm. The screw torque poles of mining operation are 0.9324 Nm and 0.9957 Nm, and the screw torque peaks of handling operation are 0.1677 Nm and 0.1346 N.m. The model illustrate the four workflows. This results confirm that the constructed RASM structure meets the practical requirements of mining operation.

To investigate the effectiveness of the fifth-degree interpolation method used in this study for motion constraint control during RA operations, a comparative analysis is conducted against third-, seventh- and ninth-degrees interpolation methods. Joints 1, 2, and 3 are selected as the test subjects and the fluctuation magnitude of each joint's velocity profile over time is used as the evaluation index. The results are shown in Fig. 7. Application of the interpolation method at different time steps constraints the RA joint motion range, ensuring that the joint curve remains smooth and continuous. Among them, the three times interpolated terminology method shows the weakest constraint performance, with large fluctuations occurring at the start and end of motion. The velocities of Joints 1, 2, and 3 increase from 0 $m \cdot s^{-1}$ to 0.45 $m \cdot s^{-1}$, 0.09 $m \cdot s^{-1}$, and 0.42 $m \cdot s^{-1}$, respectively. The fifth-degree interpolation method demonstrates the best performance, minimizing motion fluctuation in ranges between [−0.2 $m \cdot s^{-1}$, 0.2 $m \cdot s^{-1}$]. Compared with the fifth-degree method, the constraint performance of seven-degree and nine-degree interpolated method improves by 2 % and 3 %, respectively. Furthermore, the fifth-degree interpolation method reduces power consumption and improves the system's energy efficiency ratio while maintaining efficient control. Therefore, the proposed fifth-degree interpolation method offers both high application effectiveness and economic advantage.

To further verify the effect of the interpolation order on RA power consumption, a comparison is made between the third-, fifth- and seventh-degree interpolation methods to verify the superiority of the fifth-degree method. Four different working conditions are used within the same RA application scenario, and the corresponding RA power and time curve are presented in Fig. 8. Among them, Condition 1 is the maximum range of telescopic motion of the robotic arm in an unloaded state; Condition 2 is the extension and contraction motion of the robotic arm under rated load, simulating pushing or supporting operations; Condition 3 simulates the action of drilling or cutting coal and rock using the end effector of the robotic arm; Condition 4 is for the robotic arm to grab and transport materials. Under the four working conditions shown in Fig. 8, the three interpolated term methods exhibit the lowest energy consumption, the seventh-degree method the highest, and the fifth-degree the moderate level. The energy consumption of the three interpolated methods at Condition 1 is 46.37 J, 54.76 J, and 87.45 J, respectively. Compared to the third-degree method, the fifth-degree method improves by 20.32 % while it reduces consumption by 70.23 % compared to seventh-degree method. Across all conditions shown in the figure, all three interpolated methods exhibit the same power consumption results under four different operating conditions, with deviations within 5 %. Although the seventh-degree interpolation method consumes significantly more power than the other two, it does not yield substantial improvement in joint control performance. Therefore, the fifth-degree interpolation method is considered the most reasonable choice, offering a balanced trade-off between control performance and energy efficiency.

To verify the effectiveness of the PID controller perturbed by non-linear environmental factors, the displacement versus time curves of four different joints is analyzed. Moreover, the RA trajectory planning error is combined before and after applying the PID control strategy. The results are shown on Fig. 9. The actual and predicted trajectories of the RA almost completely overlap, with error values not exceeding 5 %. In Fig. 9a, the displacement of Joint 1 reaches 4.2 m with the largest error approximately 0.4 m between actual

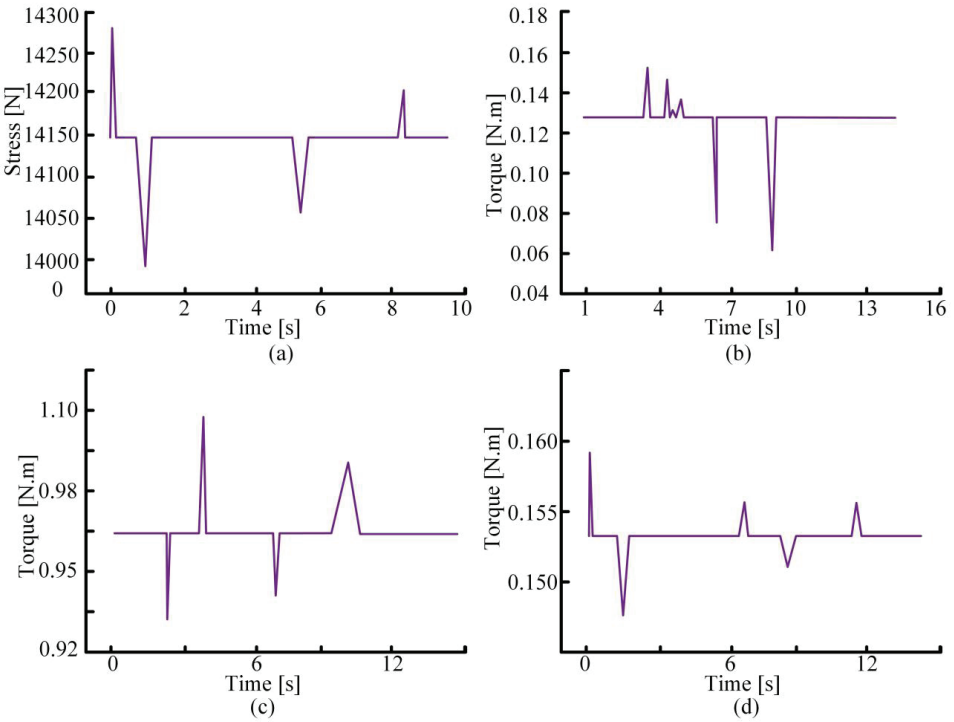

Fig. 6. Dynamic simulation experiment analysis of edge cutting robot; the operational motion process of robot arm simulation structure model in: a) expansion and contract, b) move, c) excavate, and d) carry

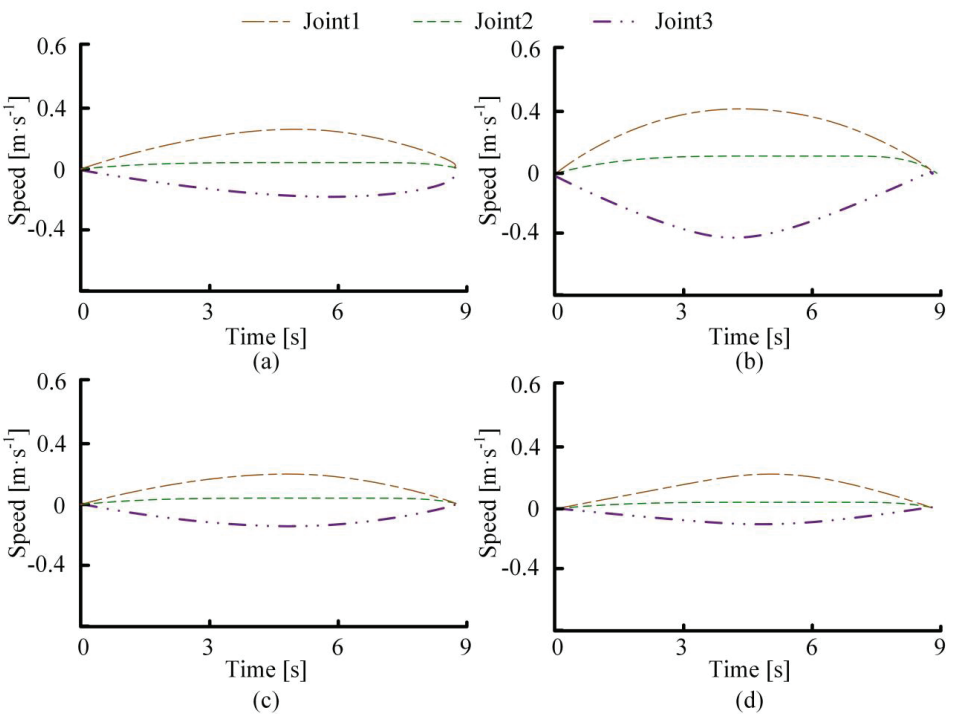

Fig. 7. Comparison of motion speed curves under different interpolation methods: a) fifth degree interpolation method, b) third degree interpolation method, c) seventh degree interpolation method, and d) ninth degree interpolation method

and predicted values. In Figs. 9b and c, Joint 2 exhibits the smallest error, with its actual and predicted displacement curves highly overlapping and differing by less than 0.1 m. Joint 2 and Joint 3 show similar intermediate-level differences, with differences within 1 m. The findings demonstrate the high feasibility of the suggested PID controller in suppressing the environment's unpredictable non-linear variables.

A sensitivity analysis of the key control parameters reveals that increasing the proportional gain from 50 to 70 reduces the steady-state error by 33 % but also raises the overshoot from 4 % to 8 %. Similarly, increasing the adjustment coefficient of the adaptive rate

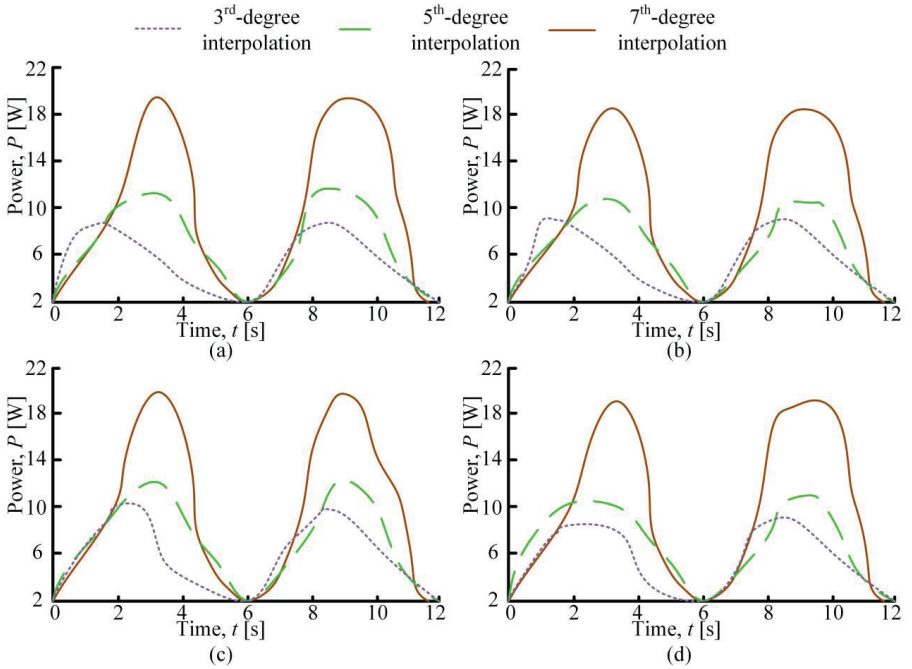

Fig. 8. Power consumption curves of the robot applying the three interpolated term methods at working conditions: a) Condition 1, b) Condition 2, c) Condition 3, and d) Condition 4

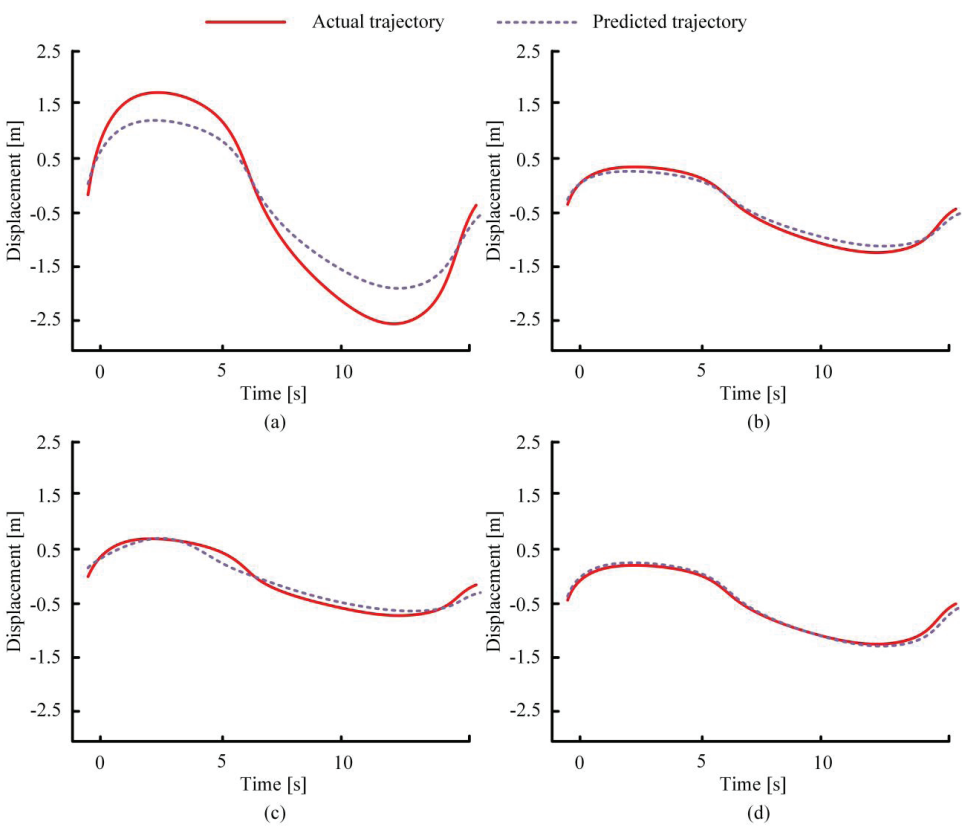

Fig. 9. Performance tests under PID control of RA using: a) displacement curve of joint 1 over time, b) displacement curve of joint 2 over time, c) displacement curve of joint 3 over time, and d) displacement curve of joint 4 over time

matrix increases from 0.5 to 1.0 shortens the convergence time by 22 %, though it increases the computational load by 15 %. Adjusting the disturbance observation gain within ±10 % of the nominal value results in the compensation efficiency of no more than 5 %.

3.2 Practical Application of RASM for Mining Exploitation

After testing the RA model kinematic model, the next step is to verify the motion trajectory error (TE) values of each joint in the simulated robot under externally disturbed conditions. A performance

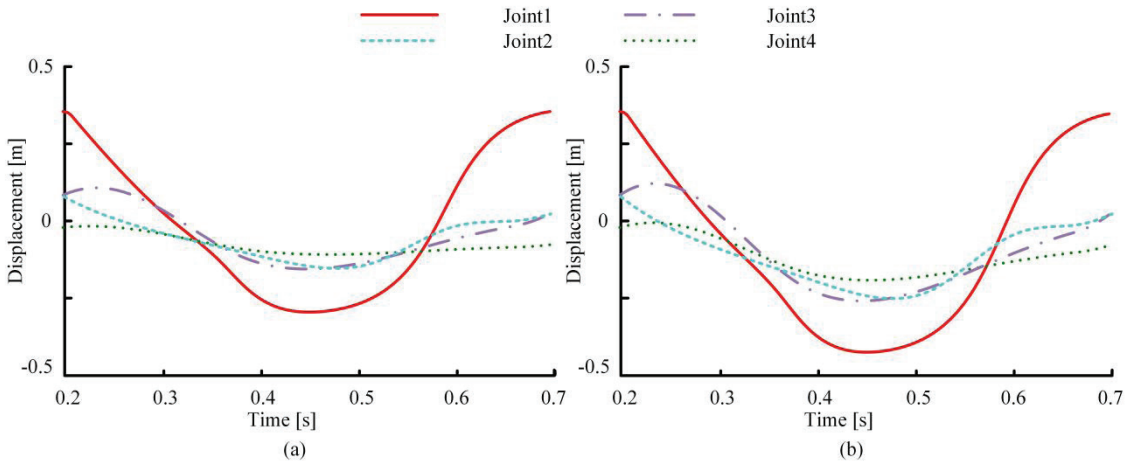

Fig. 10. Comparison of joint error curves under external disturbance conditions; error value of motion trajectory under different environmental conditions a) daytime, and b) nighttime

comparison is conducted between daytime and nighttime environment, and the results are shown in Fig. 10. The fluctuation range of the error value of each joint over time remains in the range of [−0.5 m, 0.5 m]. The largest fluctuation error is observed in Joint 1, reaching an extreme value of −0.4 m at the 0.4-second mark. This is caused by transient motion instability during the initial startup process. The smallest difference occurs in Joint 4, within 0.1 m, due to the adaptive feedback mechanism, which gradually reduces the error. The error values for joints 2 and 3 are medium, ranging from −0.1 to 0.1 m. The RA shows slightly larger errors at night compared to daytime due to reduced camera image acquisition accuracy caused by lower light levels. However, the difference is minimal, within 0.1 m.

To verify the dynamic control effect of the *Simscape* dynamic function applied to the RASM, four rounds of parameter debugging are carried out for each of the four different joints. Comparison and analysis of the positional error over time for each joint during the debugging process is performed, with the results shown in Fig. 11. From the debugging process graphs can be observed that the position errors of the joints gradually converge as the number of debugging times is increased. Among them, the error reduction ratio for Joint 1 is 2 %, 4 %, 3 %, and 1 % when the number of debugging times is 1, 2, 3, and 4, respectively. Moreover, it reaches a stable state in the first 0.2 s, with the best convergence effect. Joint 4 has the slowest convergence only reaching a steady state within 0.4 s. Moreover, its performance is enhanced by an average of 1 % per debugging iteration within the expected range. The debugging performance

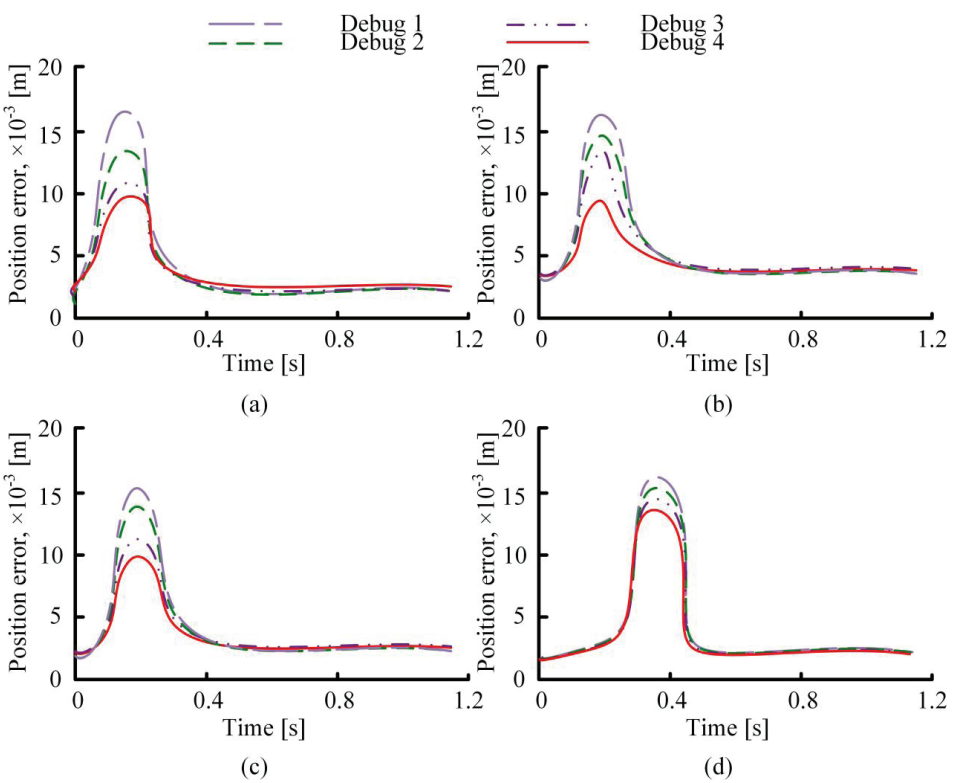

Fig. 11. Comparison of dynamic control effects of different joints; the variation of position error of joints over time during the debugging process: a) Joint 1, b) Joint 2, c) Joint 3, and d) Joint 4

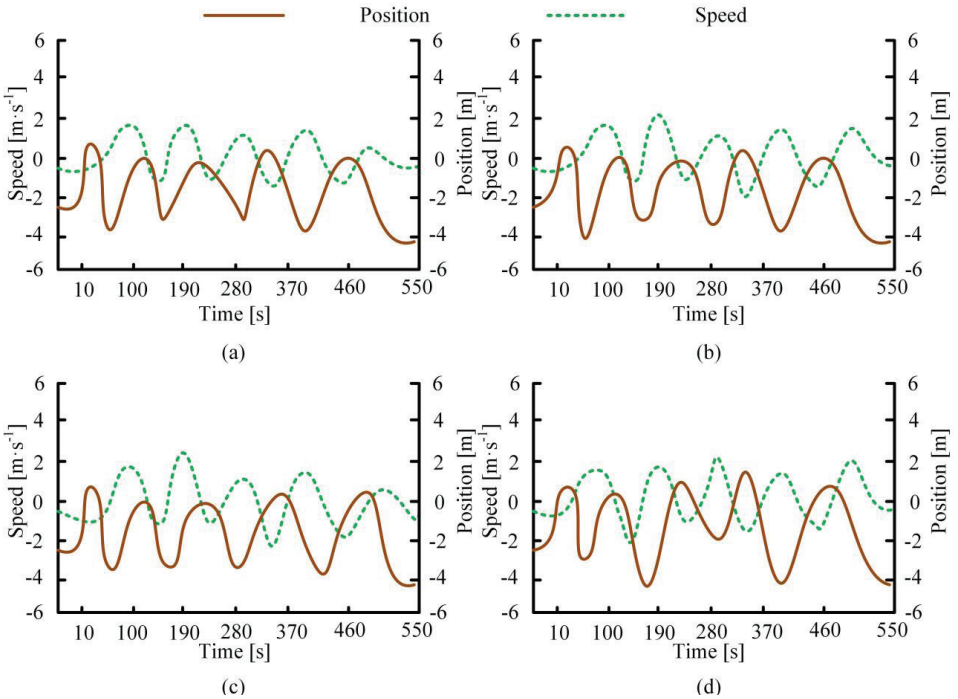

Fig. 12. Comparison of motion continuity under different numbers of obstacles in the paths; Speed and position fluctuation curve of: a) Path 1, b) Path 2, c) Path 3, and d) Path 4

of Joints 2 and 3 shows intermediate performance, stabilizing within 0.3 s and improving performance by an average of 4 % per debugging iteration. All four joints show a performance improvement of over 1 % during each debugging cycle. The results confirm that the proposed *Simscape* dynamic function provides high accuracy and stability for RA error control.

To verify the smoothness of the constructed simulated RA model in terms of joint position and velocity along the obstacle path, four different paths with progressively increasing numbers of obstacles are compared and analyzed. Velocity and position fluctuation curves are used as evaluation indexes, with the results shown in Fig. 12. In Fig. 12a, exhibits the highest stability, with velocity and position fluctuations limited to [$-2\,m{\cdot}s^{-1}$, $2\,m{\cdot}s^{-1}$] and [$-4\,m{\cdot}s^{-1}$, $1\,m{\cdot}s^{-1}$], respectively. Path 4 presents largest fluctuation, with maximum displacement of −4.5 at both 180 s and 380 s, respectively. Paths 2 and 3 show intermediate fluctuation level with velocity and position ranges of [$-2.5\ m{\cdot}s^{-1}$, $2.5\ m{\cdot}s^{-1}$] and [$-4.5\ m{\cdot}s^{-1}$, $1.5\ m{\cdot}s^{-1}$], respectively. The proposed method allows for the effective planning of trajectories across different paths while keeping velocity and displacement fluctuations within the fixed ranges of [$-4.5\ m{\cdot}s^{-1}$, $1.5\ m{\cdot}s^{-1}$] and [$-2\ m{\cdot}s^{-1}$, $2.5\ m{\cdot}s^{-1}$], respectively. The results demonstrate that the adaptive tuning mechanism employed in this study enables the RA to maintain high stability and performance when navigating various obstacle configurations in real mining operations.

To validate the error control performance of the proposed disturbance tracker for the RA, two additional trajectory tracking methods are used for comparison, namely non-linear disturbance observer (NDO) and extended state observer (ESO). The three controllers are applied across four operational processes, namely, excavation, rotation, translation, and handling. The predicted and actual RA trajectory curves for each process are compared and analyzed, with the findings shown in Fig. 13. Predicted and actual trajectories of the RA across all four workflows exhibit a high degree of overlap, with errors below 2 %. In the excavation process (Fig. 13a), the RA shows the largest TE at 0.5 m. In the rotation and translation workflow (Fig. 13b and c), the smallest TE errors are observed at 0.3 m and 0.2 m, respectively. In the handling operation (Fig.13d), the TE is at the level of 0.1 m. The results suggest that the RA applied in a variety of operational processes achieves consistent accuracy with an error below 2 %, with minor fluctuation in individual processes that are operationally negligible.

The performance of EFC proposed is compared before and after parameter reduction and compared with fuzzy controller (FC). The error between the actual and desired displacement is used as the evaluation index, with the results shown on Fig. 14. Under both larger and smaller parameter conditions, the displacement curves of EFC, FC, and the proposed method all show an initial increase followed by a decrease trend, with a total displacement of 0.8 m. Between 7 s and 15 s, the displacement remains constant at around 0.85 m. After parameter reduction, both controllers show hysteresis compared to the desired displacement, although some improvement in motion continuity is observed. For smaller parameters, the proposed method exhibits a hysteresis of 5 % compared to the desired displacement, while FC shows a hysteresis of 10 %. The results show that the proposed controllers have less hysteresis and are more feasible to be used for practical testing.

To further validate the control performance of the proposed method, two comparable methods are selected, namely AC and sliding mode control (SMC). The AC implementation employs Lyapunov stability theory to design adaptive parameter law, with an update rate of 0.5. The SMC implementation uses an exponential approach law with a switching function gain of 150. Experiments are carried out under four typical mining operation processes (tunneling, rotation, translation, and handling), each repeated 10 times. The same DHPs and initial RA state are used, and the same compound disturbances are applied (±20 % sudden change in joint inertia, ±15 % step change in load, 3000 lux pulse disturbing illumination). The performance evaluation is performed using three evaluation indicators: trajectory tracking accuracy, anti-interference ability, and computational complexity. The results are presented in Table 2. The proposed method has a higher computational complexity, but its

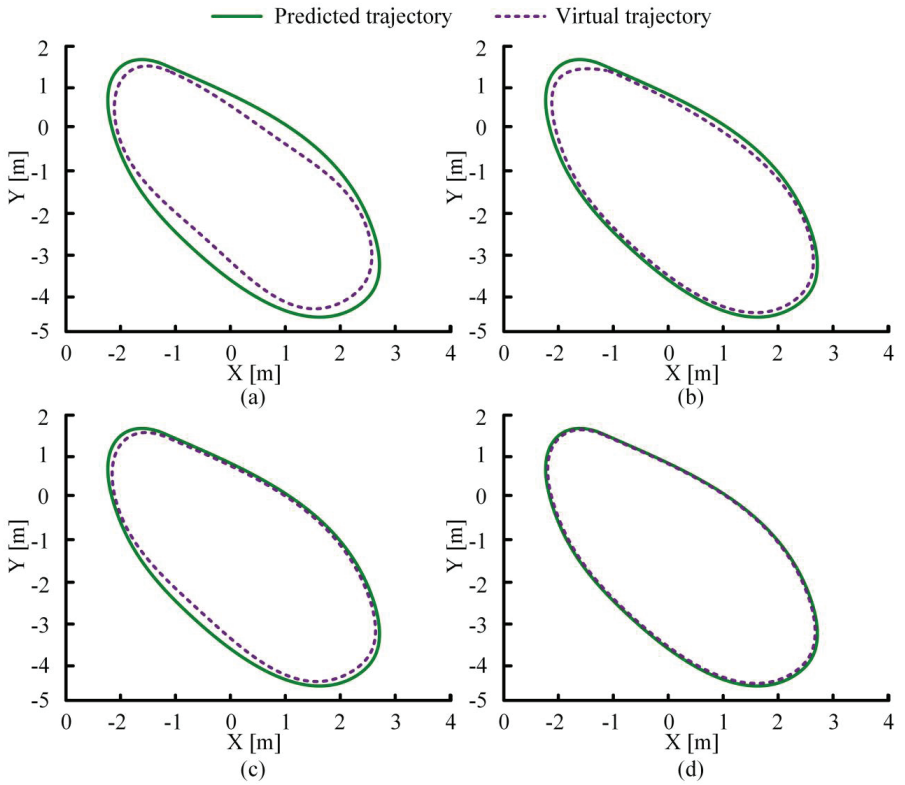

Fig. 13. Error comparison of different trackers; analysis and prediction of trajectory and actual trajectory curve applied to: a) excitation, b) rotation, c) translation, and d) transportation

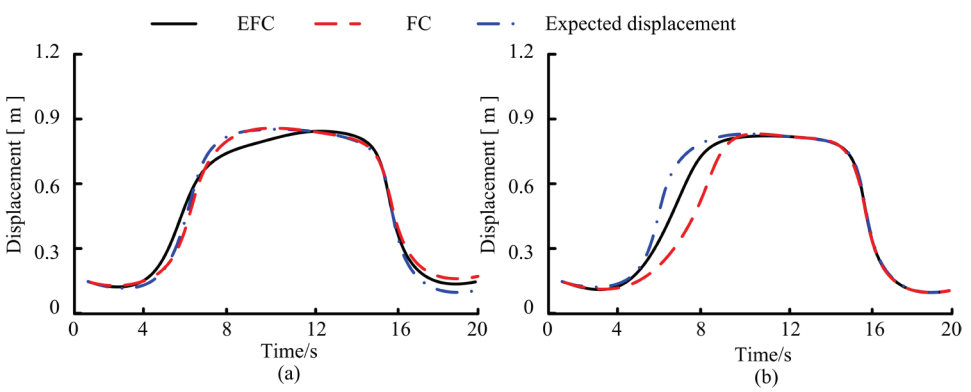

Fig. 14. Comparison of controller parameter size and performance; error between actual displacement and expected displacement under: a) large parameters, and b) smaller parameters

trajectory tracking accuracy is 97 %, which is 10 % and 3 % higher than AC and SMC, respectively. The anti-interference ability is 15 % and 6 % higher than SMC and MEC, respectively. The results indicate that the proposed method can ensure high control accuracy, stability, and reliability in practical control.

To verify the technology's adaptability to the complex environment of a coal mine, simulations were conducted under typical interference conditions, such as fluctuations in dust concentration (50 mg/m^3 to 150 mg/m^3), sudden changes in light intensity (50 lux to 5,000 lux), and mechanical vibrations (5 Hz to 20 Hz). In the simulation, the impact of elevated dust concentration is modeled by accordingly degrading the signal-to-noise ratio (SNR) of the visual feedback module and increasing the joint friction coefficients within the dynamic model. Experimental results show that a peak dust concentration of 150 mg/m^3 causes the end effector's positioning error of 0.18 m. This error increases only by 12 % compared to an ideal environment. When the light intensity is abruptly increased to 5,000 lux, the visual assistance module, using adaptive exposure compensation, maintains the trajectory re-planning delay within 0.2 s. Under continuous vibration interference, the anti-interference tracker reduces the fluctuation amplitude of the joint torque to 28 % of that in the uncontrolled state. These results demonstrate the proposed method can effectively address multi-source, time-varying, and unstructured disturbances in coal mine operations.

Table 2. Performance comparison of various control methods

Control method	Trajectory tracking accuracy [%]	Disturbance rejection capability [%]	Computational complexity (relative value)
AC	87	80	3
SMC	94	89	4
MEC	97	95	2

To verify the superiority of the proposed method, the study further combines it with the advanced model predictive control (MPC), nonlinear active disturbance rejection control (NADRC), and impedance-based method. During the implementation of MPC, a state

space model is established. The prediction time domain is five steps, and the control time domain is two steps. For the implementation of the NADRC, the ESO's bandwidth is set to 20 rad/s. For the impedance-based implementation process, the inertia-damping parameter is set to [15, 0.7] N·s/m. The results are shown in Table 3.

As shown in Table 3, the proposed control method's trajectory tracking error of 3 %, which is 5 % higher than the error of MPC and 8 % higher than that of NADRC. Using a composite observer, it predicts and compensates for disturbances caused by sudden changes in simulated dust concentrations and mechanical vibrations, achieving an anti-interference ability of up to 95 %. This performance surpasses NADRC (which depends on nonlinear estimation) and MPC (which depends on model accuracy). Meanwhile, the steady-state time is reduced to 0.24 s through the hierarchical optimization strategy of the proposed control method. The time is 31 % to 40 % shorter than the times of MPC (0.35 s) and NADRC (0.40 s), respectively. It is also suitable for the high real-time requirements of the coal mine environment. Overall, the proposed control method outperforms MPC, NADRC, and impedance-based strategies in terms of trajectory accuracy, anti-interference ability, and energy efficiency. It is particularly suitable for the multi-constrained and complex environment of coal mines.

Table 3. Comparative experiments of advanced methods

Metric	Proposed control method	MPC	NADRC	Impedance-based
Trajectory tracking accuracy [%]	97	92	89	85
Disturbance rejection [%]	95	88	90	80
Settling time [s]	0.24	0.35	0.4	0.5
Energy efficiency [J/cycle]	54.76	68.2	72.5	60.1
Computational complexity (relative value)	4	8	6	3
Robustness parameter range [%]	±20	±15	±10	±25

4 CONCLUSION

Study aimed to develop a kinematics-based tracking control method for operational RAs in coal mining environments. An improved D-H parametric method was utilized to establish the RA linkage CS and workspace, validated through forward/inverse kinematics. A fifth-degree polynomial interpolation was implemented to generate smooth, energy-efficient joint trajectories, thereby minimizing velocity fluctuations. PSO was employed for adaptive rate matrix tuning, while Monte Carlo sampling verified robust perturbation observation gain intervals. The results showed that the proposed method enabled the RA to achieve a thrust limit exceeding 13968 N and the spiral torque limit exceeding 0.0613 Nm under four different operation modes (extension, movement, excavation, and handling). The range of RA motion fluctuation was constrained within [−0.2 $m \cdot s^{-1}$, 0.2 $m \cdot s^{-1}$]. To enhance the robustness of the system, it ensured that the velocity and position under different obstacle paths remain within the range of [−2.5 m, 2.5 m] and [−4.5 m, 1.5 m], respectively. These results confirm that the research method can effectively improve the robot's dynamic constraint capabilities against internal and external disturbances. However, certain limitations remain. The control strategy demonstrates limited adaptability to extremely high-frequency mechanical vibrations. Additionally, the vision module's trajectory replanning speed under sudden extreme lighting changes requires optimization. Future research will explore parallel computing architectures to enhance the real-time processing for handling high-frequency disturbances as well as multimodal sensor fusion mechanisms to improve the environmental perception in highly obscured or dynamically changing coal mine environments.

References

[1] Kouritem, S.A., Abouheaf, M.I., Nahas, N., Hassan, M. A multi-objective optimization design of industrial robot arms. *Alex Eng J* 61 12847-12867 (2022) **DOI:10.1016/j.aej.2022.06.052**.

[2] Durairaj, S.P. Quantitative sequential modelling approach to estimate the reliability of computer controlled pneumatically operated pick-and-place robot. *Stroj Vestn-J Mech E* 71 28-35 (2025) **DOI:10.5545/sv-jme.2024.999**.

[3] Richter, F., Lu, J., Orosco, R.K., Yip, M.C. Robotic tool tracking under partially visible kinematic chain: A unified approach. *IEEE Trans Robot* 38 1653-1670 (2021) **DOI:10.1109/tro.2021.3111441**.

[4] Karur, K., Sharma, N., Dharmatti, C., Siegel, J.E. A survey of path planning algorithms for mobile robots. *Vehicles* 3 448-468 (2021) **DOI:10.3390/vehicles3030027**.

[5] Duta, A., Popescu, I., Geonea, I.D., Cretu, S.M., Sass, L., Popa, D.L. Inverse curves-research on two quondam inversor mechanisms. *Stroj Vestn-J Mech E* 69 (2023) **DOI:10.5545/sv-jme.2022.396**.

[6] Lattanzi, L., Cristalli, C., Massa, D.,Boria, S., Lépine, P., Pellicciari, M. Geometrical calibration of a 6-axis robotic arm for high accuracy manufacturing task. *Int J Adv Manuf Technol* 111 1813-1829 (2020) **DOI:10.1007/s00170-020-06179-9**.

[7] Li, Z., Li, S., Francis, A., Luo, X. A novel calibration system for robot arm via an open dataset and a learning perspective. *IEEE T Circuits-II* 69 5169-5173 (2022) **DOI:10.1109/TCSII.2022.3199158**.

[8] Zahaf, A., Bououden, S., Chadli, M., Chemachema, M. Robust fault tolerant optimal predictive control of hybrid actuators with time-varying delay for industrial robot arm. *Asian J Control* 24 1-15 (2022) **DOI:10.1002/asjc.2444**.

[9] Jouila, A., Nouri, K. An adaptive robust nonsingular fast terminal sliding mode controller based on wavelet neural network for a 2-DOF robotic arm. *J Frankl Inst* 357 13259-13282 (2020) **DOI:10.1016/j.jfranklin.2020.04.038**.

[10] Cheng, T., Li, W., Ng, W.Y., Huang, Y., Li, J., Ng, C.S., et al. Deep learning assisted robotic magnetic anchored and guided endoscope for real-time instrument tracking. *IEEE Robot Autom Lett* 6 3979-3986 (2021) **DOI:10.1109/LRA.2021.3066834**.

[11] Lei, M., Feng, K., Ding, S., Wang, M., Dai, Z., Liu, R., et al. Breathable and waterproof electronic skin with three-dimensional architecture for pressure and strain sensing in nonoverlap mode. *ACS Nano* 16 12620-12634 (2022) **DOI:10.1021/acsnano.2c04188**.

[12] Liu, Y., Mei, Y., Cai, H., He, C.,Liu, T., Hu, G.Asymmetric input-output constraint control of a flexible variable-length rotary crane arm. *IEEE Trans Cybern* 52 10582-10591 (2021) **DOI:10.1109/TCYB.2021.3055151**.

[13] Liu, Y, Yao, X, Zhao. W. Distributed neural-based fault-tolerant control of multiple flexible manipulators with input saturations. *Automatica* 156 111202 (2023) **DOI:10.1016/j.automatica.2023.111202**.

[14] Liu, Y., Fu, Y., He, W., Hui, Q. Modeling and observer-based vibration control of a flexible spacecraft with external disturbances. *IEEE Trans Ind Electron* 66 8648-8658 (2018) **DOI:10.1109/TIE.2018.2884172**.

[15] Liu, Y., Guo, F., He, X., Hui, Q. Boundary control for an axially moving system with input restriction based on disturbance observers. *IEEE Trans Syst Man Cybern Syst* 49 2242-2253 (2018) **DOI:10.1109/TSMC.2018.2843523**.

[16] Meng, Q., Lai, X., Yan, Z., Su, C.Y., Wu, M. Motion planning and adaptive neural tracking control of an uncertain two-link rigid-flexible manipulator with vibration amplitude constraint. *IEEE Trans Neural Netw Learn Syst* 33 3814-3828 (2021) **DOI:10.1109/TNNLS.2021.3054611**.

[17] Cui, Z., Li, W., Zhang, X., Chiu, P.W., Li, Z. Accelerated dual neural network controller for visual servoing of flexible endoscopic robot with tracking error, joint motion, and RCM constraints. *IEEE Trans Ind Electron* 69 9246-9257 (2021) **DOI:10.1109/TIE.2021.3114674**.

[18] Piqué, F., Kalidindi, H.T., Fruzzetti, L., Laschi, C., Menciassi, A., Falotico, E. Controlling soft robotic arms using continual learning. *IEEE Robot Autom Lett* 7 5469-5476 (2022) **DOI:10.1109/LRA.2022.3157369**.

[19] Bodie, K., Tognon, M., Siegwart, R. Dynamic end effector tracking with an omnidirectional parallel aerial manipulator. *IEEE Robot Autom Lett* 6 8165-8172 (2021) **DOI:10.1109/LRA.2021.3101864**.

[20] Tong, L., Zhang, M., Ma, H., Wang, C., Peng, L. sEMG-based gesture recognition method for coal mine inspection manipulator using multistream CNN. *IEEE Sens* 23 11082-11090 (2023) **DOI:10.1109/JSEN.2023.3264646**.

[21] Wen, A., Bekris, K. BundleTrack: 6D pose tracking for novel objects without instance or category-level 3D models. *IEEE/RSJ Int Conf Intell Robots Syst* 8067-8074 (2021) **DOI:10.1109/IROS51168.2021.9635991**.

[22] Oliver, G., Lanillos, P., Cheng, G. An empirical study of active inference on a humanoid robot. *IEEE Trans Cogn Dev Syst* 14 462-471 (2021) **DOI:10.1109/TCDS.2021.3049907**.

[23] Qin, J., Du, J. Robust adaptive asymptotic trajectory tracking control for underactuated surface vessels subject to unknown dynamics and input saturation. *J Mar Sci Tech-Japan* 27 307-319 (2022) **DOI:10.1007/s00773-021-00835-9**.

[24] Yan, W., Liu, Y., Lan, Q., Zhang, T., Tu, H. Trajectory planning and low-chattering fixed-time nonsingular terminal sliding mode control for a dual-arm free-floating space robot. *Robotica* 40 625-645 (2022) **DOI:10.1017/S0263574721000734**.

[25] Huang, Y., Li, X., Liu, J., Qiao, Z., Chen, J., Hao, Q. Robotic-arm-assisted flexible large field-of-view optical coherence tomography. *Biomed Opt Express* 12 4596-4609 (2021) **DOI:10.1364/BOE.431318**.

[26] Li, M., Zhu, J., Liu, Q., Liao, H., Zang, K. A novel model predictive current control for fault tolerant permanent magnet vernier rim-driven motor based on improved sector selection. *J Electr Eng Technol* 20 703-712 (2025) **DOI:10.1007/s42835-024-02020-5**.

[27] Scholl, L.Y., Hampp, E.L., de Souza, K.M., Chang, T. C., Deren, M., Yenna, Z.C., et al. How does robotic-arm assisted technology influence total knee arthroplasty implant placement for surgeons in fellowship training? *J Knee Surg* 35 198-203 (2022) **DOI:10.1055/s-0040-1716983**.

[28] Li, L., Li, X., Ouyang, B., Ding, S., Yang, S., Qu, Y. Autonomous multiple instruments tracking for robot-assisted laparoscopic surgery with visual tracking space vector method. *IEEE/ASME Trans Mechatron* 27 733-743 (2021) **DOI:10.1109/TMECH.2021.3070553**.

[29] Wu, J., Liu, Z., Yu, G., Song, Y. A study on tracking error based on mechatronics model of a 5-DOF hybrid spray-painting robot. *J Mech Sci Technol* 36 4761-4773 (2022) **DOI:10.1007/s12206-022-0835-x**.

[30] Lv, N., Liu, J., Jia, Y. Dynamic modeling and control of deformable linear objects for single-arm and dual-arm robot manipulations. *IEEE Int Conf Elect Eng Big Data Algorithm* 38 2341-2353 (2022) **DOI:10.1109/EEBDA53927.2022.9744780**.

[31] Groumpos, P.P. A critical historic overview of artificial intelligence: Issues, challenges, opportunities, and threats. *Artif Intell Appl* 1 197-213 (2023) **DOI:10.47852/bonviewAIA3202689**.

[32] Hebbi, A., Mamatha, H.R. Comprehensive dataset building and recognition of isolated handwritten kannada characters using machine learning models. *Artif Intell Appl* 1 179-190 (2023) **DOI:10.47852/bonviewAIA3202624**

Acknowledgements *The research is supported by: Social contribution of Hunan Science and technology innovation plan, Engineering research and application of automatic knotting equipment for bamboo mat based on biomimetic dexterous hands (No.2020NCK2001).*

Received: 2025-02-26, revised: 2025-06-30, accepted: 2025-07-24 *as Original Scientific Paper.*

Data Availability *All data generated or analyzed during this study are included in this published article.*

Author Contribution *Li Zhou: Conceptualization, Funding acquisition, Investigation, Methodology, Visualization; Writing - original draft, Writing - review & editing; Yan Liu: Data curation, Formal analysis, Supervision, Validation. Writing - original draft, Writing - review & editing. All authors read and approved the final manuscript.*

Kinematična metoda za krmiljenje sledenja za operativno robotsko roko ob upoštevanju kompleksnih zunanjih vplivov

Povzetek *Tveganja, povezana z rudarskimi dejavnostmi v premogovnikih so izjemno visoka, zato je uporaba robotskih rok za nadomeščanje ročnega dela ključnega pomena za izboljšanje varnosti in stroškovne učinkovitosti delovnega procesa. Za obravnavo različnih okoljskih omejitev, kot so prostorske omejitve, ovire ter notranje in zunanje motnje, ta študija predlaga na kinematiki temelječo metodo krmiljenja sledenja in nadzora rudarske robotske roke. Cilj te numerične študije je predlagati metodologijo za ublažitev zunanjih vplivov na stabilnost robotskih rok ter zagotoviti visoko natančnost pri delovanju v zapletenih delovnih pogojih. Rezultati simulacij so pokazali, da predlagana metoda omogoča, da robotska roka doseže operativne vršne potisne sile, večje od 13.968 N, ter vršne vijačne momente, večje od 0,0613 Nm. Sistem je dosegel stacionarno stanje v povprečju v 0,24 s, pri čemer se je napaka zmanjšala za 2,3 %. V primerjavi z drugimi metodami je sledilnik motenj zmanjšal povprečno napako za 2 %, krmilnik s povratno zanko pa zmanjšal zakasnitev napovedi za 5 %. Predlagana metoda bistveno izboljšuje natančnost in stabilnost pozicioniranja robotskih rok pri rudarskih delih v premogovnikih ter predstavlja obetaven pristop za praktično uporabo.*

Ključne besede *rudarske operacije v premogovnikih, robotska roka, dinamika, kompleksni zunanji vplivi, krmiljenje sledenja*

An Optimal Design Method of Hydrostatic Turntable Based on FPSO Algorithm

Yongsheng Zhao✉ – Jiaqing Luo – Ying Li – Tao Zhang – Honglie Ma
Institute of Advanced Manufacturing and Intelligent Technology, Beijing University of Technology, China
✉ yszhao@bjut.edu.cn

Abstract *The load capacity of hydrostatic turntables is predominantly governed by the design of oil pads. Optimizing oil pad parameters can substantially enhance turntable performance while reducing power consumption. This study introduces a fuzzy particle swarm optimization (FPSO) algorithm that incorporates compression factors into the particle swarm optimization (PSO) framework to optimize the parameters of oil pads. Reduce its power consumption by about 40 %, while the error between experimental and theoretical values is only 8 %. Compared with traditional PSO algorithms, FPSO converges more reliably in multiparametric environments.*

Keywords *hydrostatic turntable, finite difference method, Reynolds equation, fuzzy particle swarm optimization algorithm, performance optimization*

Highlights

- *Introduced FPSO algorithm with compression factors for oil pad optimization.*
- *FPSO cut hydrostatic turntable power use by ~40%, boosting energy efficiency.*
- *FPSO showed strong convergence and 8% error, outperforming traditional PSO.*

1 INTRODUCTION

In heavy computer numerical control (CNC) machine tools, the hydrostatic turntable is a critical component that not only supports the machine tool but also provides high-precision movement. With advancements in hydrostatic bearing technology, its analysis and optimization have become increasingly complex, requiring extensive numerical calculations. Additionally, the size deviation of the oil pad significantly affects the oil film pressure distribution. Since millimeter-level precision control is essential for maintaining the high-precision rotation of the turntable, an efficient optimization algorithm is needed to optimize the load-carrying capacity of the circular oil pad. The particle swarm optimization (PSO) algorithm with a compressibility factor is an effective computational method, improving both the precision and convergence speed of the PSO algorithm.

The Reynolds equation is commonly used to evaluate hydrostatic turntables. It is a two-dimensional, second-order partial differential equation that incorporates parameters such as pressure, film thickness, and density. Several research teams have employed the Reynolds equation to analyze hydrostatic bearings and address engineering problems [1,2]. Wang et al. [3] numerically modified the classical Reynolds equation by considering the transient film thickness changes and surface deformation effects in the elastohydrodynamic lubrication (EHL) state. On this basis, Singh et al. [4] applied the improved Reynolds equation to analyze different oil pad configurations under hydrodynamic lubrication (HL) conditions and proved its adaptability under different lubrication systems. Gustafsson et al. [5] improved the Reynolds equation by incorporating the warm viscosity effect into the EHL model. Instead, Yang et al. [6] extended the equation with a non-Newtonian rheological model, which is commonly applied to the study of HL in complex fluids under steady-state conditions. Masjedi and Khonsari [7] proposed a numerical solution to the Reynolds equation by implementing the continuous successive over-relaxation (SOR) technique, which is particularly effective for solving transient EHL problems involving coupling pressure-deformation-film thickness interactions. El Khlifi et al. [8] extended the modeling framework by incorporating non-Newtonian fluid rheology and improved energy equations, a typical HL approach for solving steady-state viscous flows with complex fluid behavior. Li and Chen [9] derived an approximate expression for bearing surface roughness and obtained results by solving the Reynolds equation. Liu et al. [10] presented Reynolds expressions for bearings of various shapes, while Khakse et al. [11] formulated a Reynolds equation in spherical coordinates.

The PSO algorithm was initially proposed by Kennedy and Eberhart [12]. It is inspired by the predatory behavior of birds and fish, simulating their flight and foraging patterns to achieve optimal solutions through collective intelligence. This swarm intelligence-based optimization technique is simple to implement and has been applied to various fields, including bearing optimization. To ensure the convergence of the PSO algorithm, a compression factor is required [13]. Several studies [14-16] have attempted to improve the precision and convergence speed of the PSO algorithm by modifying parameter values. Niu et al. [17] developed a method for hyperstatic analysis and motion error prediction, validating its effectiveness but not optimizing it using an improved PSO algorithm. Chen and Li [18] introduced a novel multi-sensor signal analysis method for centrifugal pump fault diagnosis using an improved PSO algorithm, significantly enhancing structural optimization complexity and reducing computation time. Zhou et al. [19] proposed an improved PSO algorithm to reduce computational complexity, while Paikray et al. [20] applied an enhanced PSO algorithm to generate optimal, collision-free trajectories for robots in cluttered environments. Zhang et al. [21] improved the PSO algorithm by introducing dynamic inertia weights and gradient information, improving bearing fault diagnosis accuracy. Sana et al. [22] integrated an improved PSO algorithm with blockchain technology to enhance efficiency and security. Liu et al. [23] utilized an improved PSO algorithm to iteratively optimize the parameters of the gcForest model, achieving optimal diagnostic accuracy. Cheng et al. [24] applied different types of hydrostatic bearings to the PSO algorithm. Chang and Jeng [25] employed the

 DOI: 10.5545/sv-jme.2025.1366

PSO algorithm to design a double shim hydrostatic bearing. Srisha Rao and Jagadeesh [26] used vector-based evaluation to enhance the PSO algorithm convergence. Tang et al. [27] applied the PSO algorithm to workshop scheduling optimization, and Luo et al. [28] proposed a new group update method to improve species-based algorithms. Finally, Liu et al. [29] reviewed various optimization methods, highlighting the widespread application of the PSO algorithm across multiple domains.

In order to improve the load-bearing performance of the hydrostatic turntable and further reduce power consumption. This study modifies the Reynolds equation based on the working conditions of the hydrostatic turntable, and then uses the finite difference method (FDM) to solve the pressure distribution and oil flow parameters. The fuzzy particle swarm optimization (FPSO) algorithm is proposed for optimizing the key parameters of the turntable and further improving its load-bearing capacity. Compared with the PSO algorithm, power consumption is reduced by about 40 %, and the experimental and theoretical values have an error of only 8 %. The experimental results show that using the FPSO algorithm can obtain optimal solutions for various parameters of the turntable and minimize power consumption, providing an important reference for optimizing and evaluating the load-bearing performance of the hydrostatic turntable.

2 METHODS AND MATERIALS

2.1 Model of Hydrostatic Turntable and Oil Pad

As a key component of CNC machine tools, the hydrostatic turntable, plays an important role in the field of precision machining [30]. Its working principle is based on the hydrostatic pressure bearing theory, with a pressurized oil film as the core working medium. During operation, the external oil pump transfers the high-pressure oil to each oil chamber of the rotary table through the precision oil circuit, forming an oil film with bearing capacity between the rotary body and the base of the hydrostatic turntable. This oil film acts as a near-frictionless surface, supporting the weight of the rotary body and enabling smooth rotation [6].

The oil pad on the base is the core component that determines the bearing capacity of the hydrostatic turntable. After the high-pressure oil enters the oil pad, it is evenly distributed on the surface of the oil pad through the precise control of the throttling device to form a stable oil film with a certain stiffness. Several oil pads are strategically arranged on the base to carry the rotary body together. The classic hydrostatic turntable model is shown in Fig. 1, showing the main components of the turntable, including the base support system, the rotating execution unit, the hydrostatic bearing unit, the hydrostatic control system, and the auxiliary function module.

The oil pad consists of a circular stepped pad with concentric oil pockets, incorporating oil pockets and oil seals. The classic circular oil pad structure is shown in Fig. 1, where R_0 is the oil pad radius, R_1 is the oil pocket radius, and H_0 is the oil film thickness. Typical values of the outer diameter of the general circular oil pad R_0 are between 50 mm and 300 mm [31], while the inner diameter R_1 is usually kept between 20 mm and 150 mm [31]. As a key parameter, oil film thickness H_0 has a significant impact on the performance of the hydrostatic turntable, and its typical range is from 10 μm to 50 μm [32].

As the oil film thickness tends to zero, the bearing capacity becomes nearly infinite, increasing the likelihood of oil film collapse and compromising the machine tool's safety. Thus, it is necessary to regulate oil film thickness within a safe range. The working conditions of the hydrostatic turntable are as follows [33]:

$$\begin{cases} H \geq H_0 \\ \sum_{i=1}^{N} W_i = mg \end{cases}. \tag{1}$$

2.2 Theoretical Model

In hydrostatic systems, the pressure distribution in the oil pad is described by the Reynolds equation. Before solving the Reynolds equation, the following dimensionless parameters must be defined:

$$\bar{p} = \frac{p}{p_0},\ \bar{p}_0 = 1,\ \bar{r} = \frac{r}{R_0},\ \bar{R}_0 = 1,\ \bar{z} = \frac{z}{H},\ \bar{h} = \frac{h}{H},\ \bar{H} = 1,$$
$$\bar{U}_r = \frac{U_r}{\frac{H_0^2 P_0}{R_0 \eta}},\quad \bar{U}_\theta = \frac{U_\theta}{\frac{H_0^2 P_0}{R_0 \eta}},\quad \bar{W} = \frac{W}{R_0^2 P_0},\quad \bar{q} = \frac{Q}{\frac{H_0^3 P_0}{\eta}}, \tag{2}$$

where p is the oil film pressure, P_0 is the oil pocket pressure, r is the radial coordinate, h is the oil film thickness, U_r is the radial velocity, U_θ is the circumferential velocity, W is the bearing performance, Q is the volume flow of the oil pad, η is the viscosity. Moreover $\bar{p}$ is the dimensionless pressure, $\bar{h}$ dimensionless oil film thickness, $\bar{U}_r$ dimensionless radial velocity, $\bar{U}_\theta$ dimensionless circumferential velocity, $\bar{W}$ dimensionless bearing performance, $\bar{q}$ dimensionless flow, z coordinate in the film thickness direction, and p_0 pocket pressure (reference pressure).

Circular oil pads are suitable for Reynolds equations in cylindrical coordinate form. The fan element is used to analyze the force of the

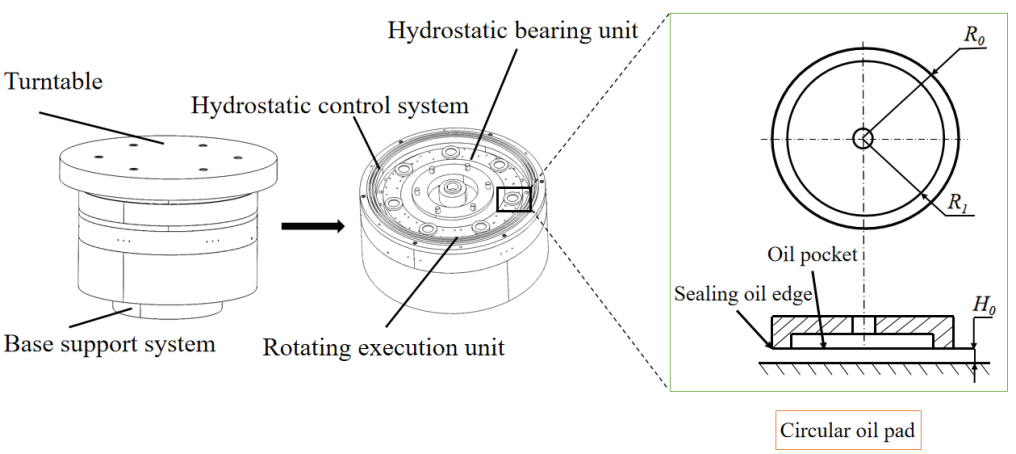

Fig. 1 Model of the hydrostatic turntable and circular oil pad

element, and the inertial force due to the centripetal acceleration of the element is introduced. The fan element forces used to analyze the circular oil pad are shown on Fig. 2. In polar coordinates, the Reynolds equation of the circular oil pad is [34]:

$$\frac{\partial}{\partial \bar{r}}\left(rh^3\frac{\partial \bar{p}}{\bar{r}}\right)+\frac{\partial}{\partial \bar{\vartheta}}\left(h^3\frac{\partial \bar{p}}{\bar{r}\vartheta\bar{\vartheta}}\right)=0. \tag{3}$$

A common way to solve this partial differential equation is through FDM, which discretizes the equations into finite algebraic equations and iteratively solves them, as shown in Fig. 3. The Reynolds equation and its discretized form are expressed as follows [35]:

$$\begin{bmatrix} A1_{i,j} & A2_{i,j} & A3_{i,j} & A4_{i,j} & A5_{i,j}\end{bmatrix}\begin{bmatrix}\bar{p}_{i+1,j}\\ \bar{p}_{i-1,j}\\ \bar{p}_{i,j}\\ \bar{p}_{i,j-1}\\ \bar{p}_{i,j+1}\end{bmatrix}=0, \tag{4}$$

$$\begin{cases} A1_{i,j}=\dfrac{\bar{r}_i\bar{h}_{i,j}^3}{\bar{r}_{step}^2}\\ A2_{i,j}=\dfrac{\bar{r}_{i-1}\bar{h}_{i-1,j}^3}{\bar{r}_{step}^2}\\ A3_{i,j}=-\left(\dfrac{\bar{r}_i\bar{h}_{i,j}^3}{\bar{r}_{step}^2}+\dfrac{\bar{r}_{i-1}\bar{h}_{i-1,j}^3}{\bar{r}_{step}^2}+\dfrac{\bar{h}_{i,j-1}^3}{\bar{r}_i\,\bar{\theta}_{step}^2}+\dfrac{\bar{h}_{i,j}^3}{\bar{r}_i\,\bar{\theta}_{step}^2}\right)\\ A4_{i,j}=\dfrac{\bar{h}_{i,j-1}^3}{\bar{r}_i\,\bar{\theta}_{step}^2}\\ A5_{i,j}=\dfrac{\bar{h}_{i,j}^3}{\bar{r}_i\,\theta_{step}^2}\end{cases}, \tag{5}$$

where [$A1$, $A2$,..., $A5$] is the coefficient vector and the pressure is assumed to be distributed across x_{pieces} nodes in the x direction and y_{pieces} nodes in the y direction. The value of the index i is an integer in $[1,x_{pieces}]$, and the value of the index j is an integer in $[1, y_{pieces}]$. Therefore, Eq. (4) forms an algebraic system of equations of dimension $x_{pieces}{\times}y_{pieces}$, and its solution provides the numerical solution of the pressure distribution. Here, i and j represent the r and θ coordinates. $\bar{r}_{step}$ is the step size of the r coordinate, $\bar{\theta}_{step}$ is θ steps of coordinates. The boundary conditions for the pressure distribution are as follows: the pressure within the inner oil pocket is set to 1, while the pressure at the outer oil seal is 0 [36]:

$$\bar{p}_{i,j}=\begin{cases}1, & \bar{r}_i<\bar{R}_1\\ 0, & \bar{r}_i=1\end{cases}. \tag{6}$$

The bearing capacity of the oil pad is determined using [25]:

$$\begin{cases}\bar{w}=\int\bar{p}r d\bar{r}d\bar{\theta}\\ \bar{q}=\int\dfrac{\bar{z}^2-\bar{z}}{2\eta}\dfrac{\partial\bar{p}}{\partial\bar{r}}d\bar{z}, \quad \text{where} \quad \bar{r}_i=1\end{cases}. \tag{7}$$

The parameters $\bar{w}$ and $\bar{q}$ are important indicators for evaluating the bearing capacity of the hydrostatic turntable. These parameters vary with changes in $\bar{R}_1$. Assuming that the delivery weight is constant, the pump power is expressed as follows [27]:

$$\begin{cases}P_0=\dfrac{mg}{N\bar{w}\pi R_0^2}\\ Q=\bar{q}\dfrac{H_0^3P_0}{\eta}\\ P_s=NP_0Q\end{cases}, \tag{8}$$

where P_s is the power consumption. During the optimization process, losses due to the electromechanical system's efficiency and pressure variations are neglected.

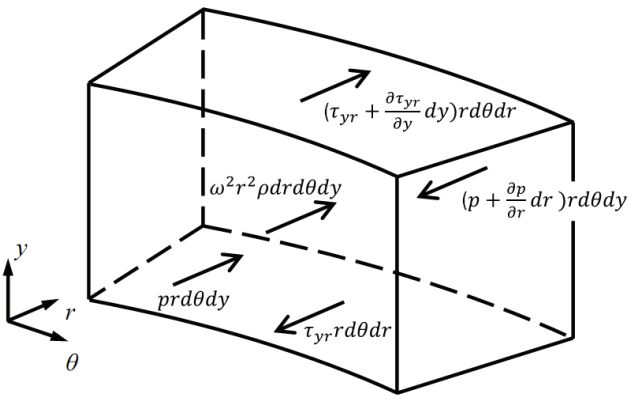

Fig. 2. Circular microelement forces in cylindrical coordinates

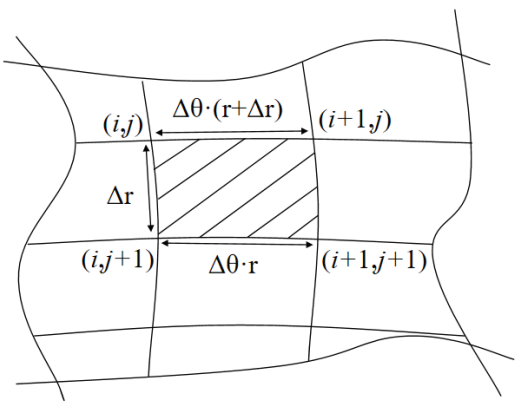

Fig. 3. Discretization of pressure

2.3 FPSO Algorithm

The PSO algorithm is a global search optimization method known for its simplicity and fast convergence. Due to its leapfrog nature, it efficiently locates the global optimum. This algorithm is particularly useful for optimizing problems involving multiple design variables and minimal parameters, where the number of particles is defined by N_p. Here, w is inertia weight, c_1 and c_2 are learning factors, X_i is particle position, V_i is search vector, P_i is individual optimal position, G_{best} is population optimal position, r_1 and r_2 are random numbers in the interval [0,1]. In Equation (9b), the first item is a memory term, representing the size and direction of the speed in the last iteration, the second item is a self-cognition term, and is referred to as the "self-cognition item" of particles. The third item is a group cognition term, indicating that the actions of particles are determined by their own experience and the best experience of their peers [18].

$$X_i^{n+1}=X_i^n+V_i^{n+1}, \tag{9a}$$

$$V_i^{n+1}=wV_i^n+c_1r_1\left(P_i^n-X_i^n\right)+c_2r_2\left(G_{best}^n-X_i^n\right). \tag{9b}$$

In cases with multiple local optima, the PSO algorithm may struggle to identify the global optimum. For instance, in Griewank function optimization, after initializing particles using the PSO algorithm, particles are easily attracted by local optima during iterations. This results in clustering around a local solution, which makes it difficult to find the optimal global solution due to reduced

speed and limited information exchange. To address this limitation, a compression factor, also known as a constraint factor, can be introduced to control system convergence. This approach enables efficient exploration of different regions and improves solution quality. By increasing the compression factor, particle flight speed can be effectively controlled, thereby balancing local search capability and global convergence. This further enhances the global search capability and avoids the problem of premature convergence of the hydrostatic turntable in multi-objective parameter optimization. It has been verified by experiments that the best convergence accuracy and speed can be achieved when c_1 is 0.4 and c_2 is 0.9 [28]. This ensures the algorithm's accuracy and convergence speed. The modified equations incorporating the compression factor are given as follows [13]:

$$V_i^{n+1} = K \times \left(V_i^n + c_1 r_1 \left(P_i^n - X_i^n \right) + c_2 r_2 \left(G_{best}^n - X_i^n \right) \right), \tag{10a}$$

$$K = \left(\frac{(2)}{\left| 2 - \varnothing - \sqrt{\varnothing^2 - 4\varnothing} \right|} \right), \quad \varnothing = c_1 + c_2 \text{ and } \varnothing > 4. \tag{10b}$$

Each individual in the PSO algorithm represents a value of R_1 so that $R_1 = X_n \cdot R_0$. The optimization objective is to minimize bearing losses. The termination condition for the optimization is defined as follows [25]:

$$\begin{cases} \left| x_n^{(k)} - x_n^{(k-1)} \right| \le tol_{PSO} \\ \max\left(x_n^{(k)} \right) - \min\left(x_n^{(k)} \right) \le tol_{PSO} \end{cases}. \tag{11}$$

3 RESULTS AND DISCUSSION

3.1 Theoretical Calculation

The algorithm of this research is shown in Fig. 4, which mainly includes three parts: first, using FDM to solve the Reynolds equation, and then evaluating the support force. Finally, the improved PSO algorithm with compression factor is used to solve the minimum power consumption problem of the oil pad.

The bearing capacity of the oil pad is analyzed using dimensionless bearing capacity and dimensionless flow parameters. The size of the oil pad influences both factors. Figure 5 presents experimental results demonstrating that the bearing capacity of the oil pad increases with the dimensionless size.

As shown in Fig. 6, increasing the dimensionless radius of the circular oil pad leads to an increase in both dimensionless bearing capacity and dimensionless flow rate. The dimensionless bearing capacity exhibits a linear increase with radius, while the dimensionless flow rate increases at a higher rate as the radius grows. This is because the increase in the dimensionless radius will expand the oil film pressure integral region, so that the bearing area is proportional to the square of the radius, thus significantly improving the hydrostatic bearing capacity. In addition, driven by the pressure difference, the effective path length of the oil flow along the radial direction is linearly related to the dimensionless radius, resulting in enhanced fluid energy transfer.

3.2 Experimental Verification

To verify the theoretical calculation, a 32-channel dynamic signal acquisition module is configured with an LMS modal test instrument. The installation gap was eliminated, and the repeatability of boundary conditions was ensured by the preloading method. An acceleration sensor was arranged on the turntable to monitor the vibration response, and the pressure distribution data was collected synchronously by the strain gauge attached to the surface of the oil pad. The experiments were carried out on the hydrostatic turntable of General Technology Group Tianjin First Machine Tool Corporation, China, as shown in Figs. 7a and b. The parameters of the hydrostatic turntable are presented in Table 1, while the size parameters of the tested circular oil pads are listed in Table 2.

Table 1. Relevant parameters of the hydrostatic turntable

Parameter	Value	Parameter	Value	Parameter	Value
R_0	0.075 m	n	20	tol_{FDM}	1×10^{-7}
m	25000 kg	η	0.08 Pa·s	tol_{PSO}	6

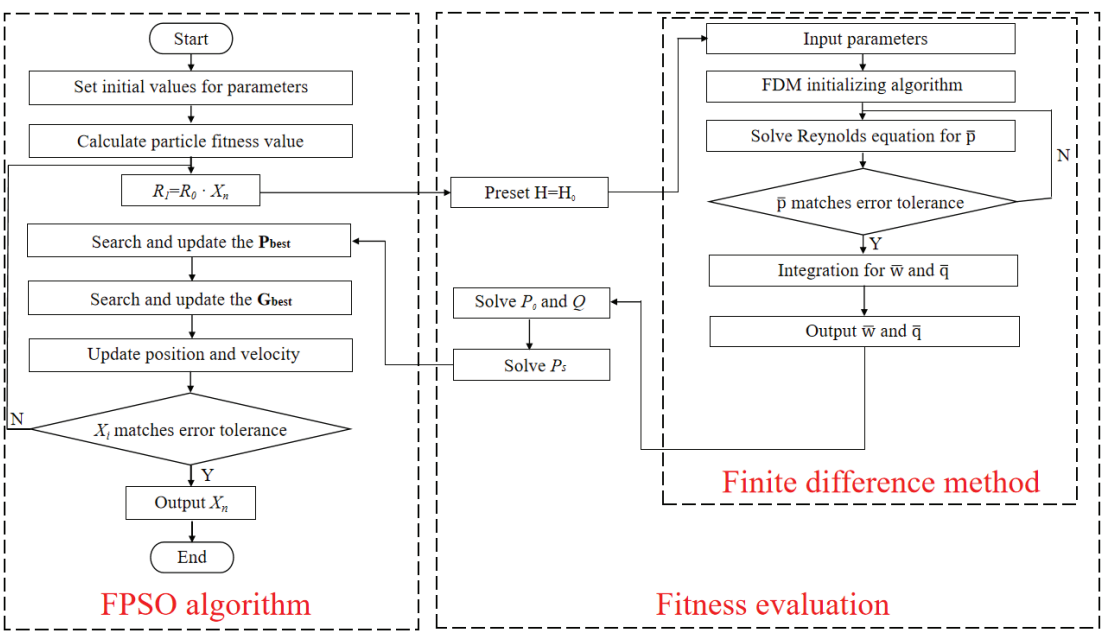

Fig. 4. Flowchart of the proposed algorithm

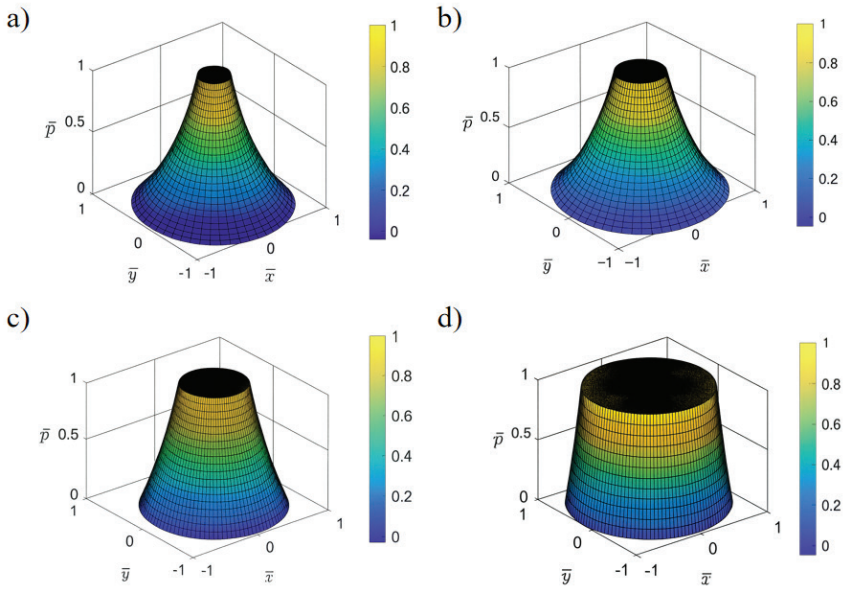

Fig. 5. Relationship between dimensionless pressure distribution and dimensionless oil pad radius: a) $\bar{R}_1$ = 0.2, b) $\bar{R}_1$ = 0.4, c) $\bar{R}_1$ = 0.6, and d) $\bar{R}_1$ = 0.8

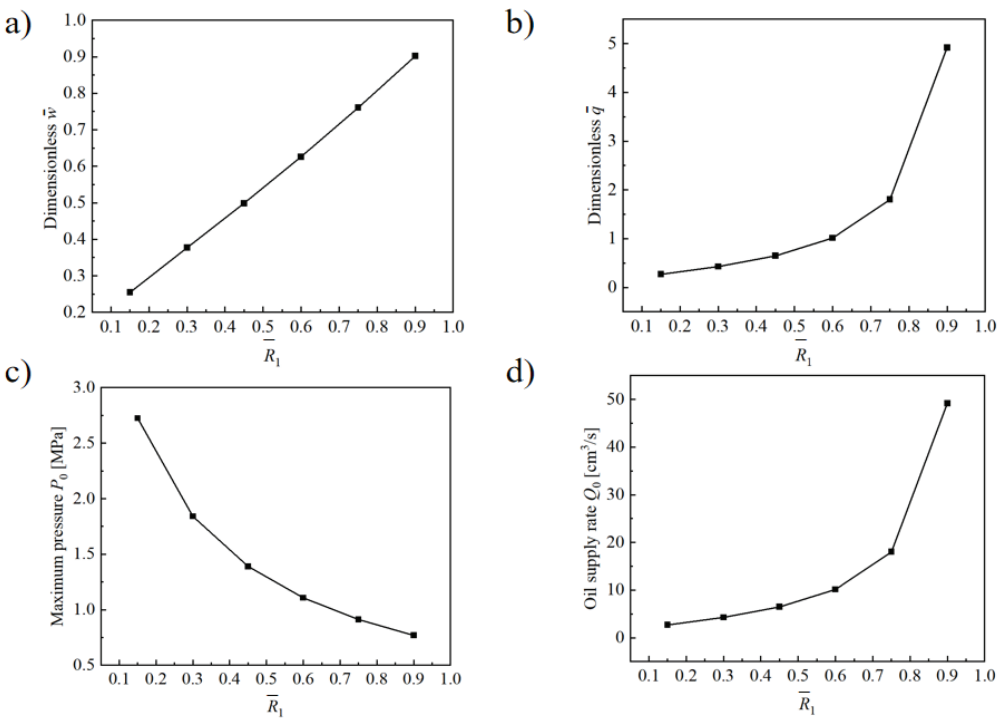

Fig. 6. Relationship between circular oil pad performance and pad size; a) dimensionless $\bar{w}$, b) dimensionless $\bar{q}$, c) maximum pressure P_0, and d) oil supply rate Q

Five circular oil pads of varying sizes were selected for testing. The test results are shown in Figs. 7c and d. Compared to theoretical calculations, the experimental values were lower, with a minimum error of approximately 8 %. The results indicate a certain deviation between theoretical and experimental values. The reason for the error is that the theoretical model usually ignores the nonlinear constitutive relationship of oil, the coupling effect of multiple physical fields, and the geometric deviation introduced by the manufacturing process, which leads to systematic error in the prediction of fluid mechanics behavior. In addition, experimental factors such as oil contamination and assembly errors further expand the error range. However, the trends of dimensionless bearing capacity and flow rate with respect to oil pad size remain consistent, confirming the feasibility of the theoretical calculations.

Table 2. Dimensional parameters of circular oil pads

	R_0 [m]	R_1 [m]	$\bar{R}$
Pad 1	0.033	0.01	0.3030303
Pad 2	0.033	0.015	0.4545454
Pad 3	0.033	0.02	0.6060606
Pad 4	0.033	0.025	0.7575758
Pad 5	0.033	0.028	0.8484848

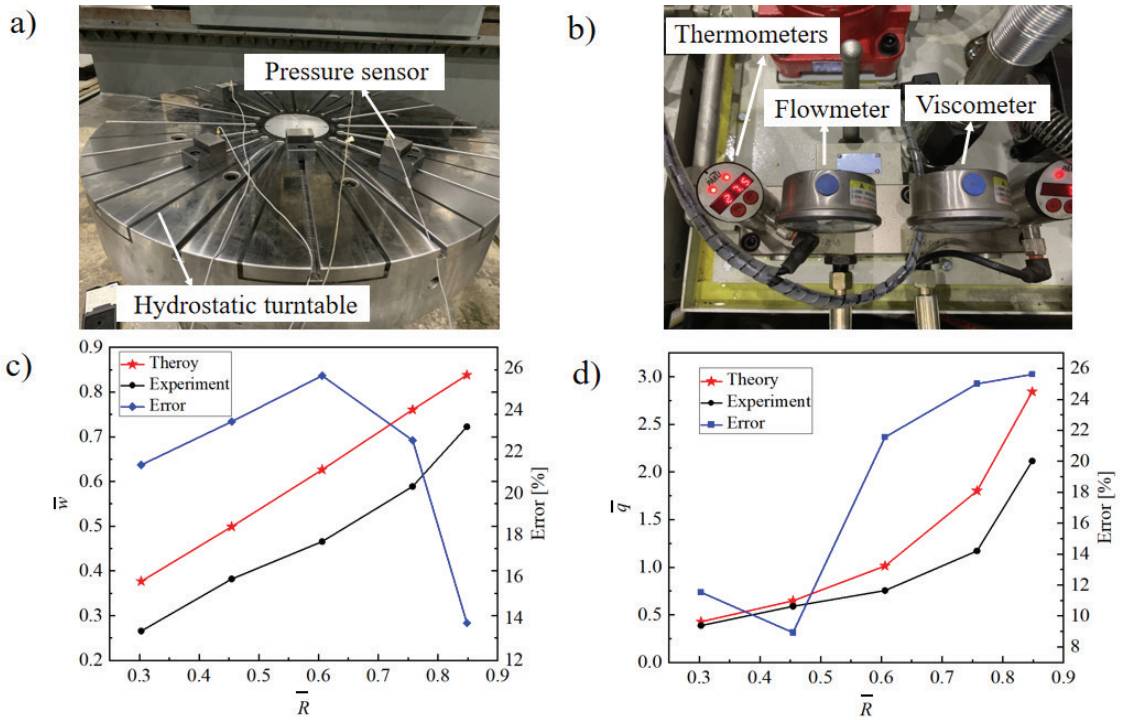

Fig. 7. Hydrostatic turntable testing and comparison of theoretical and experimental results; a) physical diagram of the hydrostatic turntable, b) data acquisition system, c) dimensionless bearing capacity, and d) dimensionless flow

3.3 Optimization of Various Parameters Based on FPSO Algorithm

The initial position and velocity of particle X_n within the defined domain were randomly assigned. The radius of the oil pad was assumed to be $R_1=X_n \cdot R_0$, linking its size to the particle positions. As the position of the particle in the search space changes, the X_n also changes, resulting in a corresponding change in the oil pad radius R_1. The film thickness was assumed to be H_0, and support performance was determined using the finite difference method to minimize power loss. The FPSO algorithm identified the global optimal solution by iteratively searching for the best fitness value, determining the optimal location, and power consumption. The effect of dynamic viscosity η, oil film thickness H_0, and the number of oil pads on pump power consumption was investigated. When the particle swarm size was set to five, convergence was achieved in seven cycles. The impact of η on pump power consumption is shown in Fig. 8, where η was set to 0.06, 0.08, and 0.1. The results indicate a negative correlation between η and pump power consumption. Variations in X_η and P_s remained minimal, suggesting that η has a limited effect on pump power consumption, increasing from 0.06 to 0.1 and reducing power consumption by only 20.6 W, with the optimal power consumption being 30.5 W when the P_s position is 0.549, and the optimal η is 0.1. The influence of oil film thickness H_0 on pump power was then examined. Under ideal conditions, the minimum oil film thickness can reach 5×10^{-5} m. To accommodate practical conditions, the minimum thickness was evaluated starting from 10×10^{-5}, as shown in Fig. 9. The results indicate a positive correlation between H_0 and pump power consumption. While H_0 had minimal influence on X_n, it significantly affected P_s. When the particle position reaches 0.565, the minimum power consumption is 407.6 W, and the optimal oil film thickness is 1×10^{-4} m. This shows that thicker films require higher support power. Finally, the effect of the number of oil pads on pump power was analyzed, as shown in Fig. 10. The number of oil pads was set to 10, 15, and 20, while other parameters remained constant.

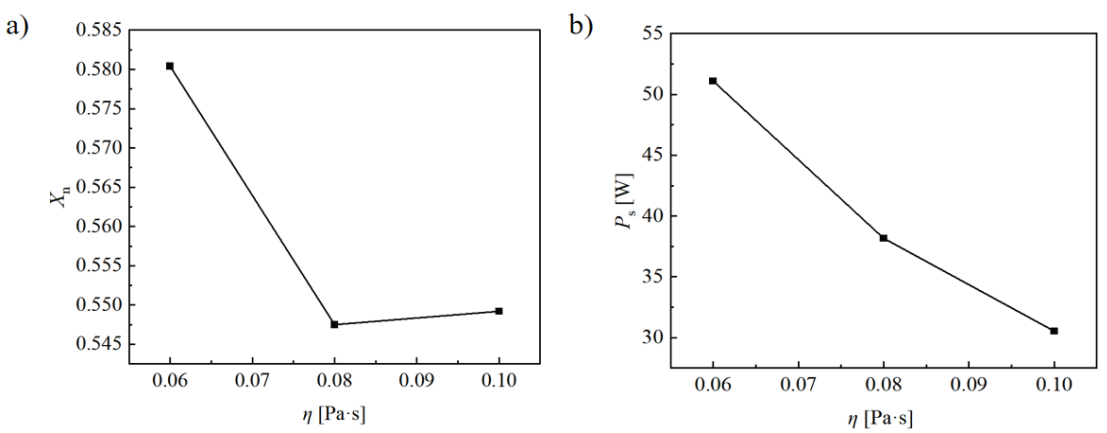

Fig. 8. The influence of different η on a) position of the particles, and b) power consumption

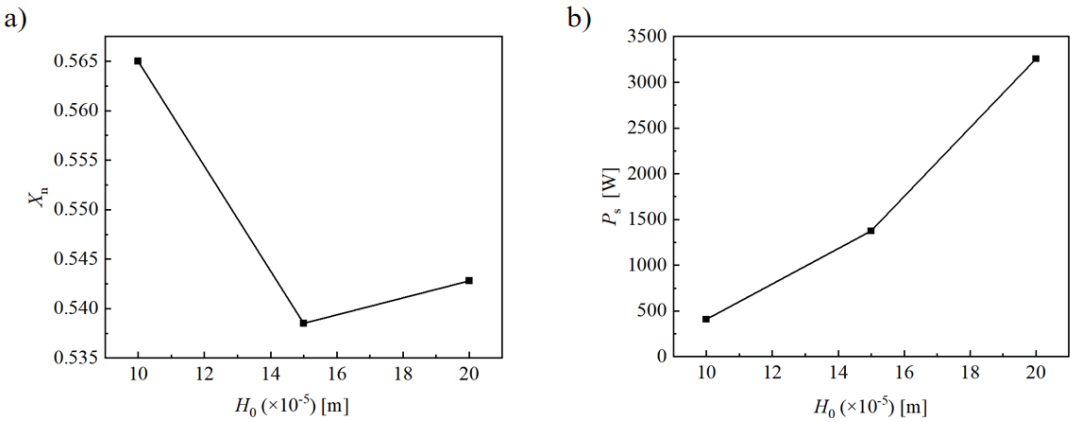

Fig. 9. The influence of different H_0 on; a) position of the particles in each iteration, and b) power consumption

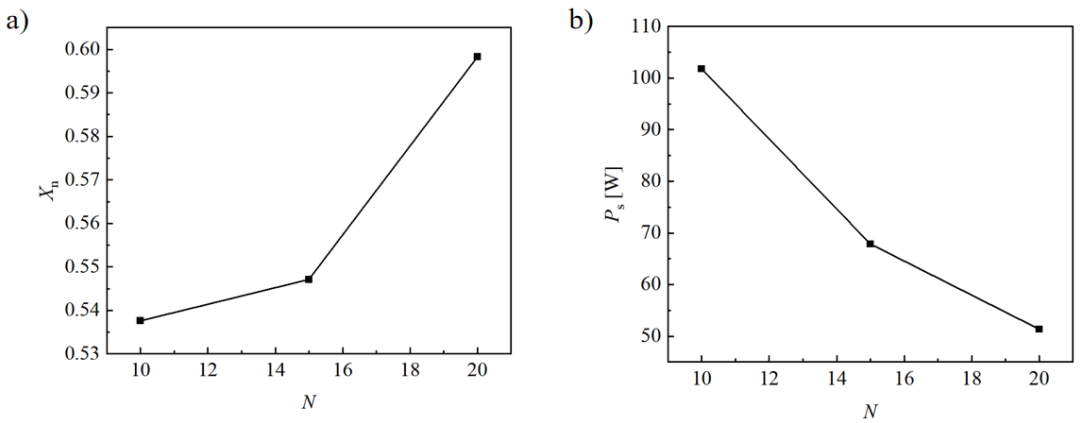

Fig. 10. The influence of different N on: a) position of the particles, and b) power consumption

The results indicate an inverse relationship between the number of oil pads and pump power consumption. When the particle position reaches 0.598, the optimal number of oil pads is 20, and the minimum power consumption is 51.3 W. Increasing the number of oil pads reduced overall power consumption. However, the number of oil pads had a relatively minor effect on power consumption compared to other factors. Overall, film thickness H_0 was identified as the primary factor affecting pump power consumption. Based on the experimental results and the operational constraints of the hydrostatic turntable, the optimal parameters were determined as η=0.1, H_0=1×10^{-4} m, and N=20. Under these conditions, the optimal power consumption of the turntable was P_s=244.3 W. By reducing the power consumption of the support, the hydraulic thermal load and the thermal drift caused by the increase in oil temperature and rotation axis are directly reduced, which is beneficial for the geometric accuracy and surface smoothness in heavy-duty CNC machining. Simultaneously, precise control of film thickness can achieve maximum energy-saving effect, while an appropriate number of oil pads can maintain load-bearing capacity and overturning stiffness. It also reduces operating costs, pump wear, and cooler load, and can reduce auxiliary cooling capacity.

4 CONCLUSIONS

To solve the optimization problem of load power consumption in a hydrostatic turntable, this study solved the Reynolds equation using the FDM method to analyze the bearing capacity of the hydrostatic turntable. The relationship between turntable parameters and power consumption was determined numerically. Based on these findings, an efficient optimization method for hydrostatic turntable design is proposed to solve the problem of premature convergence of traditional PSO in multivariable nonlinear optimization. The conclusions are as follows:

1. A FPSO algorithm has been proposed to address the shortcomings of single objective tuning and premature convergence in the design of multivariable parameters for hydrostatic turntables using the PSO algorithm. It improves the load-bearing performance while reducing power consumption.
2. Through FPSO algorithm optimization, the optimal parameters for the hydrostatic turntable can be obtained as follows: η = 0.1, H_0=1×10 $^{-4}$ m, N=20. The influence of various parameters on the bearing performance of the turntable has been clarified: H_0>N>η. The maximum energy-saving effect can be achieved by controlling the precise film thickness, while the appropriate number of pads can maintain load capacity and overturning stiffness.
3. The support power consumption of the pump has been reduced by about 40 %, and the theoretical calculation and experimental error is only 8 %. Further improving its load-bearing performance reduces thermal drift and operating costs in the turntable.

References

[4] Qiu, M., Bailey, B.N., Stoll, R., Raeymaekers, B. The accuracy of the compressible Reynolds equation for predicting the local pressure in gas-lubricated textured parallel slider bearings. *Tribol Int* 72 (2014) 83-89 **DOI:10.1016/j.triboint.2013.12.008**.

[5] de la Guerra Ochoa, E., Echávarri Otero, J., Sánches López, A., Chacón Tanarro, E. Film thickness predictions for line contact using a new Reynolds-Carreau equation. *Tribol Int* 82 133-141 (2015) **DOI:10.1016/j.triboint.2014.10.003**.

[6] Wang, N., Cha, K.-C., Huang, H.-C. Fast convergence of iterative computation for incompressible-fluid Reynolds equation. *J Tribol-T ASME* 134 024504 (2012) **DOI:10.1115/1.4006360**.

[7] Singh, U.P., Gupta, R.S., Kapur, V.K. On the steady performance of annular hydrostatic thrust bearing: Rabinowitsch fluid model. *J Tribol-T ASME* 134 044502 (2012) **DOI:10.1115/1.4007350**.

[8] Gustafsson, T., Rajagopal, K.R., Stenberg, R., Videman, J. Nonlinear Reynolds equation for hydrodynamic lubrication. *Appl Math Model* 39 5299-5309 (2015) **DOI:10.1016/j.apm.2015.03.028**.

[9] Yang, Q, Huang, P, Fang, Y A novel Reynolds equation of non-Newtonian fluid for lubrication simulation. *Tribol Int* 94 458-463 (2016) **DOI:10.1016/j.triboint.2015.10.011**.

[10] Masjedi, M., Khonsari, M.M. On the effect of surface roughness in point-contact EHL: Formulas for film thickness and asperity load. *Tribol Int* 82 228-244 (2015) **DOI:10.1016/j.triboint.2014.09.010**.

[11] El Khlifi, M., Souchet, D., Hajjam, M., Bouyahia, F. Numerical modeling of non-Newtonian fluids in slider bearings and channel thermohydrodynamic flow. *J Tribol-T ASME* 129 695-699 (2007) **DOI:10.1115/1.2736732**.

[12] Li, J., Chen, H. Evaluation on applicability of Reynolds equation for squared transverse roughness compared to CFD. *J Tribol-T ASME* 129 963-967 (2007) **DOI:10.1115/1.2768619**.

[13] Liu, Z., Wang, Y., Cai, L., Cheng, Q., Zhang, H. Design and manufacturing model of customized hydrostatic bearing system based on cloud and big data technology. *Int J Adv Manuf Tech* 84 261-273 (2016) **DOI:10.1007/s00170-015-8066-2**.

[14] Khakse, P., Phalle, V., Mantha, S. Performance analysis of a nonrecessed hybrid conical journal bearing compensated with capillary restrictors. *J Tribol-T ASME* 138 011703 (2016) **DOI:10.1115/1.4030808**.

[15] Kennedy, J., Eberhart, R. Particle swarm optimization. *IEEE International Conference on Neural Networks* 4 1942-1948 (1995) **DOI:10.1109/ICNN.1995.488968**.

[16] Eberhart, R., Shi, Y. Comparing inertia weights and constriction factors in particle swarm optimization. *IEEE World Congress on Evolutionary Computation* 1 84-88 (2000) **DOI:10.1109/CEC.2000.870279**.

[17] Schutte, J.F., Koh, B., Reinbolt, J.A., Haftka, R.T., George, A.D., Fregly, B.J. Evaluation of a particle swarm algorithm for biomechanical optimization. *ASME J Biomech Eng* 127 465-474 (2005) **DOI:10.1115/1.1894388**.

[18] Khajehzadeh, M., El-Shafie, A., Raihan, T. Modified particle swarm optimization for probabilistic slope stability analysis. *Int J Phys Sci* 5 2248-2258 (2010).

[19] Yan, Z., Deng, C., Zhou, J., Chi, D. A novel two subpopulation particle swarm optimization. *IEEE World Congress on Intelligent Control and Automation* 4113-4117 (2012) **DOI:10.1109/WCICA.2012.6359164**.

[20] Niu, P., Cheng, Q., Zhang, T., Yang, C., Zhang, Z., Liu, Z. Hyperstatic mechanics analysis of guideway assembly and motion errors prediction method under thread friction coefficient uncertainties. *Tribol Int* 108275 (2023) **DOI:10.1016/j.triboint.2023.108275**.

[21] Chen, H., Li, S. Multi-sensor fusion by CWT-PARAFAC-IPSO-SVM for intelligent mechanical fault diagnosis. *Sensors* 3647 (2022) **DOI:10.3390/s22103647**.

[22] Zhou, J., Wu, S.-S., Liu, T., Wu, X. Application of IPSO-MCKD-IVMD-CAF in the compound fault diagnosis of rolling bearing. *Meas Sci Technol* 34 035113 (2023) **DOI:10.1088/1361-6501/aca349**.

[23] Paikray, H.K., Das, P.K, Panda, S. Optimal multi-robot path planning using particle swarm optimization algorithm improved by sine and cosine algorithms. *Arab J Sci Eng* 46 3357-3381 (2021) **DOI:10.1007/s13369-020-05046-9**.

[24] Zhang, Q., Chen, S., Fan, Z.P. Bearing fault diagnosis based on improved particle swarm optimized VMD and SVM models. *Adv Mech Eng* 13 (2021) **DOI:10.1177/16878140211028451**.

[25] Sana, M.U., Li, Z., Javaid, F., Hanif, M.W., Ashraf, I. Improved particle swarm optimization based on blockchain mechanism for flexible job shop problem. *Cluster Comput* 26 2519-2537 (2023) **DOI:10.1007/s10586-021-03349-6**.

[26] Liu, K., Wu, S., Luo, Z., Gongze, Z., Ma, X., Cao, Z., Li, H. An intelligent fault diagnosis method for transformer based on IPSO-gcForest. *Math Probl Eng* 6610338 (2021) **DOI:10.1155/2021/6610338**.

[27] Cheng, Q., Zhan, C., Liu, Z., Zhao, Y., Gu, P. Sensitivity based multidisciplinary optimal design of a hydrostatic rotary table with particle swarm optimization. *Stroj Vestn-J Mech E* 61 432-447 (2015) **DOI:10.5545/sv-jme.2015.2478**.

[28] Chang, S.H., Jeng, Y.R. A modified particle swarm optimization algorithm for the design of a double pad aerostatic bearing with a pocketed orifice-type restrictor. *J Tribol-T ASME* 136 021701 (2013) **DOI:10.1115/1.4026061**.

[29] Srisha Rao, M.V., Jagadeesh, G. Vector evaluated particle swarm optimization (VEPSO) of supersonic ejector for hydrogen fuel cells. *J Fuel Cell Sci Tech* 7 041014 (2010) **DOI:10.1115/1.4000676**.

[30] Tang, D., Dai, M., Salido, M., Giret, A. Energy efficient dynamic scheduling for a flexible flow shop using an improved particle swarm optimization. *Comput Ind* 81 82-95 (2016) **DOI:10.1016/j.compind.2015.10.001**.

[31] Luo, W., Sun, J., Bu, C., Liang, H. Species-based particle swarm optimizer enhanced by memory for dynamic optimization. *Appl Soft Comput* 47 130-140 (2016) **DOI:10.1016/j.asoc.2016.05.032**.

[32] Liu, Z., Wang, Y., Cai, L., Zhao, Y., Cheng, Q., Dong, X. A review of hydrostatic bearing system: Researches and applications. *Adv Mech Eng* 9 (2017) **DOI:10.1177/1687814017730536**.

[33] Clerc, M., Kennedy, J. The particle swarm-explosion, stability, and convergence in a multidimensional complex space. *IEEE Trans Evolut Comp* 6 58-73 (2002) **DOI:10.1109/4235.985692**.

[34] Michalec, M., Svoboda, P., Křupka, I., Hartl, M. A review of the design and optimization of large-scale hydrostatic bearing systems. *Eng Sci Technol* 24 936-958 (2021) **DOI:10.1016/j.jestch.2021.01.010**.

[35] Li, X., Cheng, T., Li, M., Li, M., Wu, R., Wan, Y. Theoretical research on sector oil-pads mechanical property in hydrostatic thrust bearing based on constant flow. *Ind Lubr Tribol* 69 491-506 (2017) **DOI:10.1108/ILT-03-2016-0060**.

[36] Wang, Y., Liu, Z., Cai, L., Cheng, Q., Dong, X. Optimization of oil pads on a hydrostatic turntable for supporting energy conservation based on particle swarm optimization. *J Mech Eng* 64 95-104 (2018) **DOI:10.3901/JME.2018.22.095**.

[37] Cai, L., Wang, Y., Liu, Z., Cheng, Q. Carrying capacity analysis and optimizing of hydrostatic slider bearings under inertial force and vibration impact using FDM. *J Vibroeng* 17 2781-2794 (2015).

[38] Weißbacher, C., Schellnegger, C., John, A., Buchgraber, T., Pscheidt, W. Optimization of journal bearing profiles with respect to stiffness and load-carrying capacity. *J Tribol-T ASME* 136 031709 (2014) **DOI:10.1115/1.4027399**.

[39] Eberhart, R., Shi, Y. Comparing inertia weights and constriction factors in particle swarm optimization. *IEEE World Congress on Evolutionary Computation* 1 84-88 (2000) **DOI:10.1109/CEC.2000.870279**.

Acknowledgement *This research was supported by the National Natural Science Foundation of China (52075012).*

Data availability *The data that support the findings of this study are available from the corresponding author upon reasonable request.*

Received: 2025-04-23, revised: 2025-10-16, accepted: 2025-11-17 *as Original Scientific Paper.*

Author contributions *All authors contributed to the conceptualization and design of the study and participated in extensive revisions and approved the final version. Jiaqing Luo: Writing – original draft, Software, Formal analysis, Data curation; Yongsheng Zhao Data curation, Validation, Writing – review & editing; Ying Li: Writing – review & editing; Tao Zhang: Writing – review & editing; Honglie Ma: Writing – review & editing*

Declarations *The author declares that there are no competing interests.*

Metoda za optimalno načrtovanje hidrostatične vrtljive mize na osnovi FPSO algoritma

Povzetek *Nosilnost hidrostatičnih vrtljivih miz je v veliki meri odvisna od zasnove oljnih blazinic. Optimizacija parametrov oljnih blazinic lahko bistveno izboljša zmogljivost vrtljive mize ter hkrati zmanjša porabo energije. V tej študiji je predstavljen algoritem mehke optimizacije z rojem delcev (FPSO), ki v osnovno optimizacijo z rojem delcev (PSO) vpeljuje faktorje stisljivosti za optimizacijo parametrov oljnih blazinic. Rezultati optimizacije kažejo, da je rabo energije je mogoče zmanjšati za približno 40 %. Rezultati so bili potrjeni tudi eksperimentalno, pri čemer je razlika med eksperimentalnimi in teoretičnimi vrednostmi le 8 %. V primerjavi s tradicionalnimi PSO-algoritmi, FPSO kaže zanesljivejšo konvergenco pri večparametričnih problemih.*

Ključne besede *hidrostatična vrtljiva miza, metoda končnih razlik, Reynoldsova enačba, algoritem mehke optimizacije z rojem delcev, zmogljivost optimizacije*

Theoretical and Experimental Investigation on Microcosmic Surface Generation in Precision Grinding with Discrete Method

Yizun Chen[1] – Yu Sun[2] ✉

[1] Xi'an University of Architecture and Technology, School of Building Services Science and Engineering, China
[2] Xi'an University of Architecture and Technology, School of Science, China

✉ sunlyu@xauat.edu.cn

Abstract *Surface topography of the workpiece created in precision grinding is influenced by not only key process parameters, but also the distribution characteristics of active abrasive grits on the surface of the grinding wheel, including the number of active grits in the contact zone, the morphology of grits, and the cutting depth of a single grit in a normal direction. Under the conditions of small cutting depth (less than 5 μm) with small eccentrical rotation of the abrasive wheel (less than 3 μm), the influences of the original workpiece surface topography characteristics and the dynamic cutting depth of abrasive grits are often neglected in the study of microcosmic surface generation. In this paper, a discrete method (DM) is used to develop a theoretical kinematics model for the prediction of machined workpiece surface topography. Compared with the characteristics value of surface topography (scratch grooves) between experimental measurement and simulation output, the verification results from the improved prediction model of surface topography present well in comprehensively considering the influences of original surface characteristics, eccentrically rotational behavior of the abrasive wheel and the overlapped situation of scratch grooves on complex process conditions with a prediction error of about 10 %. In comparison with two commonly used empirical formulas in many other research studies, the prediction accuracy of the DM model for machined surface topography improves by 20 %. When calculating material removal volume, the prediction accuracy of incremental volume model of material removal increases approximately by 9 % to 19 % in comparison with the prediction results that take the whole cross-section area of an active grit as a key variable.*

Keywords *precision grinding, microcosmic surface topography, depth of cut, discrete method (DM), surface roughness*

Highlights

- *Presented improved kinematics model considering original surface, wheel eccentricity, and groove overlap.*
- *A discrete method (DM) is used to develop the enhanced kinematics model of surface topography.*
- *DM model improved topography prediction accuracy by 20 % compared to common empirical formulas.*
- *Material removal model accuracy improved by 9 % to 19 % compared to full cross-section-based predictions.*

1 INTRODUCTION

Precision surface grinding is one of the primary processes to acquire surface finish of the metal workpieces in high accuracy. In the process, slender and thin chips are removed from the workpiece surface by continuously working abrasive grits distributed on the surface of the grinding wheel that is installed on the machine tool spindle. The results demonstrate that surface accuracy of the machined workpiece is comprehensively influenced by linear and nonlinear factors, including process parameters, preparation and dressing/truing conditions of abrasive wheel, mechanical properties of the workpiece material, and the thermal-mechanical coupling relationship during grinding [1-4]. As one of the main surface topography characteristics in evaluating machining accuracy, surface roughness of the workpiece is closely relevant to the distribution characteristics of active abrasive grits on the surface of the wheel in axial and peripheral directions, such as the number of active grits in the contact zone, morphology combination of the grits, and cutting depth or moving trajectory path of each grit in a normal direction, etc. [5-6].

There are two types of relatively mature techniques currently utilized for predicting and evaluating surface accuracy of the machined workpiece. By means of different prediction models or digital fitting methods with some process parameters, the first technique is to establish an empirical formula for predicting the surface topography of the workpiece by considering a high correlation between the characteristic data of surface topography as measured by experiments and specific process parameters. Based on a material removal mechanism, the other technique is to develop a theoretical model of the workpiece surface topography and further to conduct the numerical solutions of surface topography characteristics in high precision. The validity of both techniques mentioned above is verified by results from the corresponding experiments.

By utilizing the first technique, Zagórski et al. [7], Li et al. [8] and Wang et al. [9] presented a prediction model using artificial neural networks and a logarithmic or exponential correlation model between surface roughness of the machined workpiece and some process parameters, including substrate size or grinding radius of the abrasive wheel, particle size and hardness of the grits, total cutting depth, rotatory speed of abrasive wheel, feed rate of workpiece, etc., and further conducted surface topography prediction or surface quality evaluation. By evaluating how strongly different surface-generation process parameters affect the outcome, and validating the results against experimental measurements and simulated surface-roughness data, this method provides a straightforward way to build a surface-topography prediction model and to estimate the expected machining accuracy of a workpiece from the chosen process parameters.. For example, numerous nonlinear influential factors are often

 DOI: 10.5545/sv-jme.2025.1386

neglected regarding surface generation under conditions of small cutting depth (less than 5 μm). In addition to process parameters, machining accuracy is also affected by the mechanical properties of the workpiece material, grinding performance and distribution characteristic of active grits in the contact zone [1-3,6], and dressing/truing/wear conditions of the abrasive wheel [5], etc. Therefore, the prediction accuracy of proposed empirical models may be limited by a lack of consideration of how the aforementioned nonlinear influential factors work on surface generation.

The grinding process is a cutting operation in which abrasive grits grind the workpiece material into the desired surface topography. Under the condition of cutting depth of a single abrasive grit in the range of a micrometer, the material removal mechanism of precision surface grinding involves slender chips of the workpiece material being gradually removed by means of continuously active abrasive grits randomly or orderly distributed on the surface of the rotating abrasive wheel. Then a microcosmic surface generation of the workpiece at a much finer scale is achieved by means of various scratch grooves formation processes along the axial direction of abrasive wheel (i.e. the direction of measuring surface roughness). By adopting the second technique based on this mechanism, many researchers systematically studied material removal behavior in the feed direction of the workpiece and then proposed theoretical models of the microcosmic surface topography of the workpiece, using cutting depth and trajectory path of abrasive grits in one dimension or two dimensions to predict surface roughness and machining accuracy. As this technique mainly depends on the material removal mechanism, the presented models of surface topography and their application have better adaptability in higher prediction accuracy than those derived from the first technique. Zhang et al. [1] proposed a theoretical model based on average protrusion heights of abrasive grits arranged in an orderly way on the surface of the abrasive wheel and further presented the theoretical model of surface topography of the workpiece machined in a trajectory direction along which the workpiece material was removed. Zhu et al. [10] proposed an improved model of surface topography by comprehensively considering process parameters, including particle size and number of abrasive grits and their distribution characteristics around the circumference of the abrasive wheel. Santhosh et al. [11] and Zou et al. [12] proposed mathematical models of surface topography based on a generation mechanism of the maximum undeformed chip of material removed by abrasive grits as randomly distributed on the surface of the abrasive wheel. Rasim et al. [3] and Duan et al. [13] studied the removal process of brittle material exerted by single and multiple abrasive grits based on the assumption that all geometries of abrasive grits were uniform in morphology, and then analyzed surface generation of the workpiece by means of scratching experiments using abrasive grits. Axinte et al. [6] and Hu et al. [14] predicted surface topography and machining accuracy with a dynamic's simulation method of the grinding process by comprehensively considering the geometry combinations of abrasive grits in shapes of spherical, conical with rounded corner and cube. Guo et al. [15] proposed prediction and evaluation models of three-dimensional surface topography in microscale based on molecular dynamics theory. Zagórski et al. [16] and Jia et al. [17] developed prediction models of surface topography on conditions of rough milling magnesium alloy and grinding ceramic materials by using tools with different geometries.

The eccentrically rotational behavior of an abrasive wheel is seldom considered as one of the influential factors on surface generation in most theoretical models of surface topography based on material removal mechanism, especially under the condition of micro-grinding. The behavior involves material being removed by many abrasive grits on the surface of an abrasive wheel eccentrically rotating with uneven radius around the center of a machine tool spindle in which assembly error between machine tool spindle and abrasive wheel spindle results in dynamic wear of the abrasive wheel. This wear results in a wavy surface on the workpiece, which can be measured in axial and peripheral directions. Likewise, the influence of original surface characteristics (such as micro-unevenness of surface) of the workpiece on actual cutting depth or material removal rate is also neglected or insufficiently considered in most scientific research. The situation presumes that a preset total cutting depth is removed from a workpiece with an "absolutely horizontal" surface with no waviness, which obviously does not conform to the actual situation. Accordingly, the influential mechanism of corresponding material removal increment between the original surface characteristics and instantaneous cutting depth per rotation of adjacent abrasive grits on surface generation is not fully revealed.

In this paper, quantitative characterization and restructuration considering the original surface topography of the workpiece are conducted by exerting a discrete method (DM) considering characteristic values of a wavy surface (e.g., peak and valley of surface waviness) as measured in experiments. The comprehensive influence of original surface characteristics and eccentrically rotational behavior of an abrasive wheel on microcosmic surface generation is studied and further, the theoretical models of instantaneous cutting depth of continuously working abrasive grits in a contact zone and incremental removal volume of material are presented. The validity and reliability of the models are verified by comparing them with the prediction outputs of the improved model and experimental results of the surface topography in axial and peripheral directions.

2 METHODS AND MATERIALS

2.1 Theoretical Model of Grinding Kinematics

The theoretical model of grinding kinematics or dynamics is illustrated in Fig. 1a. Here X, Y and Z axes represent the normal direction of the abrasive wheel, feed direction of the workpiece, and axial direction of the abrasive wheel respectively. In most research, it is assumed that the rotatory center of abrasive wheel coincides with the installation center of the machine tool spindle, which implies that the influence of eccentrically rotational movement of the abrasive wheel on material removal and the workpiece surface generation is neglected. As shown in the enlarged and three-dimensional (3D) diagram of Fig. 1b, the moving active abrasive grits in different geometries with varied protrusion heights remove materials from the workpiece, which results in microcosmic surface generation of the workpiece in shapes of many slim scratches (grooves) staggered or overlapped with a certain spatial distance. The cross-sectional characteristics (e.g., cutting depth $h_r(\varphi_i)$, contact length l_p and width B_i) of a single groove is represented in Fig. 1b (top-left view [6]). Various shapes and depths of grooves in some X-Z sectional plane of the workpiece surface (in green in Fig. 1b) are enlarged in Fig. 1c.

As shown in Fig. 1b, the workpiece surface during the grinding process is approximately composed of three parts, ie. machined surface, surface machining and surface to be machined. In the zone of machined surface, microcosmic surface topography with staggered or overlapped grooves in X–Z cross-sectional plane (in green) along the direction of the measuring surface roughness (in red) has been generated by working abrasive grits consecutively [1]. In one X–Z sectional plane in Fig. 1c, the mathematical model of surface roughness is characterized by extracting workpiece surface feature values of peak-points (v_1–v_n) and valley-points (w_1–w_n) obtained from experiments, and is used to evaluate the machining accuracy.

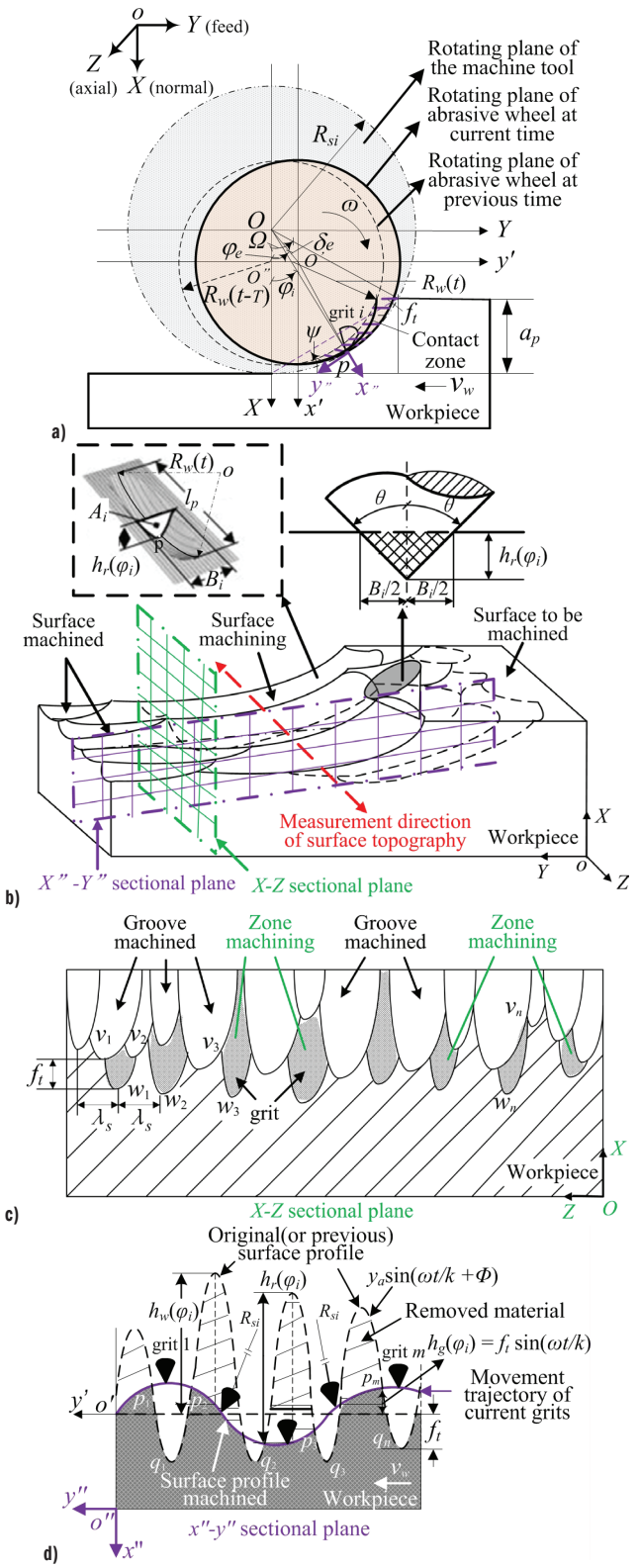

Fig. 1. Improved kinematics model and material removal model under condition of eccentrically rotating of wheel in a precision grinding process; a) kinematics model of precision grinding; b) the 3D surface topography processed by continuous abrasive grits and single groove by an abrasive grit; c) the microcosmic surface topography processed by continuous abrasive grits in one $X-Z$ sectional plane; and d) the microcosmic surface topography processed by continuous abrasive grits in one $X''-Z''$ sectional plane

In Figure 1c, the wavy surface generation and the features of surface roughness are mainly affected by key process parameters, including total cutting depth and rotating speed ratio of the workpiece and the abrasive wheel, etc, when large cutting depths of over 10 μm are adopted. It means that the effect of grit morphology and eccentric rotational behavior of the grinding wheel on the characteristics value of surface topography is not crucial in the situation. However, the situation becomes different when the cutting depth is less than 5 μm or even less than 1 μm (i.e. approximately one order of magnitude to the eccentricity value of abrasive wheel) in precision or ultra precision grinding. Set a temporary reference coordinate system $o''-x''-y''$ on a cutting point p in a peripheral direction when a single grit is scratching, as shown in contact zone in Fig. 1a. Here x''-axial and y''-axial represent normal and peripheral directions related to a single active grit on the surface of the abrasive wheel respectively. It is assumed that the number of active abrasive grits with various morphology geometries (e.g., conical, cuboid and sphere, etc. [2,3]) working simultanuously in a grit-workpiece interaction zone (i.e. grinding contact zone) is m. Influenced by the excitation of eccentric rotational behavior of the abrasive wheel, the characteristic values of peak-points (p_1-p_n) and valley- points (q_1-q_n) extracted from the wavy surface in one $x''-y''$ peripheral sectional plane (in red-purple in Fig. 1b) are shown in Fig. 1d and are fully discretized after the workpiece material is removed by active grits rotating with a certain eccentricity radius. However, these peak- and valley- points in one peripheral-sectional plane in Fig. 1d could be interfered with or coincided by those also expressed with peak-points (v_1-v_n) and valley- points (w_1-w_n) in one normal-sectional plane shown in Fig. 1c. Thus microcosmic surface topography in normal- (Fig. 1c) and peripheral- (Fig. 1d) sectional planes have close relations with the grit morphology characteristics and present the material removing capability of active abrasive grits. For example, the size, placement, shape and cutting depth of active grits in the normal direction are crucial to the length, width, depth, peak-points and valley-points of scratch grooves on the surface of the workpiece and their overlapping situation. The three-dimensional surface topography of the machined workpiece and its characteristics, such as surface waviness and surface roughness are determined by not only the characteristic values of peak-valley points on the workpiece surface in the $X-Z$ normal-sectional plane, but also the maximum values of characteristics both in the $X-Z$ normal-sectional plane and in the $X''-Y''$ peripheral-sectional plane. The aforementioned theories provide the main principles for developing an improved theoretical model of microcosmic surface topography and conducting data discretization in the research.

2.2 Theoretical Model of Eccentrically Rotational Behavior of Abrasive Wheel

During the actual grinding process, the initial error is generated by the unavoidable eccentric installation of the abrasive wheel, which results in nonuniform material removal from the workpiece. As shown in Fig. 1a, an abrasive wheel of substrate radius R_w is installed on the rotatory center O' and rotates with angular speed ω (or peripheral speed v_s). The workpiece moves forwards with feed speed v_w and the material is removed at the same peak position p and in time interval T with instantaneous and incremental cutting depth $h_r(\varphi_i)$ in the normal direction by adjacent abrasive grits in which the rotatory radii are $R_w(t)$ and $R_w(t-T)$ at the instant time t and previous time $t-T$ respectively. Microcosmic surface with a certain waviness in one normal-section plane (i.e. $X-O-Z$ plane) is generated after the material is removed, as illustrated in machining zone in Fig. 1c. As shown in the enlarged Fig. 1d, the material is removed with an incremental cutting depth of $h_r(\varphi_i)$ by eccentrically rotating grits in one peripheral section plane (i.e. $X''-O''-Y''$ plane), and the wavy

surface whose characteristics marked with peak-points ($p_1 - p_n$) and valley-points ($q_1 - q_n$), respectively, is obtained.

In Fig. 1a, the variable $\delta_e = \bar{O}\bar{O}'$ is defined as error derived from the eccentric installation of the abrasive wheel, which increases with deterioration from dynamic wear of the wheel during grinding. The value of the eccentric error is limited at the range of 1 μm to 3 μm to avoid the severe grinding chatter that significantly decreases the abrasive wheel life and results in defective products. When total cutting depth is a_p, the effective grinding radius R_{si} ($i=1,2,\ldots,m$) of a single abrasive grit i from the rotatory center O' to the cutting position p in contact zone is calculated as [18]:

$$R_{si} = R_w + \Lambda_{si} + \delta_e \cos\varphi_{e0i}, \tag{1}$$

where R_w is the radius of the abrasive wheel substrate; and Λ_{si} protrusion height of abrasive grit i from the surface of the wheel, which is a characteristic variable that conforms to the Gaussian distribution with the mean value Λ_{savg} and the standard deviation σ [1,9]. Variable φ_{e0i} is defined as the initial installation position angle of current grit i to rotatory center O', which is calculated according to the initial installation location of the abrasive wheel and the distribution position of the current abrasive grit i on the surface of the wheel. Thus, rotatory radius R_{si} of each active abrasive grit i around the machine tool spindle center O is calculated with the determination of the wheel substrate radius, the eccentric installation error of the abrasive wheel, and the initial position of the grit.

2.3 Theoretical Model of Cutting Depth of Active Grit in Peripheral-Sectional Plane

As shown in Fig. 1c, the machined scratch grooves are regularly removed with a certain material removal rate in one normal direction. The newly formed grooves are generated by the interaction between the continuously working abrasive grits distributed along the axial direction of the workpiece in the grinding contact zone with different grinding radii combined with the wheel substrate radius, protrusion height of the abrasive grit, and the eccentrical error of the wheel. Some grits cannot effectively remove the material because their protrusion heights are lower than the valley-position of the previously generated surface. This situation also occurs in the peripheral-sectional plane shown in Fig. 1d. The corresponding surface roughness is measured along the axial direction. Selecting an active grit at an instant of time t shown in Fig. 1b and one temporary reference coordinate system $X''-Y''$ at the cutting point p in normal and peripheral directions is established. The enlarged trajectory paths of the adjacent abrasive grits are illustrated in Fig. 1d. The continuously incremental cutting depth of active abrasive grit in the peripheral- sectional plane is calculated as:

$$h_{r,i}(\varphi_i) = -h_g(\varphi_i) - \Delta h(\varphi_i) + h_w(\varphi_i), \tag{2}$$

where $h_g(\varphi_i)$ is the theoretical cutting depth of a single active grit and it is usually taken as the cutting depth in most of previous research; $\Delta h(\varphi_i)$ is the dynamic deviation from the normal cutting depth derived from the eccentrically rotational behavior of the abrasive wheel, which is deduced in detail in reference [18,19]; $h_w(\varphi_i)$ the local amplitude of peak-point on the initial surface waviness of the workpiece, which is always neglected and will be substituted by the surface waviness amplitude newly generated in the prospective material removal process.

In Equation (2), as shown in Fig. 1a and Fig. 1d, the theoretical cutting depth is calculated as [4,9]:

$$h_g(\varphi_i) = f_t \sin(\varphi_i), \quad 0 \le \varphi_i \le \Omega, \tag{3}$$

where $f_t=\lambda_s\cdot(v_w/v_s)$ is the feed rate per rotation of the abrasive wheel; v_w feeding speed of the workpiece; v_s is the peripheral speed of the abrasive wheel; and λ_s is the average distance between the adjacent active grits on the surface of the abrasive wheel, which is determined by the grinding wheel substrate diameter and the distribution and size of abrasive grits, and here assumed to be the same in both axial and peripheral directions and keeps constant under the same experimental conditions. $\varphi_i=\omega t$ is the rotatory position angle of the grit around the center of the machine tool spindle. The variable t is defined as total time from the grit cutting-in to cutting-out contact zone and can be discretized when calculating the rotatory position angle. The variable φ_i is very important for determining the working position of each active grit, the corresponding peak-points and valley-points of new-formed surface waviness, and surface roughness as well. The limit value of Ω is the radial cutting-in angle of the grit [6], as shown in Fig. 1a, which is used to determine the effective interaction area. The angle ϕ is defined as the effective included angle between the peripheral direction of the grit trajectory and the normal direction while current abrasive grits scratch through the contact zone, and is calculated as:

$$\cos\phi = \frac{a_p}{l_p},$$

where l_p is the length of a single scratch groove, shown in Fig. 1b (top-left view) and approximately calculated as [13]: $l_p = \sqrt{a_p \cdot d_s}$, then: $\Omega \approx 2\arccos\sqrt{\frac{a_p}{d_s}}$,

when the rotatory position angle of the grit $\varphi_i > \Omega$, it indicates that the working grit tends to leave the grit-workpiece interaction zone, and the cutting depth turns to zero.

The dynamic deviation of the normal cutting depth $\Delta h(\varphi_i)$ in Eq. (2) is calculated as:

$$\Delta h(\varphi_i) = R_w(t) - R_w(t-T), \tag{4}$$

where $R_w(t)$ represents the actual rotation radius of active grit and is calculated as:

$$R_w(t) = \sqrt{R_{si}^2 + \delta_e^2 - 2R_{si}\delta_e\cos(\theta_s)}, \tag{5}$$

where $\theta_s = \angle PO'O = |\varphi_e - \varphi_i|$ is the rotation included angle from the machine tool spindle center to the eccentrically rotational center of the abrasive wheel; $\varphi_e=\varphi_{e0}+\theta$ is the position angle of the abrasive wheel center relative to the machine tool spindle center; $\theta=-\omega t$ is the dynamically rotatory angle of the wheel center at instant time t. Substituting the variables into Eq. (5), $R_w(t)$ becomes:

$$R_w(t) = \sqrt{R_{si}^2 + \delta_e^2 - 2R_{si}\delta_e\cos(|\varphi_{e0} - 2\omega t|)}. \tag{6}$$

2.4 Theoretical Model of Microcosmic Surface Topography with Discrete Method

The trajectory paths of consecutively active abrasive grits in a peripheral direction are illustrated in Fig. 1d. Accordingly, when the periodical time t that is taken for an active single abrasive grit from the cutting- in contact zone to cutting-out, the zone is discretized by k times with time interval T, i.e., $T=t/k$, and the material is removed by each working grit at a different cutting position with its own eccentrically rotating radius. Then, the incremental cutting depth that is expressed as the third variable in Eq. (2) by removing the previously generated wavy surface or initial surface of the workpiece, is approximately characterized with the discrete method as:

$$h_w(\varphi_i) = y_a \sin(\omega t / k + \Phi_i). \tag{7}$$

The characteristic value of surface waviness remains varied as time passes, and the grinding trajectory paths of eccentrically rotating grits change dynamically. In Equation (7), k represents the sampling times within the length of the workpiece surface. The symbol m is the number of active abrasive grits simultaneously working in the

contact zone in a peripheral direction. The complete surface waviness generated in the grinding process is restructured and connected with multiple segmented surface waves separately generated by various abrasive grits along their grinding trajectory paths. In order to improve solution precision, the surface waviness could be evenly segmented into at least 4 sections of regular sinusoidal fluctuation, i.e. $k=4Nm$ ($N=1,2,\ldots$), which implies that more discretized peak- or valley-points of the surface are solved. To simplify the calculation, here variable k is set to be equal to $4m$ ($N=1$), which implies that the discretized surface waviness of the workpiece is generated and restructured with only one individual sinusoidal fluctuation formed by abrasive grits m during the cutting-in and cutting-out process. Although the assumption may cause a little error variation, it will not have a significant impact on the acquisition of peak- points and valley-points of whole surface machined. ϕ_i is the phase difference between the motion trajectory of adjacent abrasive grits in a peripheral direction and their varying eccentrically rotational radius, and is approximately calculated by the respective position phase in a sinusoidal trajectory path.

The amplitude variable of y_a in Eq. (7) is defined as the average longitudinal height between peak- and valley-points in k sampling times along a peripheral direction and described as:

$$y_a = \frac{1}{k_n}\sum_{x=1}^{k_n} R_{a,wx}, \tag{8}$$

where k_n is the sampling times in each sampling zone for measuring the whole surface roughness. By means of discretization in unit distance interval Δx, the variable $R_{a,wx}$ represents the average longitudinal height between peak- and valley-points in local surface topography. Thus, Eq. (7) is used to restructure the initial surface topography based on surface roughness measured prior to grinding. By substituting the expression of the initial surface to the corresponding trajectory path of eccentrically rotating abrasive grits, the incremental cutting depth is obtained, and newly generated surface topographies are quantitatively characterized by peak- and valley-points in the scratch grooves. The influence of the characteristics of the initial surface waviness of the workpiece on instantaneous cutting depth is discussed in the subsequent experiment section.

Substituting above Eqs. (3), (4) [18,19] and (7) into Eq. (2) after discretization with DM, the complete expression of the microcosmic surface topography is further depicted as:

$$h_r(\varphi_i) = -f_t \sin(\omega t) - \Delta h(\omega t) + y_a \sin(\omega t / k + \Phi_i), \tag{9}$$

$$h_r(\varphi_i) = -f_t \sin(\omega t) - \frac{1}{k}\sum_{i=1}^{k} \Delta h(\omega t)\cos(i\omega T) + \\ + \frac{1}{k}\sum_{i=1}^{k} y_a \sin(i\omega T + \Phi). \tag{10}$$

The physical meanings of Eqs. (9) and (10) are that under excitation frequency of the eccentrically rotational behavior of active grits in contact zone, the material is removed with various grinding radii and cutting depth $h_r(\varphi_i)$, then the periodical surface waviness is generated by connecting discretized k segmented wavy surfaces. The fluctuating frequency of the discretized surface waviness is approximately constant, while the amplitudes of the waves are undulant due to various rotatory trajectory of each working grit.

The model of an instantaneous cutting depth of a single grit in Eqs. (9) or (10) consists of two parts. The first part is related to the feed cutting depth per rotation based on motion trajectory combined with the feed motion of the workpiece and the rotatory motion of the abrasive wheel. The second part is related to the dynamic cutting depth derived from the eccentrically rotational behavior of the abrasive wheel as well as the incremental deviation between previous and newly generated surface waviness respectively. The condition applied to the improved model of cutting depth is closer to the actual machining situation in higher prediction precision. As the value of the feed cutting depth per rotation is significantly larger than that of the dynamic cutting depths, the value of the instantaneous cutting depth $h_r(\varphi_i)$ reaches the maximum at the moment abrasive grits cut into the critical boundary of the grinding contact zone (i.e., $\varphi_i=\Omega$) and decreases gradually as the process lasts. With the superposition of the instantaneous impact of abrasive grits cutting into the eccentrically rotating abrasive wheel–machine tool spindle system, the total amplitude of the vibration and motion trajectory of active abrasive grits will correspondingly increase. With the movement of the eccentrically rotating abrasive wheel, while the cutting point p of current active grit and the rotatory center O of abrasive wheel coincide with the rotatory center O' of the machine tool spindle in a line, that is, $\varphi_{e0}=2\omega t$ or $t=\varphi_{e0}/(2\omega)$, the dynamic cutting depth derived from the eccentrically rotational behavior of the abrasive wheel decreases to minimum, and the forced vibration excited from the abrasive wheel-machine tool spindle will keep relatively stable in a lower amplitude range due to the cutting point p with the eccentricity value staying far away from the critical boundary of contact zone.

2.5 Theoretical Model of Microcosmic Surface Roughness

The total normal cutting depth of continuously active grits simultaneously removing material in the contact zone can be calculated by Eq. (11), and the surface roughness of the machined workpiece is expressed in Eq. (12) as:

$$h_r = \sum_{i=1}^{m} |h_r(\varphi_i)|, \tag{11}$$

$$R_a = \frac{1}{k}\sum_{i=1}^{k} |h_r(\varphi_i)|. \tag{12}$$

To verify the validity and prediction precision of the surface roughness model in Eq. (12), two engineering empirical formulas from references [20,21] are introduced separately as:

$$R_a = 0.256 \max\left(2|h_r(\varphi_i)|\right), \tag{13}$$

$$R_a = 1.36\lambda_{sl}^{6/5}\left(\frac{f_t}{B_s}\right)^{2/5}\left(\frac{v_w}{v_s}\right)^{2/5}\left(\frac{1}{2R_{si}}\right)^{1/5}. \tag{14}$$

In these two empirical formulas, most variables have been introduced in previous sections except that B_s is the width in axial direction or thickness of the abrasive wheel. The prediction precisions of three formulas are compared and the application limitations of them are analyzed in subsequent sections.

2.6 Influence of Morphology Characteristics of Abrasive Grits Geometries on Microcosmic Surface Generation

As shown in Fig. 1c, the instantaneous values of peak-points (v_1-v_n) and valley-points (w_1-w_n) are obtained by calculating the intersection of the previous surface waviness and currently moving trajectory of abrasive grits with various geometries morphology. In actual machining process, the main morphology of working grits is usually assumed to be conical, cuboid, spherical and their combinations [22] according to the variable of relative area ratio between top area and bottom area, as listed in Table 1. There is a small difference in machining performance if the proportion of three types of grit geometries changes. In this study, the corresponding relationship between the cutting depth in a peripheral direction and the size of three types of working grits geometries is investigated and illustrated in Fig. 2.

Table 1. Main morphology of working abrasive grits

Morphology categorization			Characteristics formulae	Projection disambiguatation
Group	Sub-type	Geometry	Criterion	Features
		Sphere	$S_1/S_2 \geq 0.8$	None
		Ellipsoid	$S_1/S_2 < 0.8$	
		Triangular pyramid	$S_1/S_2 \leq 0.1$	Three edges and one highlight peak
		Rectangular pyramid		Four edges and one highlight peak
		Pentahedron		Five edges and one highlight peak
		Rhombo-hedron		Six edges and one highlight peak
		Cone	$S_1/S_2 \leq 0.1$	Round bottom-surface and one peak
		Truncated cone	$0.1 < S_1/S_2 < 0.8$	Round bottom-surface and one top-surface
		Cylinder	$S_1/S_2 \geq 0.8$	Round bottom-surface and one top-surface
		Triangular prism	$S_1/S_2 \geq 0.8$	Three edges and one truncated top-surface
		Quadrangular prism		Four edges and one truncated top-surface
		Pentahedral prism		Five edges and one truncated top-surface
		Rhombohedral prism		Six edges and one truncated top-surface

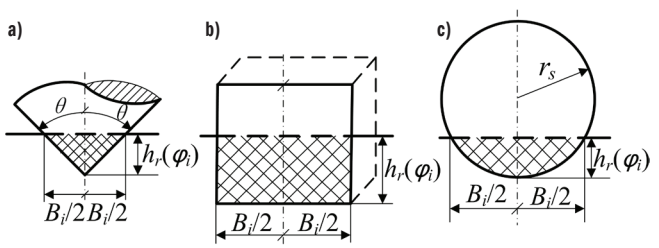

Fig. 2. The corresponding relationship between cutting depth in peripheral direction and geometric sizes of abrasive grits; a) conical; b) cuboid; and c) spherical

According to the material removal mechanism in Fig. 1b, the morphology characteristics of abrasive grits and maximum cross-section areas in contact with surface waviness are shown in Fig. 2. Neglecting the influence of plastic flow and pile-up of material, the maximum surface areas of the longitudinal cross-sections (such as the shadow zone in Fig. 2) of the material removed by single grit i with three geometry types can be calculated respectively as:

a) For conical abrasive grits: $B_1 = 2\,h_r(\varphi_i)\tan(\theta)$, then the section area of one groove by single abrasive grit is calculated as:

$$S_1 = \frac{1}{2} B_i h_r(\varphi_i) = h_r^2(\varphi_i) \cdot \tan\theta.$$

b) For cuboid abrasive grits, the ratio of length to width of a single grit is simplified to be 3:2, then $B_2 = 4/3\, h_r(\varphi_i)$, and the section area of one groove by single grit is calculated as:

$$S_2 = B_i \cdot h_r(\varphi_i) = \frac{4}{3} h_r^2(\varphi_i).$$

c) For spherical abrasive grits: $B_3 = 2\sqrt{(2r_s - h_r(\varphi_i))h_r(\varphi_i)}$, then the section area of one groove by single grit is calculated as:

$$S_3 = r_s^2 \arcsin\left(\sqrt{2\frac{h_r}{r_s} - \left(\frac{h_r}{r_s}\right)^2}\right).$$

By accumulating the surface area of continuously working abrasive grits with different geometries proportioned at the same interval, it can be calculated as:

$$S_n = \sum_{j=1}^{3} (S_j\, W_{nj}), \tag{15}$$

where W_{nj} is the proportion of numbers of active grits with one type of geometry compared to the total number of effective abrasive grits. It is assumed that the proportion is approximately equal in different grit distribution zones, then $W_{n1} + W_{n2} + W_{n3} = 1$. By scanning the cross-section of grit geometries along the trajectory path of material removed, the coordinate values of interaction points between the normal-sectional plane of the workpiece and the cross-section of abrasive grit geometries are obtained. The maximum and minimum values of interaction points are characterized as peak-points and valley-points of surface roughness and used to predict machining accuracy.

The incremental cutting depth of effective working grits is comprehensively considered in Eq. (15). Furthermore, if the geometric sizes of the overlapping grooves are larger than the distance λ_s that is related to the instantaneous cutting depth of abrasive grit, then during some interval T, the correspondingly incremental volume V_w of instantaneously-removed material along the motion trajectory of abrasive grits cutting-in and cutting-out of the material can be calculated as:

$$V_w = S_n l_p = S_n \sqrt{a_p d_s}, \quad \text{if} \quad \lambda_s \geq B_i, \tag{16}$$

$$V_w = (S_n - \lambda_s h_r(\varphi_i)) l_p = (S_n - \lambda_s h_r(\varphi_i)) \sqrt{a_p d_s}, \quad \text{if} \quad \lambda_s < B_i. \tag{17}$$

Equation (16) is commonly taken as the theoretical formula to calculate average material removal volume in most research [1,13]. In both Eqs. (16) and (17), the judging condition is to determine if the overlapping situation of the scratch grooves occurs, as illustrated in Fig. 1c. When the value of the width of the effective section of a single abrasive grit is larger than the distribution distance of adjacent grits, a certain amount of the workpiece material is incrementally removed as the consecutive scratch grooves overlap, instead of substituting the whole cross-sectional area of single grit in order to calculate the material removal volume. Thus, the calculation value with Eq. (17) is lower than the one with Eq. (16). With the increase of grinding stability and the distribution uniformity of an instantaneous cutting depth, the prediction precision increases, which is verified on the basis of comparison analysis in the following experimental section.

2.7 Experimental Conditions and Data Analysis Methods

Five groups of rough grinding and precision grinding experiments were carried out on the same precision grinder Jones and Shipman 540 (Jones and Shipman, UK), respectively. The experimental principle and measuring platform are illustrated in Fig. 3 and the main grinding parameters are listed in Table 2.

Table 2. Experimental conditions of surface grinding

Preset cutting depth [μm]	5, 15
Spindle speed [r/min]	2880
Workpiece feed speed [mm/s]	150
Eccentricity value of abrasive wheel [μm]	1, 2, 3
Initial installation position angle of abrasive wheel center [°]	30

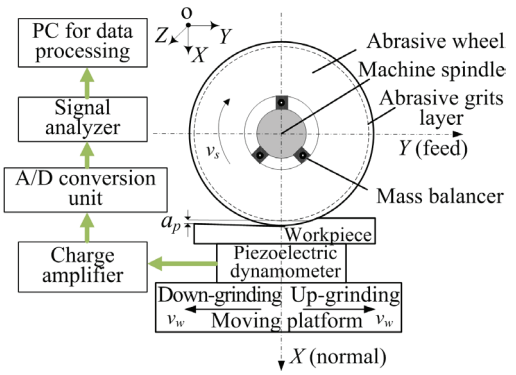

Fig. 3. Experimental principle and measurement platform of surface grinding process

Prior to every grinding experiment, the eccentricity value of the grinding wheel is calibrated and corrected with a static/dynamic balancing instrument NHY-2000-810A (Sigma, Japan) in order to decrease the disturbance errors in the eccentricity value fluctuation. This is achieved by adjusting the installation position of the mass balancer shown in Fig. 3. This ensures that the eccentricity value of the grinding wheel is effectively controlled within 1 μm, 2 μm and 3 μm according to the experimental needs. During experiments with micro-grinding or precision grinding with low material removal rate, the eccentrically rotational behavior of the abrasive wheel is examined by the in-situ dynamic balancer instrument CB-2001RGB (Sigma, Japan) installed on the motorized spindle. The process monitors the deterioration of the eccentrical vibration of the abrasive wheel with consideration of the changes in wheel wear in order to insure the eccentricity value fluctuates in the error range of ±5 % of preset one during grinding. The characteristic value of surface topography and surface roughness are measured, and the data analysis is implemented.

A monolayer resin-bonded diamond abrasive wheel with electroplated grits is applied to conduct grinding experiments. The abrasive wheel specification takes values of substrate diameter ϕ 162 mm, width 20 mm and abrasive particle size number 200/230# by ANSI-B74.16 [23]. The average size of abrasive grits is 750 μm and adjacent grits spacing is 500 μm. Considering better performance of material removal and chip formation that is beneficial for measuring peak- and valley-points of machined surface topography, the medium carbon-steel EN8 (surface size: length 20 mm × width 10 mm) is selected as sample material. The workpiece is fixed on the worktable with mode of single-pass down-grinding without lubricant, which implies that the dynamic wear of the grind wheel between two adjacent experiments is almost negligible. The material properties, machinability and composition of the sample workpiece are listed in Tables 3 and 4, respectively. The piezoelectric acceleration sensor Kistler 8764B and dynamometer Kistler 9257BA (Kistler Group, Switzerland) are assembled to measure the vibration acceleration signal and grinding force signal of the workpiece in the feed direction (motion direction of the worktable) and the normal direction (perpendicular to motion direction of the worktable), and the sampling frequency of two sensors are set to 50 kHz. The collected signals, after conversion by the charge amplifier and the A/D unit PMD-1608FS (MCC, US) where phase characteristics are also calibrated prior to every grinding experiment and are input to the signal analyzer CSI3005III (Emerson, US) and the computer equipped with graphic data analysis software LABVIEW (Ni Solutions, Sweden) for vibration signal analysis. Within the sampling length range of 5 mm on the machined surface, five different zones are randomly selected to measure surface topography. The mean values of the surface topography characteristics (including peak- and valley-amplitude of surface waviness, length and width of contact zone) are measured and the corresponding data analyses are conducted after each group of grinding experiments to effectively decrease initial noise errors of surface roughness measurement on the surface roughness profiler Talysurf6 (Taylor Hobson, UK).

Table 3. Material properties and machinability of workpiece

Heat treatment mode	normalizing treatment	Yield strength [MPa]	≥360
Hardness [HB]	170-210	Tensile strength [MPa]	600-750
Elastic modulus [GPa]	210	Elongation [%]	≥15

Table 4. Composition of workpiece material

C [%]	Si [%]	Mn [%]	P [%]	S [%]
0.35-0.45	0.05-0.35	0.6-1	≥0.06	≥0.06

3 RESULTS AND DISCUSSION

3.1 Measurement and Restructure of Initial Surface Topography of the Workpiece

The quantitative influence of characteristics distribution of the initial surface topography is studied by rough grinding experiments with conditions of δ_e=1 μm, f_t=0.3 μm, a_p=15 μm. The initial surface topography enlarged 20 times is shown in Fig. 4a. Surface roughness after grinding from two randomly selected sampling zones (1) and (2) in Fig. 4b, whose values are 0.49 μm and 0.55 μm are measured along a perpendicular direction to the grinding direction. The reconstruction of the machined surface waviness in X−Z sectional plane is conducted by Eq. (10) with values of peak-points and valley-points extracted from the sampling zones. The corresponding 3D machined surface topographies are obtained, as shown in Fig. 4c and d.

According to the analysis of the grinding kinematic and microcosmic surface generation in Section 2, surface topography is affected by the main process parameters, grit morphology, position distribution and protrusion height distribution regularity of working grits with different particle sizes. It is shown that the 3D surface topography in Fig. 4 presents a grinding situation of continuously active grits scratching through the contact zone with unequal protrusion heights (i.e. cutting edges with unequal height) of the adjacent distributing abrasive grits and with incremental cutting depth. The staggered and overlapped scratch grooves were left with characteristic values of peak-points and valley-points. The longitudinal distance between the maximum peak-point and the deepest valley-point of the scratches is about 0.6 μm almost double that of f_t by multiple abrasive grits scratching through the same position. By further extraction and calculation using Eq. (11), the average total cutting depth of each grit is about 13.87 μm with an error of 1.13 μm compared with a_p=15 μm at a proportion of 7.5 %. The error of average cutting depth is explained that the initial surface waviness and the eccentricity value of the abrasive wheel of 1 μm are introduced in Eq. (9).

3.2 Surface Topography of Workpiece in Peripheral Section under Condition of Eccentrical Rotation Excitation of Abrasive Wheel

Two groups of precision grinding experiments are designated with conditions of f_t=0.1 μm, a_p=5 μm, and conducted to verify the validity and prediction precision of the discretized theoretical models of microcosmic surface topography by comparison with experimental data and simulation outputs, where the length of the sampling zone is 0.5 mm.

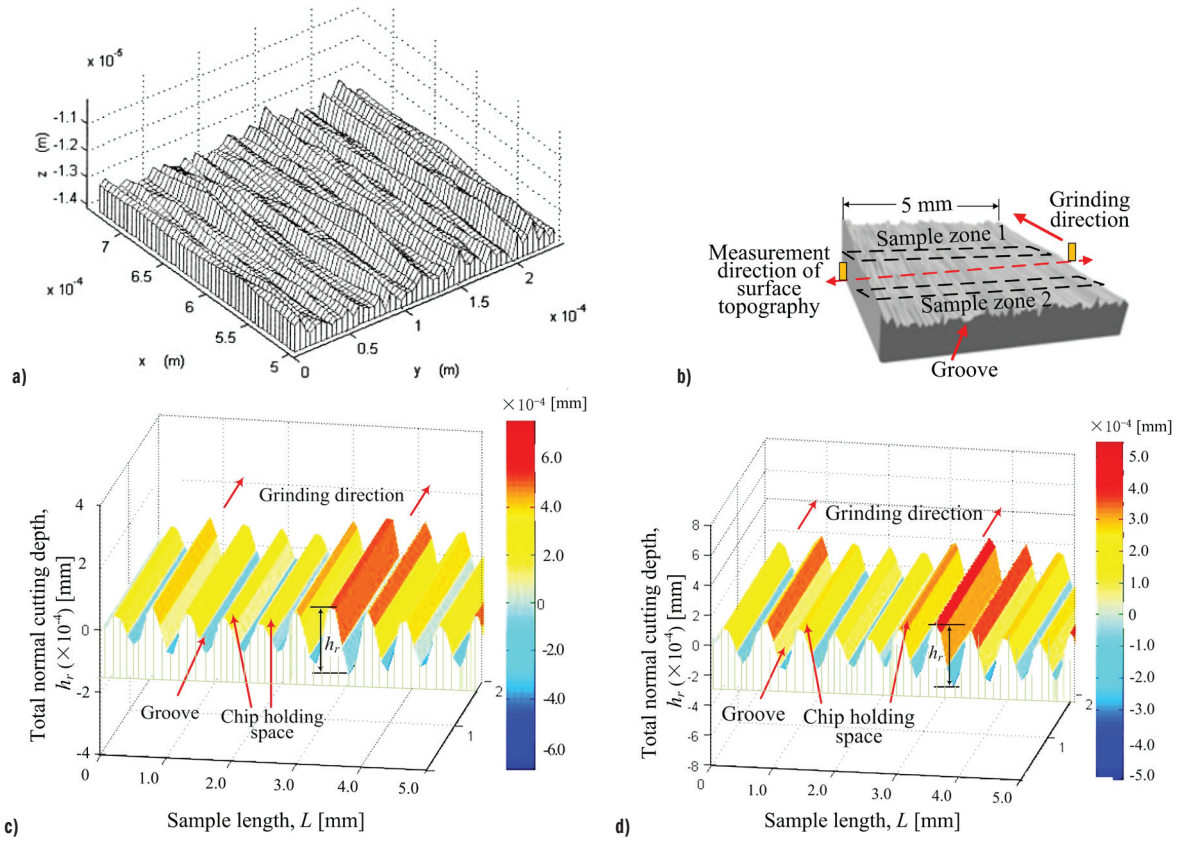

Fig. 4. 3D surface topography ; a) initial surface topography ; b) sampling zones for measuring surface topography; c) simulated surface topography in sampling zone 1; and d) simulated surface topography in sampling zone 2

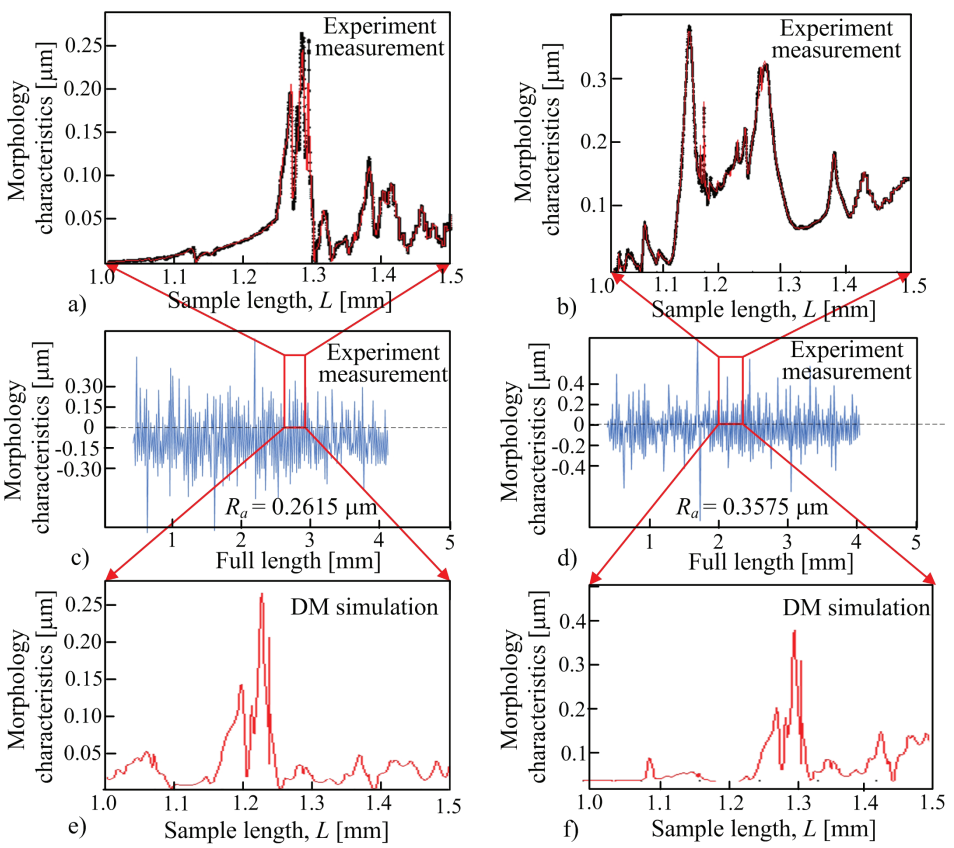

Fig. 5. Morphology characteristics of workpiece when δ_e are set to 1 μm and 2 μm; a) and b) enlarged surface topography by experiments; c) and d) actual surface topography by experiments; e) and f) enlarged surface topography by DM simulation

The first group of experiments is conducted with an eccentricity rotational value of the abrasive wheel of 1 μm. Surface roughness of the machined workpiece is measured and the corresponding characteristic value of surface topography, including peak-points and valley-points are extracted and used to restructure microcosmic surface topography with full discretization Eq. (10). The characteristics of the initial surface topography value is considered prior to precision grinding. As illustrated in Figs. 5c, a and e, respectively, surface waviness is enlarged to observe the local characteristics obtained from experiments, using a full discretization simulation. The experiments that specify eccentricity rotational values of the abrasive wheel at 2 μm by adjusting the mass balancer position and using a_p=5 μm, are conducted by continuously utilizing the workpiece machined under the condition of an eccentricity value of 1 μm. The characteristics of surface topography are measured and extracted with the same data-processing principle above, and the corresponding results are shown in Figs. 5d, b and f.

In Fig. 5c, the surface roughness of 0.2615 μm with δ_e of 1 μm is better than that of 0.3575 μm with de of 2 μm as shown in Fig. 5d, which implies that the former is smoother than the latter. Surface roughness of the latter deteriorates approximately by 37 %. By comparing the local characteristics of the surface waviness in details shown in Figs. 5a and b from experiments with the discretization simulation outputs shown in Figs. 5e and f, it is shown that the common tendency of the two results is, at some discrete moment, the total amount of instantaneous cutting depth of continuously effective abrasive grits in the peripheral plane improves up to the maximum as the static or theoretical cutting depth, the absolute value of first variable in Eqs. (9) or (10), keeps a higher proportion. Meanwhile, a stronger dynamic impact exists when the error rate of abrasive grits cutting into the material increases with an increase of the eccentrically rotational excitation. As the process becomes gradually stable, the instantaneous cutting depth distinctly decreases and keeps a small fluctuation with a cutting depth per rotation of 0.1 μm. With the increase of δ_e from 1 μm to 2 μm, the effective grinding radius of variable R_{si} of a single grit in the contact zone increases according to Eq. (1) and the depiction in Fig. 1. Accordingly, the instantaneous cutting depth in a local region distinctly increases to almost 2 times, and surface roughness of the latter is larger by 1.37 times than the former. The tendency implies that the grinding stability deteriorates, and serious vibration occurs. In comparison of the characteristics of peak-points and valley-points from the experiments and restructure simulations, both the fluctuation tendency of surface waviness coincide very well. The prediction error was about 50 %. But when δ_e is 1 μm, the error decreases to within 20 % when δ_e is 2 μm. This indicates that on a condition of stable grinding, the total predicted amount of cutting depth is lower as the characteristics of the initial surface topography are considered in the third variable in Eq. (9) when calculating total instantaneous cutting depth. The particle size, distance distribution and grinding preference of abrasive grits have a small influence on the material removal process during micro-grinding as well. Unlike the situation in which eccentrical vibration increases, the influential proportion of the incremental cutting depth in the second variable in Eq. (9) derives from eccentric rotational behavior increases, which results in the descending influential proportion of the morphology characteristics of abrasive grits. Such considerations result in predictions closer to actual grinding situations.

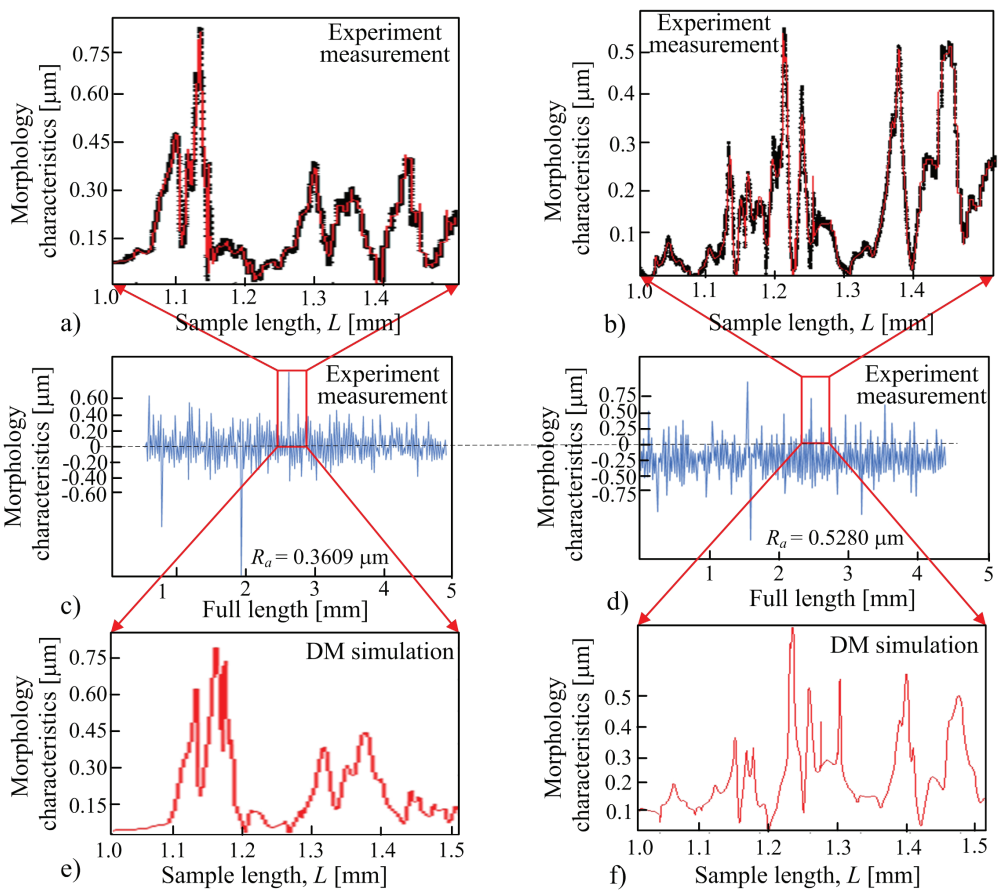

Fig. 6. Morphology characteristics of workpiece when δ_e are set to 2 μm and 3 μm; a) and b) enlarged surface topography by experiments; c) and d) actual surface topography by experiments; e) and f) enlarged surface topography by DM simulation

The second group of experiments are conducted by referring to the same technique and data analysis when δ_e turn to 2 μm and 3 μm (the upper limit value of stable grinding in most research). Separately, the responding characteristic values of surface waviness and surface roughness are measured and restructured. Surface waviness is enlarged to observe local characteristics as obtained from experiments and full discretization simulations are illustrated in Fig. 6a to Fig. 6f respectively.

In Fig. 6c, the surface roughness of 0.3609 μm with δ_e of 2 μm is better than 0.5280 μm with δ_e of 3 μm shown in Fig. 6d, which implies that the former is distinctly better than the latter in smoothness of surface waviness, where the surface roughness of the latter deteriorates approximately up to 47 %. Compared with the local characteristics of surface waviness shown in Figs. 6a and b from experiments and the discretization simulation outputs in Figs. 6e and f, the results imply the tendency is similar to the situation of the aforementioned paragraph. In other words, with the increase of δ_e from 1 μm to 2 μm, the local characteristics values increase greatly, and the tendency of experimental data and simulation outputs coincide very well etc. Though δ_e only ranges from 2 μm to 3 μm, the instantaneous cutting depth in the local region distinctly increases to approximately 46 %. However, the prediction error decreases to within 10 % when the eccentricity value is 3 μm. It indicates that with the development of stronger eccentrical vibration, the influential proportion of the incremental cutting depth derived from the eccentric rotational behavior increases significantly and even closely approximates to the static or theoretical one, which results in prediction outputs closer to the actual grinding situation where the error is approximately 10 %.

3.3 The Prediction Precision Analysis of the Improved Theoretical Models of Surface Roughness and Incremental Material Removal Volume

Using experimental protocols with δ_e ranging from 1 μm to 3 μm, and substituting the process parameters in Table 2 and the characteristics values (including peak-points and valley- points of surface waviness), into the theoretical models of surface roughness in Eq. (12) (with DM) and empirical Eqs. (13) and (14) respectively, the corresponding prediction results of surface roughness in conditions of changed speed ratio between the feed speed of the workpiece and the peripheral speed of the abrasive wheel from 0.006 to 0.012 are illustrated in Fig. 7.

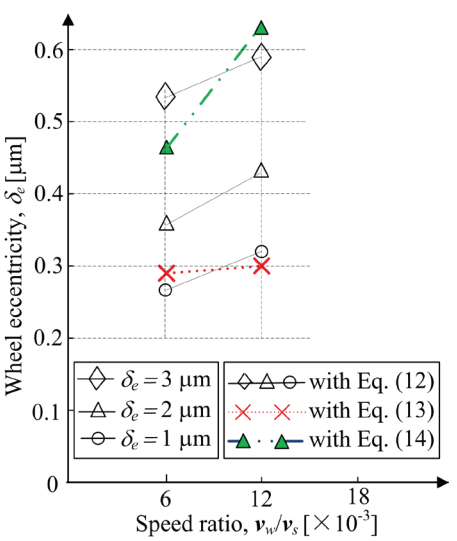

Fig. 7. Surface roughness obtained from experimental data, DM model and two fitting formulas

In Figure 7, the prediction values of surface roughness in accordance with 'dynamic deteriorated' δ_e from 1 μm, 2 μm to 3 μm in Eq. (12) are 0.26 μm, 0.36 μm, 0.53 μm respectively when the lower speed ratio is adopted, i.e. at a low feed speed of the workpiece or a high peripheral speed of the abrasive wheel. The value of surface roughness obtained in simplified Eq. (13) is 0.27 μm, which is similar to the stable situation (δ_e = 1 μm), and the prediction error is almost 4 %. The value of surface roughness obtained in complicated Eq. (14) is 0.48 μm similar to the result of a relatively unstable grinding state (δ_e = 3 μm), where the prediction error is almost 9 %. The tendency indicates that the physical considerations in Eq. (13) are mainly based on the material removal process with a crucial index of instantaneous cutting depth to predict machining accuracy in accordance with the actual grinding process. Meanwhile, Eq. (14) coincides with the situation considering various nonlinear influential factors of the process parameters. The prediction errors are 25 % and 33 % respectively when comparing the values in Eqs. (13) and (14) using the prediction value in Eq. (12) with δ_e of 2 μm.

Furthermore, the prediction values of surface roughness with δ_e of 1 μm, 2 μm, 3 μm in Eq. (12) are 0.32 μm, 0.43 μm, 0.58 μm respectively when the higher speed ratio is adopted. The value of surface roughness obtained in simplified Eq. (13) and complicated Eq. (14) are 0.30 μm and 0.63 μm, respectively. Both results are also similar to those in stable and unstable situations. The result demonstrates that Eqs. (13) and (14) are suitable to approximately predict the machined accuracy level compared with the outputs in Eq. (12). The analysis further indicates that Eq. (13) is more suitable to be utilized to predict surface roughness in a stable grinding process, especially in micro-grinding, i.e. the instantaneous cutting depth stays even. The prediction accuracy improves when the mean value of maximum cutting depth in several sampling zones is adopted, i.e. the formula is simplified and improved in the following formula: $R_a = 0.256\,\overline{\max(2|h_r(\varphi_i)|)}$. Equation (14) is more suitable to be utilized to predict surface roughness in various grinding process parameters, especially in rough grinding with a larger cutting depth.

To further improve the statistical reliability of the kinematic model for predicting surface roughness, the detailed peak-points (Peak-P) and valley-points (Val-P) are extracted from the experimental measurement (R_a-Exp) and prediction outputs (R_a-DM) based on Figs. 5 and 6, and depicted in Table 5 with the increase of δ_e. Here the sampling length of 0.5 mm is divided into 10 zones to measure the surface topography every 0.05 mm. In Table 5, it is shown that with the increase of δ_e, the maximum of Peak-P or Val-P (absolute value) from experiments are almost close to prediction outputs with the DM model. Meanwhile, the larger amplitude difference highlighted between Peak-P and Val-P occurs both in R_a-Exp and R_a-DM and increases significantly, which demonstrates that the instantaneous cutting depth of active grits is becoming deeper due to the deteriorated vibration excitation derived from the wheel rotating behavior with a larger eccentricity value.

According to the experiment protocol in varying δ_e from 1 μm to 3 μm and using the lower speed ratio, substituting the instantaneous cutting depth and the size of cuboid geometries of abrasive grits whose area is maximum in three types of geometries into the prediction model of total material removal volume per unit area in Eq. (16), (whose area variable is adopted with whole section area of working abrasive grits), and using the improved Eq. (17), (whose area variable is the incremental area considering overlapping situation of scratch grooves), the prediction results for average material removal volume with both Eqs. (16) and (17) are illustrated in Fig. 8. It is noted that the number of effective abrasive grits is the one working in some peripheral section along the wheel surface.

Table 5. Peak-points and valley-points of machined surface topography by experiments and DM model

Sampling zone	$\delta_e = 1\ \mu m$				$\delta_e = 2\ \mu m$				$\delta_e = 3\ \mu m$			
	R_a-Exp		R_a-DM		R_a-Exp		R_a-DM		R_a-Exp		R_a-DM	
	Val-P	Peak-P	Val-P	Peak-P	Val-P	Peak-P	Val-P	Peak-P	Val-P	Peak-P	Val-P	Peak-P
1.00-1.05	-0.020	0.007	-0.026	0.04	-0.02	0.05	-0.20	0.005	-0.15	0.10	-0.20	0.12
1.05-1.10	-0.025	0.009	-0.028	0.05	-0.25	0.08	-0.25	0.10	-0.35	0.05	-0.25	0.20
1.10-1.15	-0.026	0.02	-0.02	0.10	-0.10	0.38	-0.27	0.10	-0.30	0.30	-0.27	0.20
1.15-1.20	-0.18	0.04	-0.15	0.15	-0.25	0.26	-0.27	0.15	-0.23	0.25	-0.37	0.15
1.20-1.25	-0.12	0.20	-0.01	0.27	-0.20	0.20	-0.22	0.27	-0.25	0.55	-0.22	0.82
1.25-1.30	-0.08	0.27	-0.22	0.04	-0.15	0.32	-0.10	0.38	-0.25	0.40	-0.30	0.53
1.30-1.35	-0.19	0.05	-0.26	0.02	-0.27	0.10	-0.18	0.30	-0.18	0.36	-0.18	0.50
1.35-1.40	-0.20	0.06	-0.26	0.03	-0.20	0.20	-0.25	0.10	-0.15	0.52	-0.45	0.15
1.40-1.45	-0.17	0.12	-0.25	0.05	-0.02	0.15	-0.20	0.15	-0.02	0.54	-0.15	0.50
1.45-1.50	-0.25	0.07	-0.22	0.05	-0.25	0.14	-0.23	0.17	-0.10	0.54	-0.38	0.12

Meanwhile, the corresponding surface roughness and specific grinding forces within the workpiece length of 20 mm in normal and feed directions in conditions of the same process parameters with speed ratio 0.006 and various eccentricity values measured by experiments are illustrated in Fig. 9.

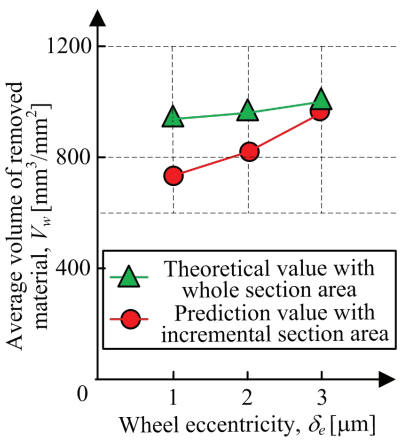

Fig. 8. Average volume of material removed by effective abrasive grits in contact zone

As shown in Fig. 8, it is assumed that the proportion of conical, cuboid, and spherical are 20 %, 60 %, and 20 %, respectively. In a stable condition of the same δ_e of 1 μm, as the whole section area of any type of grit geometry is obviously larger than the incremental section area of the continuously active grit removing material, the theoretical value of average material removal volume of 900 mm^3 obtained with Eq. (16) is distinctly larger than that of 720 mm^3 with the incremental Eq. (17), in which the error is about 25 %. A similar tendency occurs in surface roughness and specific grinding forces when the average material removal volume varies with the Eqs. (16) and (17), as shown in Fig. 9. With the increase of eccentrical vibration excitation when δ_e is 3 μm, the overlapping situation decreases the accumulated material removal volume removed by each working grit, accompanying the trend of slowing down in grinding forces in Figs. 9b and c. The incremental material removal volume of 860 mm^3 with Eq. (17) is further close to the theoretical one of 946 mm^3 with Eq. (16), in which the error is approximately by 10 %. The regularity of varying material removal volume is similar with surface roughness when the eccentricity value varies. Comparing the theoretical value of material removal volume, the prediction precision improves 19 % and 14 % with Eq. (17) when δ_e are 1 μm and 2 μm, respectively. The result demonstrates that both the prediction models of incremental material removal volume and the model of surface roughness are

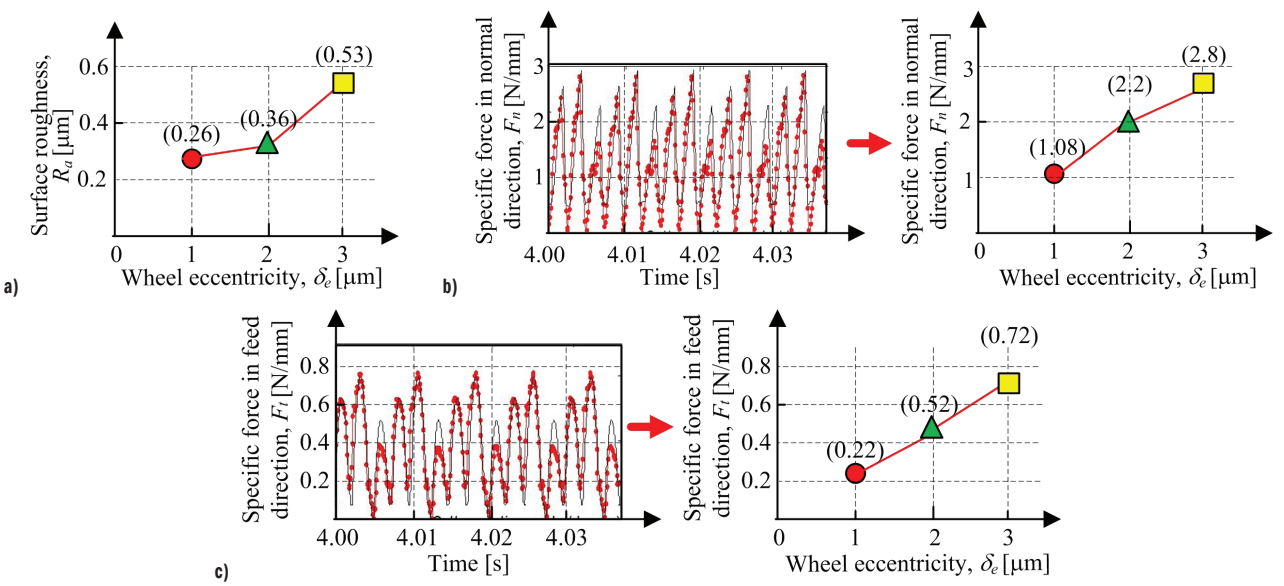

Fig. 9. Surface roughness and specific grinding forces with the increase of wheel eccentricity values; a) Surface roughness by experiments; b) Specific grinding force in normal direction by experiments and evolution trend; c) Specific grinding force in feed direction by experiments and evolution trend

more suitable for engineering application in the actual grinding process.

4 CONCLUSIONS

It is a key research issue to monitor grinding quality, control process stability, and acquire a high-quality machined surface in order to understand profoundly the influence of various linear and nonlinear factors on the material removal mechanisms in the generation of the final machined surface topography of the workpiece. In this paper, the comprehensive effects of nonlinear factors, such as the initial surface waviness of the workpiece, the eccentrically rotational behavior of the abrasive wheel and the morphology combination of abrasive grits on the instantaneous/dynamic cutting depth are depicted systematically, and the improved prediction model for microcosmic surface topography is presented by utilizing a discrete method and restructuring technique. By comparing grinding experiments, previous empirical engineering formulas, and 2D and 3D simulation results, the reliability of the prediction model of surface topography is verified. The models proposed in the paper are practical for predicting the microcosmic surface topography and its generation in higher accuracy in cases of rough grinding, precision grinding and even micro-grinding processes. The important conclusions of this study include:

1. In micro-grinding or precision grinding with a low removal rate, both the initial surface waviness and the eccentric rotational behavior of the abrasive wheel have a significant influence on grinding process stability and surface topography generation but are commonly neglected in most of previous research. By comparing experimental data and simulation outputs from theoretical models of surface topography including peak- and valley-points, and the surface roughness under varying conditions of eccentricity rotational values, the improved theoretical model of microcosmic surface topography can reliably calculate the characteristic value of peak and valley of surface topography under complex conditions in considering the influential factors above. With an increase in the eccentricity rotational values of the abrasive wheel, the prediction precision of microcosmic surface topography increases with an error of 10 %.
2. Compared to the theoretical model of surface topography in Eq. (12), in considering varying eccentricity rotational behaviors of the abrasive wheel, the prediction result based on the simplified model of surface topography with Eq. (13), which is an empirical engineering formula, is closer to stable process with an error of 4 % when the eccentricity rotational value is 1 μm, while the prediction result based on the complicated model of surface topography with Eq. (14), which is another empirical engineering formula, is closer to a relatively unstable process with an error of 9 % to 19 % when the eccentricity rotational value is 3 μm.
3. Compared to commonly used theoretical model of material removal rate, which takes a whole section area of abrasive grit geometry as a variable, under varying eccentricity rotational conditions, the improved model of material removal volume comprehensively considers both the overlapping status of scratch grooves formed by continuously working abrasive grits and the morphology combination of abrasive grits geometries. Thus, the improved model is suitable for predicting the actual grinding situation with higher accuracy. The prediction accuracy for material removal volume with the improved model in this paper improves almost 9 % by adopting the maximum of the eccentricity rotational value of 3 μm, and approximately 19 % and 14 % by adopting the eccentricity rotational values of 1μm and 2 μm respectively, relative to the results derived from the commonly used theoretical model.
4. The quantitative assessment of machining quality demonstrates that surface roughness generated in precision grinding increases significantly when a stable grinding process tends to instability, e.g., when the wheel eccentricity value changes from 1 μm to 3 μm. The eccentric rotation deviation of the grinding wheel should be minimized to less than 3 μm, which is the upper limit value of stable grinding, or should even be 'eliminated' prior to grinding with a dressing or reconditioning technique, as well as by use of dynamic balancer with the aid of some specific devices.

Nomenclatures

a_p total cutting depth of grinding process, [μm]
B_i width of abrasive grit geometry in contact zone, [μm]
d_s grinding wheel diameter, [mm]
f_t feed rate per revolution of grinding wheel, [μm]
h_r total normal cutting depth of continuously active grits simultaneously removing material in contact zone, [μm]
$h_r(\varphi_i)$ incremental cutting depth of a single active abrasive grit in contact zone, [μm]
$h_g(\varphi_i)$ theoretical cutting depth of a single active abrasive grit, [μm]
$\Delta h(\varphi_i)$ normal cutting depth with eccentrically rotational deviation, [μm]
$h_w(\varphi_i)$ local amplitude of peak-point on initial surface waviness of workpiece, [μm]
k sampling times within full length of workpiece surface
k_n sampling times in each sampling zone
L sample length on the machined surface, [mm]
l_p length of a single scratch groove, [μm]
m number of active abrasive grits simultaneously working in contact zone in peripheral direction, [grits/mm^2]
$OXYZ$ grinding kinematics coordinate system of machine tool
$O'X'Y'Z'$ grinding kinematics coordinate system of abrasive wheel
$O''X''Y''Z''$ local kinematics coordinate system of working grit in contact zone
R_a surface roughness of workpiece machined, [μm]
$R_{a,wx}$ average longitudinal height between peak-points and valley-points in local surface topography, [μm]
$R_w(t)$ rotatory radius of adjacent abrasive grits at the instant time t, , [μm]
$R_w(t–T)$ rotatory radius of adjacent abrasive grits at the previous time $t–T$, [μm]
R_{si} rotatory radius of active abrasive grit i around machine tool spindle center, [μm]
S_j section area of one groove formed by single abrasive grit with some type of geometry, [μm^2]
S_n full section area of grooves formed by all abrasive grits with three types of geometries, [μm^2]
T discrete time interval between current and adjacent working grits, [s]
v_s peripheral speed of grinding wheel, [m/s]
v_w feed speed of workpiece, [m/s]
V_w incremental volume of instantaneously removed material, [mm^3]
W_{nj} proportion of numbers of active grits with different types of geometries, [%]
y_a average longitudinal height between points of peak and valley along peripheral direction, [μm]
δ_e wheel eccentricity value, [μm]
σ standard deviation of protrusion heights of abrasive grits, [μm]
ϕ effective included angle of current abrasive grit, [°]
Φ_i phase difference of motion trajectory of adjacent abrasive grits in peripheral direction, [°]
φ_{e0} initial position angle of abrasive wheel, [°]
φ_e relative position angle with actual wheel rotational center, [°]
φ_i rotatory position angle of the grit i, [°]
ω angular velocity of abrasive wheel, [rad/s]
θ rotational angle of spindle of abrasive wheel, [°]
θ_s rotation included angle from machine tool spindle center to eccentrically rotational center of abrasive wheel, [°]

λ_s average distance between adjacent active abrasive grits on surface of grinding wheel, [μm]
Ω entire included angle of grit in interaction zone, [°]
ψ phase difference between previous and current waviness trajectory, [rad]
Λ_{si} protrusion height of abrasive grit i from surface of wheel, [μm]
Λ_{savg} mean protrusion height of abrasive grit i from surface of wheel, [μm]

References

[1] Zhang, Y.Z., Fang, C.F., Huang, G.Q, Xu, X.P. Modeling and simulation of the distribution of undeformed chip thickness in surface grinding. *Int J Mach Tools Manuf* 127 14-27 (2018) **DOI:10.1016/j.ijmachtools.2018.01.002**.

[2] Darafon, D., Warkentin, A., Bauer, R. 3D metal removal simulation to determine uncut chip thickness, contact length and surface finish in grinding. *Int J Adv Manuf Technol* 66 1715-1724 (2013) **DOI:10.1007/s00170-012-4452-1**.

[3] Rasim, M., Mattfeld, P., Klocke, F. Analysis of the grit shape influence on the chip formation in grinding. *J Mater Process Technol* 226 60-68 (2015) **DOI:10.1016/j.jmatprotec.2015.06.041**.

[4] Tian, L., Fu, Y.C., Li, H.Y., Ding, W.F. The influence of speed on material removal mechanism in high speed grinding with single grit. *Int J Mach Tools Manuf* 89 192-201 (2015) **DOI:10.1016/j.ijmachtools.2014.11.010**.

[5] Yang, X. X., Zhang, B., Bai, Q., Kang, R.K., Tang, J.G. Effect of grit size on subsurface characterization of pure iron subjected to the orthogonal cutting. *Int J Adv Manuf Technol* 120 5793-5806 (2022) **DOI:10.1007/s00170-022-09156-6**.

[6] Axinte, D., Butler-Smith, P., Akgun, C. On the influence of single grit micro-geometry on grinding behavior of ductile and brittle materials. *Int J Mach Tools Manuf* 74 12-18 (2013) **DOI:10.1016/j.ijmachtools.2013.06.002**.

[7] Zagórski, I., Kulisz, M., Szczepaniak, A. Roughness parameters with statistical analysis and modelling using artificial neural networks after finish milling of magnesium alloys with different edge helix angle tools. *Stroj Vestn-J Mech Eng* 70 27-41 (2024) **DOI:10.5545/sv-jme.2023. 596**.

[8] Li, C., Piao, Y.C., Meng, B.B., Hu, Y.X, Li, L.Q., Zhang, F.H. Phase transition and plastic deformation mechanisms induced by self-rotating grinding of GaN single crystals. *Int J Mach Tools Manuf* 172 1-15 (2022) **DOI:10.1016/j.ijmachtools.2021.103827**.

[9] Wang, X.Z., Liu, Q.Y., Zheng, Y.H., Xing, W., Wang, M.H. A grinding force prediction model with random distribution of abrasive grits: considering material removal and undeformed chips. *Int J Adv Manuf Technol* 120 7129-7233 (2022) **DOI:10.1007/s00170-022-09213-0**.

[10] Zhu, H., Ge, S.R., Huang, X.L., Zhang, D., Liu, J.L. Experimental study on the characterization of worn surface topography with characteristic roughness parameter. *Wear* 255 309-314 (2003) **DOI:10.1016/S0043-1648(03)00215-1**.

[11] Santhosh, D.K., Pušavec, F., Krajnik, P. Grinding of cemented carbide using a vitrified diamond pin and lubricated liquid carbon dioxide. *Stroj vestn-J Mech Eng* 69 435-443 (2023) **DOI:10.5545/sv-jme.2023.658**.

[12] Zou, L., Li, H., Wang, W.X., Huang, Y., Li, Y.T. A precision grinding technology for zirconium alloy tubes based on ultrasonic wall thickness automatic measurement system. *Int J Adv Manuf Technol* 121 323-335 (2022) **DOI:10.1007/s00170-022-09314-w**.

[13] Duan, N., Yu, Y.Q., Wang, W.S., Xu, X.P. Analysis of grit interference mechanism for the double scratching of monolayer silicon carbide by coupling the FEM and SPH. *Int J Mach Tools Manuf* 120 49-61 (2017) **DOI:10.1016/j.ijmachtools.2017.04.012**.

[14] Hu, Z.W., Chen, Y., Lai, Z.Y., Yu, Y.Q., Xu, X.P. Coupling of double grains enforces the grinding process in vibration-assisted scratch: Insights from molecular dynamics. *J Mater Process Technol* 304 1-14 (2022) **DOI:10.1016/j.jmatprotec.2022.117551**.

[15] Guo, X., Zhai, C., Kang, R. The mechanical properties of the scratched surface for silica glass by molecular dynamics simulation. *J Non-Cryst Solids* 420 1-6 (2015) **DOI:10.1016/j.jnon-crysol.2015.04.001**.

[16] Zagórski, I. Surface roughness evaluation of AZ31B magnesium alloy after rough milling using tools with different geometries. *Stroj Vestn-J Mech Eng* 70 355-368 (2024) **DOI:10.5545/sv-jme. 2023.885**.

[17] Jia, X.F., Wang, H., Zhao, F. Critical grinding depth of ultrasonic vibration-assisted electrolytic in-process dressing grinding in ZTA ceramics. *Int J Adv Manuf Technol* 120 7127-7141 (2022) **DOI:10.1007/s00170-022-09066-7**.

[18] Chen, Y., Jiang, C., Chen, X., Huang, G.Q., Hu, Z.Y. Study on the dynamic influence of the distribution of cutting depth on the ground surface quality in a precision grinding process. *J Manuf Process* 107 134-143 (2023) **DOI:10.1016/j.jmapro.2023.10.028**.

[19] Zhang, S.J., Yu, J.J., Tu, S., Xiong, Z.W. A theoretical and experimental study of spindle imbalance induced forced vibration and its effect on surface generation in diamond turning. *Int J Mach Tools Manuf* 133 61-71 (2018) **DOI:10.1016/j.ijmachtools.2018.06.002**.

[20] Zhang, B., Uematsu, T. Surface generation mechanism in helical scan grinding: An analytical study. *J Mater Process Technol* 91 206-214 (1999) **DOI:10.1016/S0924-0136(98)00415-4**.

[21] Song, T.J., Zhou, Z.X., Li, W., Huang, X.M., Chen, Q.D. Roughness model for helical flute of cemented carbide end milling under grinding. *J Mech Eng* 53 185-192 (2017) **DOI:10.3901/JME.2017.17.185**.

[22] Chen, Y., Chen, X., Hu, Z.W., Duan, N. Comprehensive influence of ultrasonic vibration-assisted technology on material removal mechanism under the excitation of regenerative vibration in precision grinding process. *Int J Adv Manuf Technol* 129 3645- 3657 (2023) **DOI:10.1007/s00170-023-12571-y**.

[23] ANSI-B74.16:2002. American national standard: procedure for bulk density of abrasive grains. American national standards institute (2002) New York.

Acknowledgement *This work is supported by the Natural Science Basic Research General Program of Shaanxi Province (Grant No 2024JC-YBMS-428). The authors would like to thank Ph.D. Kathleen League of DePaul University of Chicago and Prof. Bill Martin of University of Kansas from the United States for proofreading & editing.*

Received: 2025-05-13, revised: 2025-08-03, accepted: 2025-09-22
as Original Scientific Paper.

Data Availability *The data that underpin the results of this research are available for use by other researchers. Additionally, the corresponding author can provide additional raw data upon reasonable request.*

Author Contribution *Yizun Chen: Methodology, Formal analysis, Validation, Writing - original draft; Yu Sun: Methodology, Supervision, Project Administration, Writing - review & editing. All authors have contributed significantly to this work and thoroughly reviewed and approved the final version of the manuscript.*

Teoretična in eksperimentalna raziskava mikroskopske tvorbe površine pri preciznem brušenju z diskretno metodo

Povzetek *Topografija površine obdelovanca, ustvarjena pri preciznem brušenju, je odvisna ne le od ključnih procesnih parametrov, temveč tudi od porazdelitvenih značilnosti aktivnih abrazivnih zrn na površini brusnega kolesa, vključno s številom aktivnih zrn v kontaktni coni, njihovo morfologijo in globino reza posameznega zrna v normalni smeri. Pri majhnih globinah reza (manj kot 5 μm) in majhnih ekscentričnih rotacijah brusnega kolesa (manj kot 3 μm) se vplivi prvotne topografije površine obdelovanca ter dinamične globine reza abrazivnih zrn pogosto zanemarjajo pri proučevanju mikroskopske tvorbe površine. V tem članku je uporabljena diskretna metoda (DM) za razvoj teoretičnega kinematičnega modela za napoved topografije obdelane površine. Primerjava med izmerjenimi in simuliranimi vrednostmi značilnosti topografije (prask) je pokazala, da izboljšani napovedni model topografije površine dobro zajame vplive začetne površinske topografije, ekscentričnega vrtenja brusnega kolesa ter prekrivanja prask pri kompleksnih procesnih pogojih, z napako napovedi približno 10 %. V primerjavi z dvema pogosto uporabljenima empiričnima enačbama se natančnost napovedi modela DM za topografijo obdelane površine izboljša za 20 %. Pri izračunu volumna odstranjenega materiala se natančnost napovedi inkrementalnega volumskega modela odstranitve materiala poveča za približno 9 % do 19 % v primerjavi z rezultati napovedi, ki kot ključno spremenljivko upoštevajo celotno presečno površino aktivnega zrna.*

Ključne besede *precizno brušenje, mikroskopska topografija površine, globina reza, diskretna metoda (DM), hrapavost površine*

Dynamics of Aero-Engine Dual-Rotor Systems under Multi-Flight Attitudes and Simultaneous Rub-Impact Faults

Peixun Tang[1,2] – Zhengminqing Li[1,2] ✉ – Xiaojing Ma[1,2] – Yiyan Chen[1,2] – Xi Liu[1,2]

[1] College of Mechanical and Electrical Engineering, Nanjing University of Aeronautics and Astronautics, Nanjing 210016, China
[2] National Key Laboratory of Helicopter Aeromechanics, Nanjing University of Aeronautics and Astronautics, Nanjing 210016, China

✉ lzmq_cmee@nuaa.edu.cn

Abstract *High-maneuverability combat aircraft exert extreme loads on aero-engines, potentially triggering destructive rotor-stator rub-impacts and thereby pose a severe threat to flight safety. This study establishes a four-degree-of-freedom (4-DOF) rotor-bearing-disk model for a dual-disk system, specifically tailored to simulate the coupling effects of simultaneous rub-impact faults under diverse flight attitudes and maneuver loads. For benchmarking purposes, a corresponding model free of rub-impact is accordingly constructed. The Newmark-β method is employed to derive solutions for both models. To evaluate how maneuver loads influence the dynamic characteristics of the system, a parametric investigation is conducted to assess the effects of dual-disk rub-impact across three key flight attitudes, namely, rolling, pitching, and yawing. This research offers a critical theoretical basis for enhancing vibration control and conducting failure analysis in fighter engine design, ultimately contributing to the development of safer and more reliable rotor systems.*

Keywords *rotor dynamics, maneuvering flight, bearing nonlinear force, rub-impact, nonlinear characteristic*

Highlights

- *Dual-disk rub-faults show higher vibration and richer spectra under all flight conditions.*
- *Pitching (G = 2.5–7.5) causes peak vibration; yawing dominates X-direction response.*
- *Spectrogram at G = 2.5 shows the richest spectral features across loading conditions and*
- *Bifurcation diagrams show frequent regime shifts under pitching at G = 2 with rub-impact.*

1 INTRODUCTION

The continuous advancement of various technologies has significantly enhanced the maneuverability of modern fighter aircraft, enabling them to execute complex tactical maneuvers and gain air supremacy. Aircraft maneuverability refers to the capability of an aircraft to alter its flight energy, direction, spatial position, and orientation relative to the airframe. It is commonly quantified using specific maneuverability metrics [1].

In recent years, numerous researchers have investigated rotor system dynamics under flight conditions. Sakata et al. [2,3] studied a flexible rotor system with a movable base, analyzed its behavior under pitching motion and demonstrated a good agreement between theoretical and experimental results. Wei and Fan [4] developed a dynamic model for a dual-rotor system using the transfer matrix method and derived expressions for additional loads during composite maneuvers such as horizontal circling, diving, and pull-up. Zhu and Chen [5] established the equations of motion for a multi-disk rotor system under arbitrary flight attitudes applying Lagrange's equations. Hou and Chen [6] investigated the dynamic behavior of a nonlinear aircraft rotor system during Herbst maneuvering flight, with emphasis on load control for safety considerations. The equations of motion were established using Lagrange's equations, incorporating flight parameters to characterize the influence of maneuvering flight. Han and Chu [7] as well as Chen et al. [8], examined subharmonic and mixed resonance in a cracked rotor under foundation excitation, accounting for the angular motion of the aircraft. Gao et al. [9] created a simplified aero-engine rotor model and employed finite element analysis to assess how maneuvering loads affect blade tip clearance. Pan et al. [10] developed a model of a rotor-bearing-disk system to analyze dynamic responses under rolling, pitching, and yawing loads, noting that different flight modes could lead to distinct rub-impact and frequency separation phenomena. Friction faults have consistently been a major concern for researchers, as they are one of the primary causes of vibration in fighter engines. Saeed et al. [11] examined the oscillatory properties of a controlled asymmetric rotor system during rotor-stator rub-impact events and developed the governing equations for the system's dynamics, which incorporate both rub and impact forces. Wu et al. [12] established a nonlinear dynamic model of a dual-rotor-support-casing system. They refined the casing modeling using the finite element method (FEM) and component mode synthesis (CMS), treating inter-shaft rub-impact as a nonlinear excitation, and investigated the effects of rub stiffness and rotational speed ratio on self-excited vibration. Prabith and Krishna [13] employed a time-variational method to study the rub-impact stability of a dual-rotor system under co-rotation and counter-rotation conditions, evaluating the influence of key parameters such as contact stiffness, friction coefficient, and clearance. Pan et al. [14] developed a comprehensive finite element model of a rotor system that integrates multiple nonlinear factors, including blade-casing rub-impact forces, climbing maneuver loads, nonlinear Hertzian contact in bearings, rotor unbalance, gravity, and squeeze film damper effects. They systematically evaluated the dynamic response of the system under varying rub-impact stiffness values, oil film clearances, and bearing clearances. Lin et al. [15] investigated blade-coating rub-impact defects in aero-engines by developing a finite element model validated through a rotor test-rig and a coupled rotor-blade-coating system with a 0-2-1 support configuration. They identified the key

vibration response characteristics through quantitatively analyzing rub-impact forces at different rotational speeds and invasion depths. Sousa et al. [16] developed a dynamic model of a disk-shaft-bearing system based on Lagrange's equations and the finite element method, which incorporates the strain energy and kinetic energy of the shaft, as well as the kinetic energies of the disk and unbalance mass. Their work has provided a comprehensive theoretical and experimental investigation of the dynamic behavior of rotating machinery under the combined effects of base excitation and disk-stator rub-impact. Yu et al. [17,18] developed a modal analysis method for aero-engine rotors under friction and investigated the complex nonlinear modes of a hybrid rotor system and their effects on vibration responses.

Rotor systems, both in aero-engines and other applications, have been extensively studied worldwide. Prior research has examined the influence of maneuvering loads on aero-engine rotor systems, providing valuable theoretical insights into their behavior under various flight conditions. Several studies have developed rotor system models that incorporate multiple nonlinear components, enabling more comprehensive analyses. Others have integrated rub-impact faults into rotor dynamics modeling, laying a foundation for investigating failure mechanisms. Nonetheless, studies on dual-disc aero-engine rotor systems experiencing simultaneous rub-impact under multi-directional maneuvering loads remain limited. To address this gap, it is essential to develop a dynamic analysis model capable of simulating rub-impact defects and multi-directional maneuver loads. This study makes the following specific contributions: (1) Conduct a systematic investigation into the dynamics of the rotor under three fundamental flight attitudes: rolling, pitching, and yawing; (2) Develop a nonlinear dynamic model that integrates rub-impact force (for dual-disks), gravity, disk unbalance force, maneuver load-induced excitations, and nonlinear bearing force, and solve it using a Newmark-β numerical scheme tailored for complex rotor systems; (3) Perform a comparative analysis of the rotor system's response with and without dual-disk rub-impact faults across various flight attitudes, and a comparative analysis of dynamic responses across multiple flight conditions under the coupling of rub-impact and varying flight attitudes (different load conditions).

2 METHODS AND MATERIALS

2.1 System Assumptions and Total Degrees of Freedom

In practice, the rotor system of a traditional aero-engine exhibits high complexity due to the presence of multiple components and intricate interactions. In this research, the system is reduced to a two-disc rotor bearing system, with the remaining essential assumptions listed below:

1. Modern fighter aircraft are typically equipped with 1 to 3 engines, and for the sake of this study, the rotor system of the fighter engine is assumed to be situated at the fighter's center of mass.
2. The entire aero-engine rotor system has been streamlined into a single flexible shaft with two centered mass disks.
3. Rotor unbalance is assumed to occur on a single plane, as this represents a common and critical source of vibration in practical rotor systems.
4. The model's central axis is elastic, with torsional and axial vibrations of the spinning axis neglected.

The finite element approach is used to create a rotor-bearing system model with 5 nodes and 24 degrees of freedom based on the assumptions listed above. Out of these 24 degrees of freedom, 20 are the total degrees of freedom of the 5 nodes, with the remaining 4 being the degrees of freedom of the 2 supporting bearing outer rings in the X and Y axes.

2.2 Basis of Finite Element Theory

The Rayleigh model is used primarily in this research to develop the finite element model design of the rotor-rolling bearing's shaft of part. Each node of the Rayleigh beam has 4 degrees of freedom, as illustrated in Fig. 1, and the generalized coordinate system is stated as:

$$\mathbf{u}=\left[x_a,y_a,\theta_{xa},\theta_{ya},x_b,y_b,\theta_{xb},\theta_{yb}\right]^T \tag{1}$$

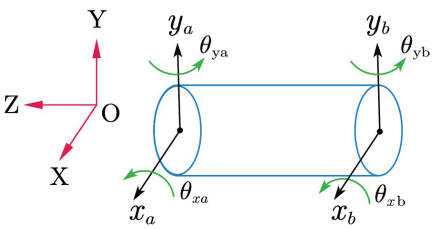

Fig. 1. Finite element model of rotor shaft (Rayleigh beam model)

The Rayleigh beam element model's mass, stiffness, damping, and gyroscopic moment matrix can all been solved using the Lagrange's equation and numerical programming tools [19]. The particular matrices are given in Eqs. (2) to (5):

$$\mathbf{M}_s^T=\frac{\rho\pi\left(R^2-r^2\right)l}{420}\begin{bmatrix}156&0&0&22l&54&0&0&-13l\\0&156&-22l&0&0&54&13l&0\\0&-22l&4l^2&0&\mathbf{0}&-13l&-3l^2&0\\22l&0&0&4l^2&13l&0&0&-3l^2\\54&0&0&13l&156&0&0&-22l\\0&54&-13l&0&0&156&22l&0\\0&13l&-3l^2&0&0&22l&4l^2&0\\-13l&0&0&-3l^2&-22l&0&0&4l^2\end{bmatrix}, \tag{2}$$

$$\mathbf{M}_s^R=\frac{\rho\pi\left(R^4-r^4\right)}{120l}\begin{bmatrix}36&0&0&3l&-36&0&0&3l\\0&36&-3l&0&0&-36&-3l&0\\0&-3l&4l^2&0&0&3l&-l^2&0\\3l&0&0&4l^2&-3l&0&0&-l^2\\-36&0&0&-3l&36&0&0&-3l\\0&-36&3l&0&0&36&3l&0\\0&-3l&-l^2&0&0&3l&4l^2&0\\3l&0&0&-l^2&-3l&0&0&4l^2\end{bmatrix}, \tag{3}$$

$$\mathbf{K}_s=\frac{E\pi\left(R^4-r^4\right)}{4l^3}\begin{bmatrix}12&0&0&6l&-12&0&0&6l\\0&12&-6l&0&0&-12&-6l&0\\0&-6l&4l^2&0&0&6l&2l^2&0\\6l&0&0&4l^2&-6l&0&0&2l^2\\-12&0&0&-6l&12&0&0&-6l\\0&-12&6l&0&0&12&6l&0\\0&-6l&2l^2&0&0&6l&4l^2&\mathbf{0}\\6l&0&0&2l^2&-6l&0&0&4l^2\end{bmatrix}, \tag{4}$$

$$\mathbf{G}_s=\frac{\rho\pi\left(R^4-r^4\right)}{60l}\begin{bmatrix}0&-36&3l&0&0&36&3l&0\\36&0&0&3l&-36&0&0&3l\\-3l&0&0&4l^2&-3l&0&0&-l^2\\0&-3l&4l^2&0&0&-3l&l^2&0\\0&36&-3l&0&0&36&3l&0\\-36&0&0&-3l&36&0&0&3l\\-3l&0&0&l^2&3l&0&0&4l^2\\0&-3l&-l^2&0&0&3l&4l^2&0\end{bmatrix}, \tag{5}$$

2.3 Rolling Bearing Model

Bearings play a critical role as support structures in rotor systems, and the nonlinear contact force influences the rotor system's dynamic behavior. Fig. 2 shows a schematic representation of a rolling bearing, which consists of four main components: an inner ring, an outer ring, rolling elements (balls) and a cage. Additionally, two assumptions must be made while calculating the rolling bearing model:

1. Assume that the ball is evenly placed between the inner and outer ring raceways, and that the ball and raceway are inpure rolling.
2. Assume that the bearing's inner ring is solidly linked to the rotating shaft.

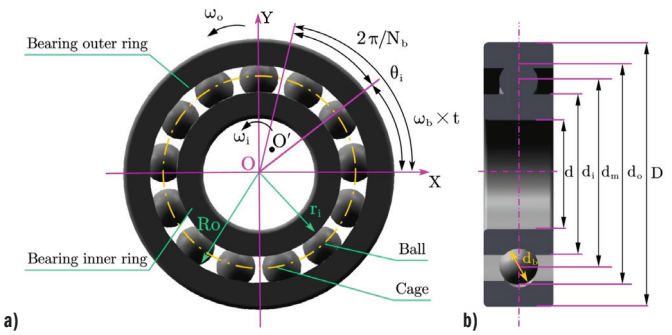

Fig. 2. The diagram of rolling bearing model; a) front view of rolling bearing, b) rolling bearing profile

The outside raceway's radius is denoted as R_o, whereas the inner raceway's radius is r_i, d_i and d_o are the diameters of the bearing's inner and outer rings, respectively, and D is the outer ring diameter of the bearing. The bearing pitching diameter is denoted by d_m, which is equal to: $d_m=(d_i+d_o)/2$, [20].

Assume that the linear speed of the contact point between a ball and the bearing outer ring is v_o, the linear speed of the contact point with the bearing inner ring is v_i, the rotational speed of the bearing outer ring is ω_o, the rotation angular speed of the inner ring is ω_i, and the radius of the outer raceway is R_o. The inner raceway radius is r_i. So v_i and v_o can be represented as:

$$v_i=\omega_i r_i, \quad v_o=\omega_o R_o, \tag{6}$$

Given that the bearing's outer ring is stationary, the formula for calculating the cage speed is as follows:

$$v_c=(v_i+v_o)/2. \tag{7}$$

The angular velocity of the bearing cage is further derived as:

$$\omega_c=\frac{\omega_i r_i}{R_o+r_i},, \tag{8}$$

Given the number of bearing balls is N_b and the angular position of the j ball is θ_j, then:

$$\theta_j=\omega_c t+\frac{2\pi}{N_b}(j-1), \quad j=1,2,3,\cdots,N_b. \tag{9}$$

The Hertz contact theory states that if the normal contact deformation δ_{bj} between the ball and the raceway is positive, the contact pressure between them is given by the f_{bj} as:

$$f_{bj}=K_b(\delta_{bj})^{3/2}=K_b\left(x\cos\theta_{bj}+y\sin\theta_{bj}-\delta_0\right)^{3/2} \cdot H(x\cos\theta_{bj}+y\sin\theta_{bj}-\delta_0). \tag{10}$$

In Equation (10), K_b represents the Hertz contact stiffness, the value of δ_0 is the bearing clearance, contact variable is $\delta_j=x\cos\theta_j+y\sin\theta_j-\delta_0$, and $H(\delta_j)$ the Heaviside function:

$$H(\delta_j)=\begin{cases}1, & H(\delta_j)>0\\ 0, & H(\delta_j)<0\end{cases}.$$

Therefore, the bearing force in the X and Y directions can be described as follows using the Hertz contact theory mentioned above:

$$\begin{cases}F_{b_x}=\sum_{j=1}^{N_b}f_{jx}\\ F_{b_y}=\sum_{j=1}^{N_b}f_{jy}\end{cases}. \tag{11}$$

2.4 Rub-Impact Force Model

Figure 3 depicts the mechanical model of rotor rub-impact, where O is the position of the rotor center of mass at rest. When the rotor's displacement r exceeds the clearance δ_c between the rotor and stator, rub-impact occurs. The rotor's displacement r is defined $r=\sqrt{x^2+y^2}$ [21].

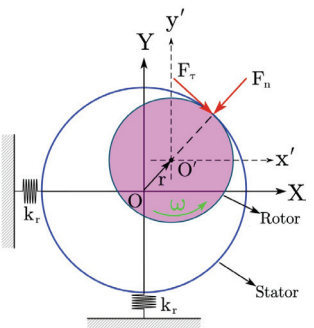

Fig. 3. Schematic representation of the rub-impact phenomenon between the stator and rotor

In addition, K_o indicates rub-impact stiffness, F_n represents normal force, F_τ is determined by Coulomb's law, which is tangential force, and μ represents friction coefficient. The normal and tangential forces during rub-impact are calculated as follows:

$$\begin{cases}F_n=\begin{cases}0 & \text{if } r\le\delta\\ k_o(r-\delta) & \text{if } r>\delta\end{cases},\\ F_\tau=\mu\cdot F_n\end{cases} \tag{12}$$

The rub-impact force can be decomposed into Cartesian coordinates xoy,

$$\begin{bmatrix}f_y\\ f_x\end{bmatrix}=-K\frac{k_o(r-\delta)}{r}\begin{bmatrix}1 & -\mu\\ \mu & 1\end{bmatrix}\begin{bmatrix}x\\ y\end{bmatrix}, \tag{13}$$

where K is the Heaviside function, and the contact angle is $\gamma=\arctan(y/x)$. When $r>\delta$, $K=1$, otherwise, $K=0$.

2.5 Modeling of 3 Basic Flight Attitudes (Rolling, Pitching, Yawing)

The work of Zhu and Chen [5] established the foundation for the maneuvering flight model, detailing its derivation and results. Based on the assumptions outlined in Section 2.1, the basic coordinates of the aircraft engine in flight are given, and the fighter is defined as pitching flight by twisting around the X axis, rolling flight around the Z axis and yawing flight around the Y axis, which are described in Fig. 4. Based on the Hamiltonian principle, the kinetic and potential energy of the rotor support system, as well as the Lagrange function are computed, and the differential equation for the system's motion

is derived. The matrix of increased damping $\mathbf{C}_{B,i}$, stiffness $\mathbf{K}_{B,i}$, and load introduced by maneuvering flight $\mathbf{F}_{B,i}$ is shown below:

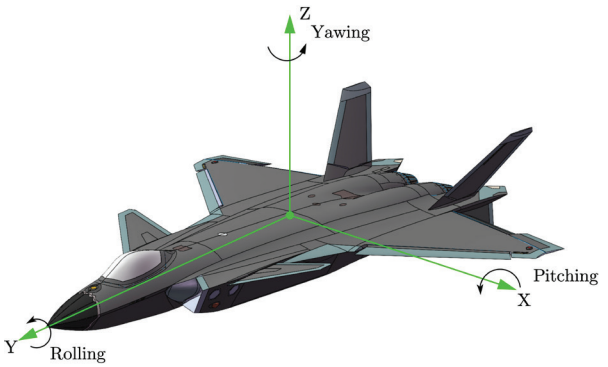

Fig. 4. Schematic diagram of the 3 basic flight attitudes of a fighter aircraft

$$\mathbf{K}_{B,i}=\begin{bmatrix} -m_i\left(\dot{\theta}_{B,y}^2+\dot{\theta}_{B,z}^2\right) & m_i\left(\dot{\theta}_{B,x}\dot{\theta}_{B,y}-\dot{\theta}_{B,z}\right) & 0 & 0 \\ m_i\left(\dot{\theta}_{B,x}\dot{\theta}_{B,y}-\dot{\theta}_{B,z}\right) & -m_i\left(\dot{\theta}_{B,x}^2+\dot{\theta}_{B,z}^2\right) & 0 & 0 \\ 0 & 0 & 0 & 0 \\ 0 & 0 & 0 & 0 \end{bmatrix}, \tag{14}$$

$$\mathbf{C}_{B,i}=\begin{bmatrix} 0 & -2m_i\dot{\theta}_{B,z} & 0 & 0 \\ 2m_i\dot{\theta}_{B,z} & 0 & 0 & 0 \\ 0 & 0 & 0 & 0 \\ 0 & 0 & 0 & 0 \end{bmatrix}, \tag{15}$$

$$\mathbf{F}_{B,i}=\begin{bmatrix} -m_i\left(\dot{X}_B-\dot{\theta}_{B,z}Y_B+\dot{\theta}_{B,y}\dot{Z}_B\right)-m_iz_i\left(\dot{\theta}_{B,x}\dot{\theta}_{B,z}+\ddot{\theta}_{B,y}\right) \\ -m_i\left(\ddot{Y}_B-\dot{\theta}_{B,z}X_B+\dot{\theta}_{B,x}\dot{Z}_B\right)-m_iz_i\left(\dot{\theta}_{B,y}\dot{\theta}_{B,z}+\ddot{\theta}_{B,x}\right) \\ -I_i\ddot{\theta}_{B,x}-\Omega I_{p,i}\dot{\theta}_{B,y} \\ \Omega I_{p,i}\dot{\theta}_{B,x}-I_i\ddot{\theta}_{B,y} \end{bmatrix}, \tag{16}$$

In Equations (14) to (16) $\ddot{X}_B$, $\ddot{Y}_B$, and $\ddot{Z}_B$ denote the linear accelerations along the X, Y, and Z axes, respectively, while $\ddot{\theta}_{B,x}$, $\ddot{\theta}_{B,y}$, and $\ddot{\theta}_{B,z}$ represent the angular accelerations about these axes. Similarly, $\dot{X}_B$, $\dot{Y}_B$, and $\dot{Z}_B$ refer to the corresponding linear velocities, and $\dot{\theta}_{B,x}$, $\dot{\theta}_{B,y}$, and $\dot{\theta}_{B,z}$ indicate the angular velocities about the X, Y, and Z axes.

2.6 Global Equation of Aero-Engine Rotor Dynamics

Building on the theoretical descriptions of the components of the rotor subsystem provided in Sections 2.1 to 2.5, this section describes the assembly of the complete rotor system, with its three-dimensional structure shown in Fig. 5. Furthermore, when paired with the fundamental equation of rotor dynamics, the overall motion equation of rotor dynamics under multi-factor conditions is completed, as presented in Eq. (17). It should be mentioned that Pan et al. [10] demonstrated the correctness of the dynamic modeling approach in the study and validated that the modeling method is not impacted by the number of nodes or whether is a step axis. $\mathbf{M}_{all}$ indicates the mass matrix of the entire system, and $\mathbf{C}_{all}$ represents the damping matrix of the entire system, $\mathbf{K}_{all}$ covers the stiffness matrix of the whole system, $\mathbf{G}_{all}$ represents the gyro matrix of the total system, and $\mathbf{C}_B$ and $\mathbf{K}_B$ represent the additional damping matrix and stiffness matrix created by maneuvering loads, respectively.

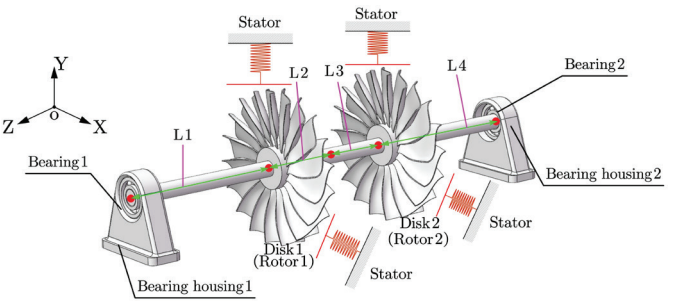

Fig. 5. Schematic of the entire rotor system

$\mathbf{F}_e$ represents the imbalance force matrix of the disc, $\mathbf{F}_b$ represents the bearing's nonlinear force matrix, $\mathbf{F}_a$ represents the dynamic load force matrix, $\mathbf{F}_g$ signifies the gravity matrix, and $\mathbf{F}_{rub}$ illustrates the disk's rub-impact force matrix.

$$\begin{aligned}&\mathbf{M}_{all}\ddot{\mathbf{X}}+\left(\mathbf{C}_{all}-\omega\mathbf{G}_{all}+\mathbf{C}_B\right)\dot{\mathbf{X}}+\left(\mathbf{K}_{all}+\mathbf{K}_B\right)\mathbf{X}\\&=\mathbf{F}_e+\mathbf{F}_b+\mathbf{F}_a+\mathbf{F}_g+\mathbf{F}_{rub}.\end{aligned} \tag{17}$$

The mass of rotor system is expressed as follows. $\mathbf{M}_{all}$ contains the mass matrix of the shaft, disks, and bearing outer rings. The two support bearings' outer rings possess centralized masses of m_{b1} and m_{b2}, respectively.

$$\mathbf{M}_{all}=\begin{bmatrix} \mathbf{M} & & & & & \\ & m_{b1} & & & & \\ & & m_{b1} & & & \\ & & & m_{b2} & & \\ & & & & m_{b2} & \end{bmatrix}.. \tag{18}$$

The damping of rotor system is expressed as follows: $\mathbf{C}$ is the proportional damping matrix of the shaft, specifically Rayleigh damping as used in this paper, calculated via Eq. (19). Here, $\alpha=2(\xi_1/\omega_1-\xi_2/\omega_1)/(1/\omega_2^2-\omega_1^2)$ and $\beta=2(\xi_2\omega_2-\xi_1\omega_1)/(\omega_2^2-\omega_1^2)$ where ξ_1, ξ_2 and ω_1, ω_2 denote the rotor system's first two damping ratios and natural frequencies, while c_{b1} and c_{b2} represent the connection damping between the bearing's supporting outer ring and bearing housing.

$$\mathbf{C}=\alpha\mathbf{M}+\beta\mathbf{K}, \tag{19}$$

$$\mathbf{C}_{all}=\begin{bmatrix} \mathbf{C} & & & & & \\ & c_{b1} & & & & \\ & & c_{b1} & & & \\ & & & c_{b2} & & \\ & & & & c_{b2} & \end{bmatrix}. \tag{20}$$

The gyro matrix of the rotor system is composed as follows:

$$\mathbf{G}_{all}=\begin{bmatrix} \mathbf{G} & & & & & \\ & 0 & & & & \\ & & 0 & & & \\ & & & 0 & & \\ & & & & 0 & \end{bmatrix}, \tag{21}$$

where $\mathbf{G}$ represents the matrix of the shaft system and the disc system.

$$\mathbf{K}_{all}=\begin{bmatrix} \mathbf{K} & & & & & \\ & k_{b1} & & & & \\ & & k_{b1} & & & \\ & & & k_{b2} & & \\ & & & & k_{b2} & \end{bmatrix}, \tag{22}$$

where **K** is the stiffness matrix of the whole shafting. k_{b1} and k_{b2} are bearing1 and bearing2 support stiffness. The extra stiffness, damping, and force matrix of the rotor system under maneuvering load are computed using Eqs. (14) to (16).

$$\mathbf{C}_{\mathrm{B}}=\begin{bmatrix}0 & -2m_j\omega_z & 0 & 0\\ 2m_j\omega_z & 0 & 0 & 0\\ 0 & 0 & 0 & 0\\ 0 & 0 & 0 & 0\end{bmatrix},\quad (j=1,2), \tag{23}$$

$$\mathbf{K}_{\mathrm{B}}=\begin{bmatrix}-m_j\left(\omega_y^2+\omega_z^2\right) & m_j\left(\omega_x\omega_y-\omega_z\right) & 0 & 0\\ m_j\left(\omega_x\omega_y+\omega_z\right) & -m_j\left(\omega_x^2+\omega_z^2\right) & 0 & 0\\ 0 & 0 & 0 & 0\\ 0 & 0 & 0 & 0\end{bmatrix},\quad (j=1,2). \tag{24}$$

When the fighter rolling, the additional force is given as:

$$\mathbf{F}_{\mathrm{a}}=\begin{bmatrix}0,0,0,0,2m_1\omega_x v_z,2m_1\omega_x v_y,0,0,0,\\ 0,0,0,2m_2\omega_x v_z,2m_2\omega_x v_y,0,0,0,0,\\ 2m_{b1}\omega_x v_z,2m_{b1}\omega_x v_y,2m_{b2}\omega_x v_z,2m_{b2}\omega_x v_y\end{bmatrix}^T. \tag{25}$$

When the fighter pitching, the additional force is given as:

$$\mathbf{F}_{\mathrm{a}}=\begin{bmatrix}0,0,0,0,\pm m_1\omega_x v,0,\pm J_{p1}\omega\omega_x,0,0,0,0,\\ 0,\pm m_2\omega_x v,0,\pm J_{p2}\omega\omega_x,0,0,0,0,\\ 0,\pm m_{b1}\omega_x v,0,\pm m_{b2}\omega_x v,0\end{bmatrix}^T, \tag{26}$$

where the sign of the force depends on the direction of the pitching motion: a negative sign "–"is used for diving (nose-down motion), and a positive sign "+" is used for climbing (nose-up motion).

When the fighter is undergoing yawing, the additional force induced by the maneuver load is given by:

$$\mathbf{F}_{\mathrm{a}}=\begin{bmatrix}0,0,0,0,0,m_1\omega_y v,0,J_{p1}\omega\omega_y,0,0,0,\\ 0,0,m_2\omega_y v,0,J_{p2}\omega\omega_y,0,0,0,\\ 0,0,m_{b1}\omega_y v,0,m_{b2}\omega_y v\end{bmatrix}^T. \tag{27}$$

The unbalanced force matrix is:

$$\mathbf{F}_{\mathrm{e}}=\begin{bmatrix}0,0,0,0,m_1e_1\omega^2\cos(\omega t+\varphi),m_1e_1\omega^2\sin(\omega t+\varphi),0\\ ,0,0,0,0,0,m_2e_2\omega^2\cos(\omega t+\varphi),m_2e_2\omega^2\sin(\omega t+\varphi),\\ 0,0,0,0,0,0,0,0,0,0,0\end{bmatrix}^T. \tag{28}$$

The gravity matrix is:

$$\mathbf{F}_{\mathrm{g}}=\begin{bmatrix}0,0,0,0,0,-m_1g,0,0,0,0,0,0,0\\ -m_2g,0,0,0,0,0,0,0,-m_{b1}g,0,-m_{b2}g\end{bmatrix}^T. \tag{29}$$

The bearing nonlinear Hertz force matrix is as follows:

$$\mathbf{F}_{\mathrm{b}}=\begin{bmatrix}-F_{bx1},-F_{by1},0,0,0,0,0,0,0,0,0,0,0\\ 0,0,-F_{bx2},-F_{by2},0,0,F_{bx1},F_{by1},F_{bx2},F_{by2}\end{bmatrix}^T. \tag{30}$$

The rub-impact matrix formed between the rotor and stator is:

$$\mathbf{F}_{\mathrm{rub}}=\begin{bmatrix}0,0,0,0,\ \mathrm{F}_{rubx1},\ \mathrm{F}_{ruby1},0,0,0,0,0,\\ \mathrm{F}_{rubx2},\ \mathrm{F}_{ruby2},0,0,0,0,0,0,0,0,0,0\end{bmatrix}^T. \tag{31}$$

The displacement of parameter **X** may be written in the form of:

$$\mathbf{X}=\left[\mathbf{x},x_{b1},y_{b1},x_{b2},y_{b2}\right]^T, \tag{32}$$

where **x** represents the displacement vector that includes each of the nodes.

3 RESULTS AND DISCUSSION

This section presents a comprehensive analysis of the dynamic behavior of the rotor system under different flight attitudes and maneuver loads. The effects of rub-impact and non-rub-impact conditions on shaft orbits and *Y*-direction frequency spectra are compared at a rotational speed of ω = 2400 rad/s under maneuvering loads of G = 2.5, G = 5, G = 7.5, and G = 10 (where G denotes the maneuver load intensity, defined as the ratio of the maneuver-induced inertial force to the gravitational force). Additionally, the bifurcation behavior is examined under a fixed maneuvering load of G = 2 within a rotational speed range of 500 rad/s to 3000 rad/s. These analyses are presented in Sections 3.1, 3.2, and 3.3 for pitching, rolling, and yawing maneuver conditions, respectively. Furthermore, Section 3.4 investigates the coupled effects of maneuvering loads and rub-impact under various flight attitudes to assess their influence on the disk 1 subsystem. The same parameter sets as those in Sections 3.1, 3.2, and 3.3 are employed for consistency.

Table 1 lists the key parameters of the rotor system used in the simulations. The calculation formulas for the maneuver load intensity of G under pitching, rolling, and yawing circumstances are as follows: $G=\omega_x v^z/g$, $G=\omega_z v^z/g$ and $G=\omega_y v^z/g$, (g=10 m/s^2).

Table 1. System parameters

Parameter	Symbol	Value
The length of each shaft part [mm]	L_1	180
	L_2	80
	L_3	80
	L_4	180
The mass of disk 1 [kg]	m_1	20
The mass of disk 2 [kg]	m_2	20
The combined mass of support bearing 1 and its outer ring [kg]	m_{b1}, m_{b2}	4, 4
Disk 1 diameter moment of inertia [kg/m^2]	jd_1	3.5×10^{-2}
Disk 2 diameter moment of inertia [kg/m^2]	jd_2	3.5×10^{-2}
Polar moment of inertia of disk 1 [kg/m^2]	jp_1	7×10^{-2}
Polar moment of inertia of disk 2 [kg/m^2]	jp_1	7×10^{-2}
The supporting damping of the bearing 1 and bearing 2 [N·s/m]	c_{b1}, c_{b2}	2×10^{3}
The supporting stiffness of the bearing 1 and bearing 2 [N/m]	k_{b1}, k_{b2}	2.5×10^{7}
Elastic modulus of shaft [Pa]	E	2.07×10^{11}
material density [kg/m^3]	ρ	7.85×10^{3}
Hertz contact stiffness [N/m]	K_b	7×10^{9}
Number of ball bearings	N_b	13
Clearance between disk and stator [m]	δ	2.5×10^{-5}
Rub-impact stiffness [N/m]	K_o	6.5×10^{7}
Eccentricity of two lumped mass disks [m]	e_1, e_2	2.5×10^{-5}

3.1 Pitching Maneuver Condition (Rub and Without Rub-Impact)

Figure 6 depicts the axial trajectory map of the disk 1 system under various pitching maneuvering loads, comparing the cases with and without rub-impact. Shaft orbits are a critical tool for analyzing rotor dynamic behavior, as they provide a visual representation of the rotor's lateral motion. Regardless of whether the rub-impact is considered, the system exhibits single-periodic motion, indicating that the maneuver load alone does not induce complex nonlinear motion (e.g., quasi-periodic or chaotic motion) under the tested conditions. In the absence of rub-impact, the overall diagram of shaft orbit changes to the top right corner as the pitching maneuver loads rise, however, vibration displacement in the X and Y axes stays

instead similar. In contrast to this conclusion, when the rub-impact is analyzed, the increase in maneuvering load causes disk 1 to increase significantly in the X and Y directions. Nevertheless, the shaft orbit travels to the upper right corner, which is consistent with the no rub-impact case, demonstrating that when subjected to rub-impact, the system's vibration in various directions is magnified, and the vibration displacement in the Y direction is larger.

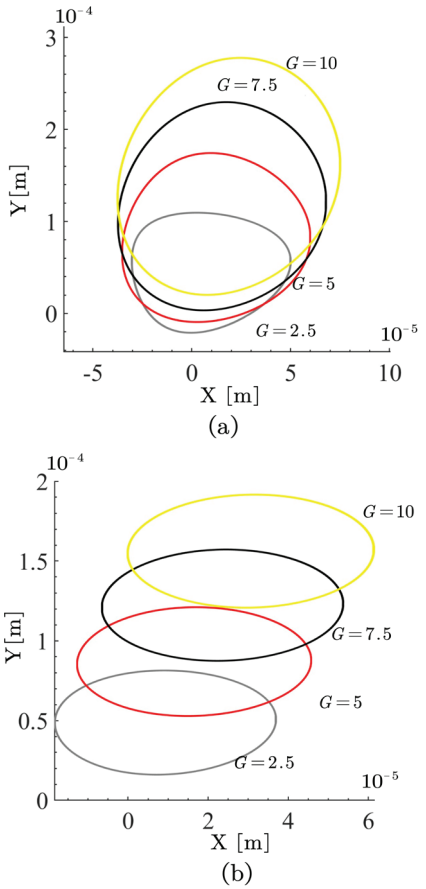

Fig. 6. Shaft orbit diagrams of disk 1 under maneuvering loads in the pitching of aircraft; a) rub impact; b) no rub-impact

Figure 7 displays the results of a fast Fourier transform (FFT) analysis of the vibration of disk 1 (Y direction) under pitching maneuvering loads, revealing significant differences in the frequency spectra between the cases with and without rub-impact. While rub-impact is considered, subharmonic frequency ($0.8f$) and ($0.9f$), and frequency of one-times (f) and two times ($2f$) appear in the spectrum diagram of disc 1, while the one-times frequency and subharmonic frequency ($0.7f$) appear in the spectrum diagram of the disk 1 system with only maneuvering load. In contrast, the one-times frequency of the rub-impact exhibits a greater wave frequency than the no rub-impact. Additionally, as the maneuver load increases, the amplitude of the fundamental frequency increases, which is attributed to the increase in inertial forces that enhance the interaction between the rotor and the stator. Interestingly, as the pitching maneuver load increases, the amplitude of the second harmonic ($2f$) in the spectrogram corresponding to the rub-impact decreases. This phenomenon may be explained by the change in the rub-impact interaction mode: as the load increases, the duration or intensity of the rub-impact may decrease, leading to a reduction in the second harmonic component.

Figure 8 illustrates the Y direction responses of disk 1 under pitching maneuver conditions (G=2), comparing the scenarios with and without rub-impact. In Figure 8a, within the speed range of 500 rad/s to 1300 rad/s, the system undergoes a series of transitions between single-periodic, quasi-periodic, multi-periodic motions. For speeds between 1300 rad/s and 2000 rad/s, the system primarily demonstrates quasi-periodic motion. As the rotational speed further increases, the system undergoes a succession of transitions between single-periodic, multi-periodic and quasi-periodic motions.

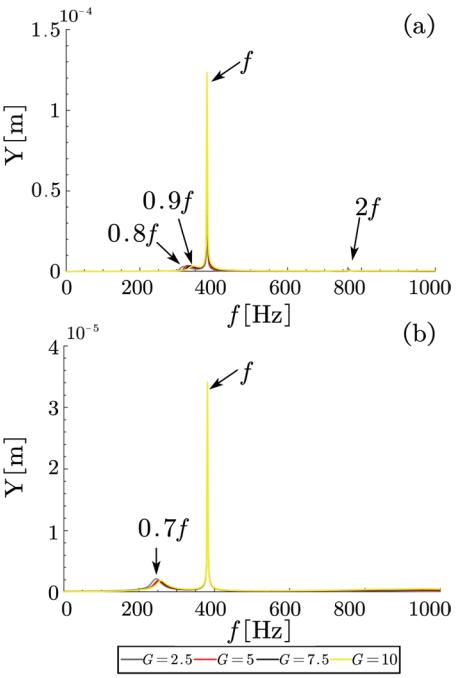

Fig. 7. Disk 1 spectrogram (Y direction) of varied maneuvering loads in the pitching of the aircraft; a) rub-impact, and b) no rub-impact

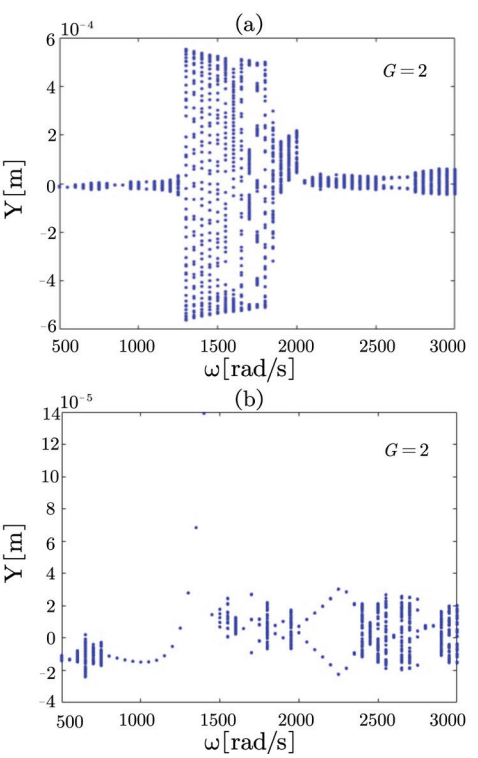

Fig. 8. Bifurcation diagrams of disk 1 in the Y direction under pitching conditions (G = 2); a) rub-impact, and b) no rub-impact

In Figure 8b, between 500 rad/s and 1450 rad/s, the response transitions from quasi-periodic to single-periodic motion. With increasing speed, the system remains quasi-periodic until reaching 1800 rad/s. Within the range of 1800 rad/s to 2350 rad/s, period-doubling bifurcation is observed, and from 2350 rad/s to 3000 rad/s, the motion is predominantly quasi-periodic.

3.2 Rolling Maneuver Condition (Rub and Without Rub-Impact)

Figure 9 depicts the shaft orbits of different loads in a rolling condition. First and foremost, whether or not the influence of rub-impact is addressed, disk 1 mostly exhibits a single period behavior, which is similar to that under pitching maneuvering loads. In the absence of rub-impact, as the rolling load steadily rises, the vibration displacement of each load in the X and Y directions remain relatively constant, but the overall shaft orbit shifts to the bottom right corner. At the same time, it is clear that when the maneuvering load grows, the influence of the rub effect on the X direction displacement increases relative to that absent rub. Furthermore, in the rub-impact diagram, the movement in the X direction expands as the load increases, and the offset path of the shaft orbit motion curve is comparable to that without rub.

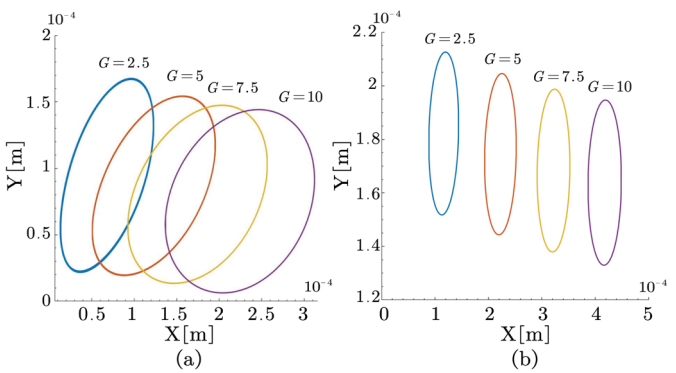

Fig. 9. Shaft orbit diagrams of disk 1 under different maneuvering loads in the rolling of the aircraft; a) rub-impact, and b) no rub-impact

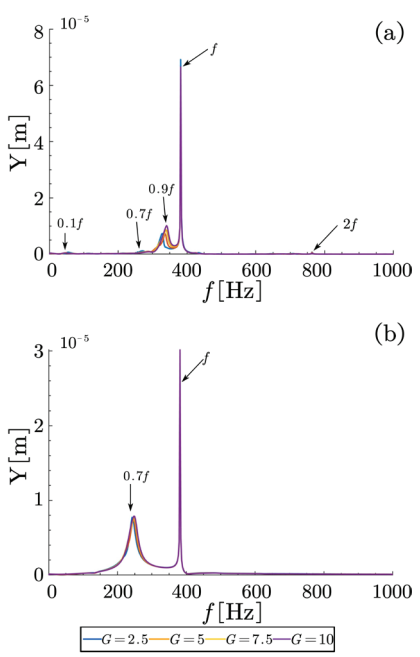

Fig. 10. Disk 1 spectrogram (Y direction) of varied maneuvering loads in the rolling of the aircraft; a) rub-impact, and b) no rub-impact

Figure 10 demonstrates the results of a fast Fourier transform (FFT) examination of rotor vibration under rolling maneuver loads yields considerable spectrum variations (Y direction) with and without rub-impact. When rub-impact is considered, the response of the disk 1 system is composed of the one-times frequency, two-times the frequency, and 3 subharmonic frequencies. It is worth observing that as the load advances, the amplitude of the subharmonic ($0.9f$) increases, but amplitude of the subharmonic ($0.7f$), the amplitudes of the two-times and one-times frequencies drop. In the absence of rub-impact, the disk 1 system's response comprises a one-times frequency and a subharmonic ($0.7f$), with its amplitudes increasing with the load. A comparison of the two figures clearly shows that considering rub-impact introduces additional multiple frequency components and modifies the amplitude distribution of existing frequencies, highlighting the significant influence of rub-impact on the system's frequency characteristics.

Figure 11 illustrates the Y direction responses of disk 1 under rolling maneuver conditions (G = 2), comparing scenarios with and without rub-impact. As depicted in sub-figure a, the system exhibits a complex dynamic evolution as the rotational speed increases. Within the speed range of 500 rad/s to 1200 rad/s, the response transitions from single-periodic to quasi-periodic, followed by a multi-periodic bifurcation and further quasi-periodic motion. The motion remains predominantly quasi-periodic from 1200 rad/s to 1900 rad/s. A window of stable single-periodic motion is observed between 1900 rad/s and 2050 rad/s, beyond which the system reverts to quasi-periodic behavior. In contrast, the dynamics presented in sub-figure b is characterized by alternating quasi-periodic and single-periodic motions in the speed range (500 rad/s to 1500 rad/s). As the speed increases, multi-periodic motion becomes dominant, which is a result of the nonlinearity introduced by the bearing forces and maneuver loads. Finally, within the high-speed range of 2400 rad/s to 3000 rad/s, the system undergoes a transition from quasi-periodic to single-periodic motion before returning to a quasi-periodic state.

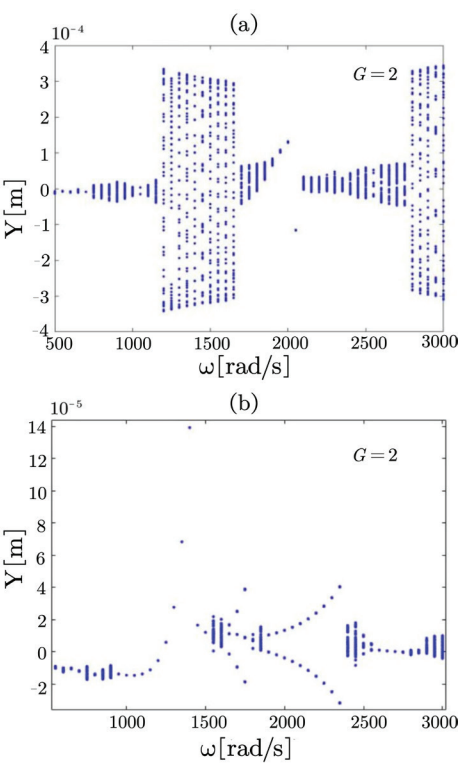

Fig. 11. Bifurcation diagram of disk 1 in the Y direction under rolling conditions (G = 2); a) rub-impact; and b) no rub-impact

3.3 Yawing Maneuver Condition (Rub and Without Rub-Impact)

Figure 12 demonstrates the shaft orbit diagram of disc 1 under yawing attitudes (with various maneuvering loads) with and without the rub-impact. In the absence of the rub-impact, the shaft orbit changes to the upper left as the maneuvering load increases. And the system displays a single period that corresponds to the pitching and rolling findings. Under the influence of rub-impact, as the load increases, the shaft orbit tends to shift to the left, and the vibration displacements in the X and Y directions increase significantly. Moreover, the overall vibration amplitude in the rub-impact case is substantially larger than that in the non-rub-impact case, which is consistent with the observations under pitching and rolling conditions. This consistency indicates that rub-impact has a universal amplifying effect on vibration amplitudes across all three basic flight attitudes.

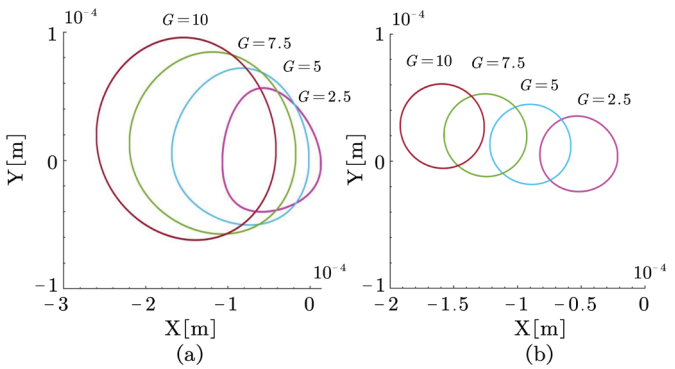

Fig. 12. Shaft orbit diagram of disk 1 under different maneuvering loads in the yawing of the aircraft; a) rub-impact; b) no rub-impact

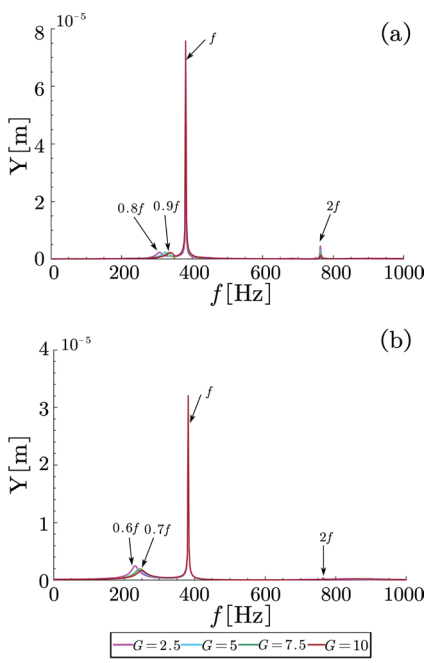

Fig. 13. Spectrogram (Y direction) of disk 1 under different maneuvering loads in the yawing of the aircraft; a) rub-impact; b) no rub-impact

The spectrum diagram (Y direction) of disk 1 with and without the rub-impact is shown in Fig. 13 under yawing flight attitude (various maneuvering loads). In the absence of the rub-impact, the system produces 2 subharmonic frequencies, a two-times frequency and a one-times frequency, which is more comparable to the output when the rub is present. However, it is evident that the amplitudes of one-times and two times frequency when the influence of the rub is taken into account is greater than when it is not. In the non-rub-impact case, the amplitudes of the subharmonic frequencies and the second harmonic decrease as the load increases, which may be due to the change in the system's stiffness or damping characteristics under higher loads, leading to a reduction in nonlinear vibration components.

Fig. 14 depicts the Y direction responses of disk 1 under a yawing maneuver (G = 2), comparing scenarios with and without rub-impact. As shown in Fig. 14a, the system's motion transitions between single-periodic, multi-periodic, and quasi-periodic states within the speed range of 500 rad/s to 1200 rad/s. This is followed by a predominantly quasi-periodic regime that spans from 1200 rad/s to 2100 rad/s, where the system exhibits sustained complex motion. A subsequent transition to single-periodic motion occurs at higher speeds, before a final shift back to quasi-periodic motion at 2450 rad/s. Conversely, the dynamics in Fig. 14b are characterized by a transition from quasi-periodic to single-periodic motion at low speeds (500 rad/s to 1450 rad/s). A quasi-periodic regime is observed between 1500 rad/s and 1900 rad/s, after which multi-periodic motion dominates until 2300 rad/s. Finally, the system settles into a persistent quasi-periodic motion from 2300 rad/s to 3000 rad/s.

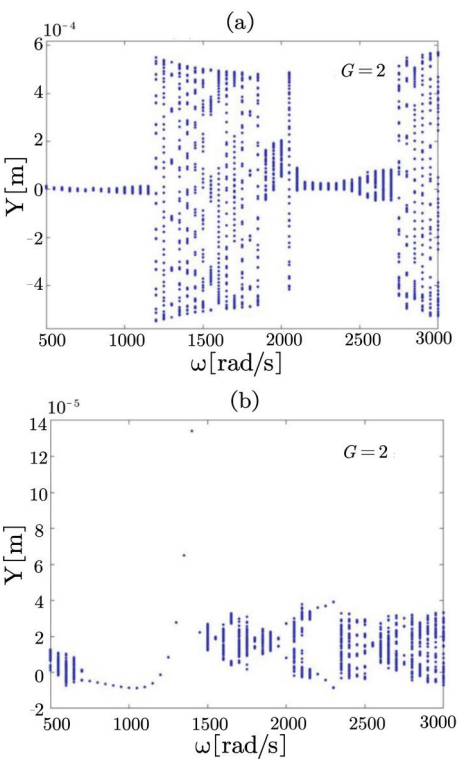

Fig. 14. Bifurcation diagram of disk 1 in the Y direction under yawing conditions (G = 2); a) rub-impact; b) no rub-impact

3.4 Pitching, Rolling and Yawing Maneuver Condition (Only Rub-Impact)

Figure 15 depicts the shaft orbits of three maneuvering loads in the disk 1 system under varying loads and rub factors. With increasing load, the amplitude of the yawing attitude in the X direction exhibits a more pronounced influence compared to those of the pitching and rolling attitudes. As the load increases, the displacement in the Y direction under pitching continues to grow, surpassing that of both yawing and rolling at G=5. Furthermore, a comparative analysis reveals that under lower load conditions (G=2.5), the rolling attitude contributes significantly to the vibration amplitudes in both the X and

Y directions. However, with further increase in load, its influence is exceeded by those of the yawing and pitching motions.

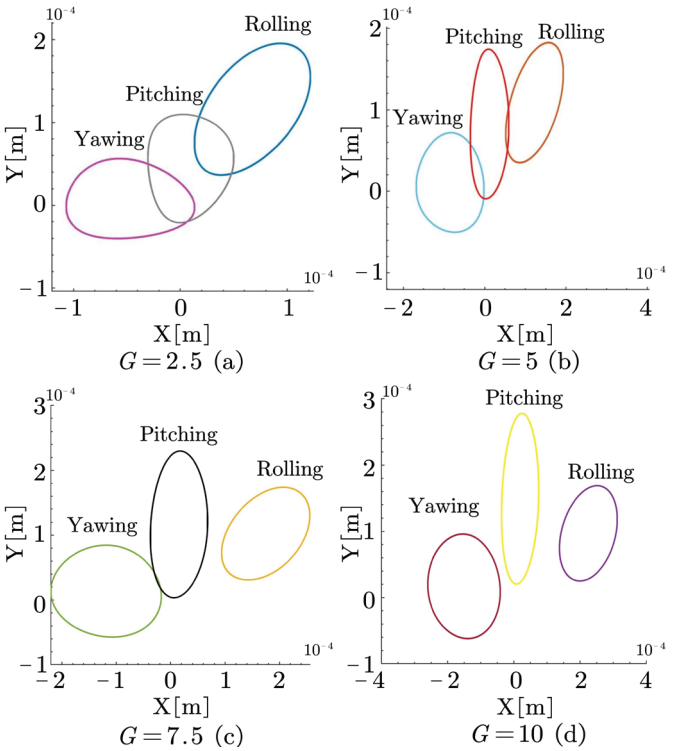

Fig. 15. Shaft orbit diagrams of disk 1 under different flight postures under different maneuvering loads; a) G = 2.5, b) G = 5, c) G = 7.5, and d) G = 10

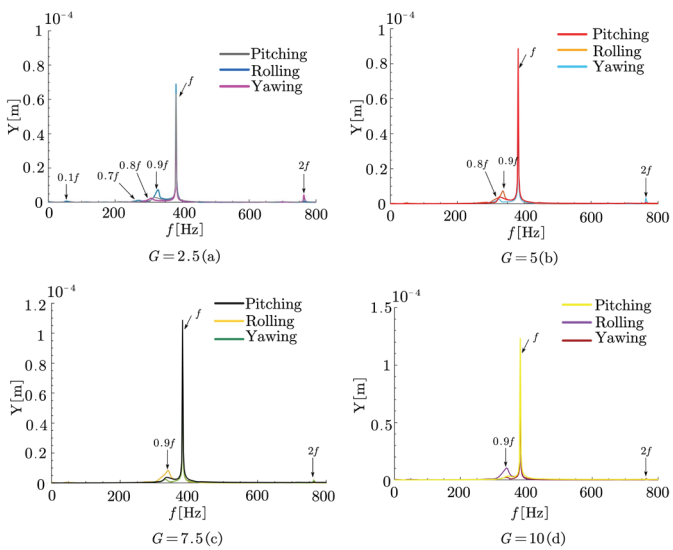

Fig. 16. Spectrogram (Y direction) of disk 1 in different flight postures under different maneuvering loads; a) G = 2.5, b) G = 5, c) G = 7.5, d) G = 10

The spectrum diagram of the Y direction for the disk 1 system under three different flight modes and various maneuvering loads, with rub-impact considered, is presented in Fig. 16. Based on the comparison, the pitching attitude produces the highest ($1f$) amplitude under all four loads. The rolling attitude consistently generates larger ($0.9f$) subharmonic amplitudes than the other attitudes, suggesting that rolling-induced rub-impact has a unique effect on the generation of this subharmonic component. In contrast, the yawing attitude yields the strongest components of the second harmonic ($2f$), highlighting that yawing maneuvers favor the generation of higher harmonic components under rub-impact

Under the coupling of fixed load G=2 and three flight attitudes (pitching, rolling, and yawing) with increasing speed, the disk 1 system's bifurcation diagram (Y direction) is displayed in Fig. 17. First, the three flying circumstances exhibit single-, multi-, and quasi-periodic motion, as well as comparatively rich periodic motion characteristics, and all of them exhibit strong nonlinear characteristics. And then, the most frequent alternation between periodic regimes is observed under pitching conditions.

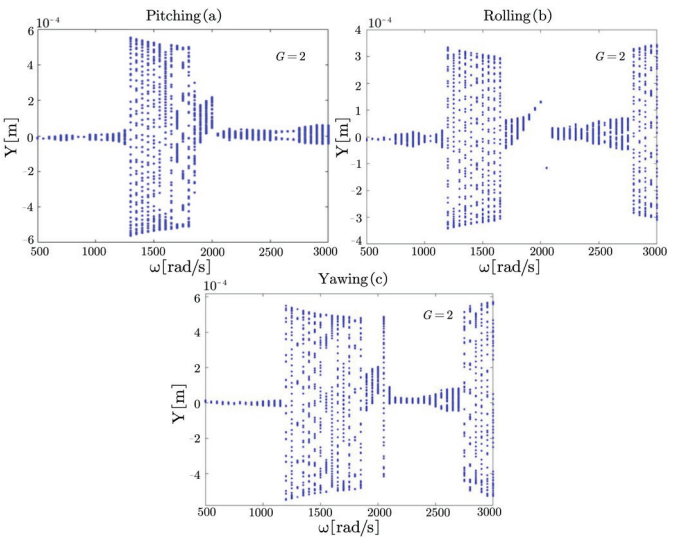

Fig. 17. Bifurcation diagram of disk 1 maneuvering loads in Y direction; at a) pitching, b) rolling, and c) yawing conditions

4 CONCLUSION

This study conducts a comprehensive comparative analysis of the dynamic behavior of an aero-engine dual-rotor system under three typical flight attitudes (pitching, rolling, and yawing) with different maneuver loads. The dynamic characteristics of the rub-impact versus the normal condition are examined under three different flight modes and various loads. Furthermore, the dynamic behavior among the three flight modes under dual-disk rubbing conditions is compared. Several notable phenomena with significant theoretical and practical implications are revealed, providing valuable insights for the design, vibration control, and failure analysis of fighter engine rotor systems.

1. According to the comparison, regardless of flight modes and related maneuvering load circumstances, vibration amplitudes in both the X and Y directions in orbit diagrams under dual-disk rub-impact faults constantly surpass those under non-rub conditions. Furthermore, spectrum graphs show much more varied frequency components during dual-disk rub-impact occurrences. Additionally, the bifurcation diagrams demonstrate that as the rotational speed increases, the vibration amplitudes under dual-disk rub-impact faults remain significantly higher than those under non-rub conditions across all flight modes and fixed loads. This indicates that the rub-impact not only amplifies vibration amplitudes but also sustains this amplification over a wide range of rotational speeds, posing a persistent threat to engine safety.
2. Under the coupled conditions of varying flight attitudes and dual-disk rub-impact faults, orbit diagrams show that pitching maneuvers (G=2.5, G=5 and G=7.5) have systematically higher vibration amplitudes in the Y direction than other flight attitudes, whereas yawing maneuvers have superior vibration amplitudes in the X direction. Across all three flight attitudes, the spectrograms under the G=2.5 condition exhibit more types of frequency com-

ponents with significant amplitudes compared to other maneuver loads, indicating that moderate maneuver loads create an optimal environment for the generation of complex nonlinear frequency components under the rub-impact. Furthermore, bifurcation diagrams show that the most frequent alternation between periodic regimes is observed under pitching conditions ($G = 2$ with rub-impact).

References

[1] Liang, C., Suo, D., Sun, M. A review on the key technologies of the sixth generation fighter engines in the us. *Aeroengine* 42 93-97 (2016).

[2] Sakata, M., Kimura, K., Park, S., Ohnabe, H. Vibration of bladed flexible rotor due to gyroscopic moment. *J Sound Vib* 131 (1989) 417-430 **DOI:10.1016/0022-460X(89)91002-X**.

[3] Sakata, M., Kimura, K., Okamoto, S., Oikawa, K. Vibration analysis of a high speed and light weight rotor system subjected to a pitching or turning motion: I: A rigid rotor system on flexible suspensions. *J Sound Vib* 184871-184885 (1995) **DOI:10.1006/jsvi.1995.0350**.

[4] Wei, H., Fan, X. Vibration response analysis of two-rotor systems in maneuvering flight. *Proc Conf Aeroengine Struct Strength Vib Chin Soc Aeronaut* 315-320 (2001).

[5] Zhu, C., Chen, Y. General dynamic model of aeroengine's rotor system during maneuvering flight. *J Aerosp Power* 24 371-377 (2009). (in Chinese)

[6] Hou, L., Chen, Y. Dynamical simulation and load control of a Jeffcott rotor system in Herbst maneuvering flight. *J Vib Control* 22 412-425 (2016) **DOI:10.1177/1077546314533138**.

[7] Han, Q., Chu, F. Dynamic response of cracked rotor-bearing system under time-dependent base movements. *J Sound Vib* 332 6847-6870 (2013) **DOI:10.1016/j.jsv.2013.07.025**.

[8] Chen, L., Wang, J., Han, Q., Chu, F. Nonlinear dynamic modeling of a simple flexible rotor system subjected to time-variable base motions. *J Sound Vib* 404 58-83 (2017) **DOI:10.1016/j.jsv.2017.05.032**.

[9] Kun, G., Xiuli, S., Yuanyuan, X., Haitao, L., Zhang, H. Initial research on impacts of maneuver loads on core engine tip clearance. *J Aerosp Power* 33 (2018) 2205-2218. (in Chinese)

[10] Pan, W., Ling, L., Qu, H., Wang, M. Coupling dynamic behavior of aero-engine rotor system caused by rolling, pitching and yawing maneuver loads. *Appl Math Model* 102 726-747 (2022) **DOI:10.1016/j.apm.2021.10.021**.

[11] Saeed, N.A., Awwad, E.M., Maarouf, A., Farh, H.M.H., Alturki, F.A., Awrejcewicz, J. Rub-impact force induces periodic, quasiperiodic, and chaotic motions of a controlled asymmetric rotor system. *Shock Vib* 2021 1800022 (2021) **DOI:10.1155/2021/1800022**.

[12] Wu, Z., Hao, L., Zhao, W., Ma, Y., Bai, S., Zhao, Q. Modeling and vibration analysis of an aero-engine dual-rotor-support-casing system with inter-shaft rub-impact. *Int J Non-Linear Mech* 165 104757 (2024) **DOI:10.2139/ssrn.4775226**.

[13] Prabith, K., Krishna, I.P. The stability analysis of a two-spool rotor system undergoing rub-impact. *Nonlinear Dyn* 104 941-969 (2021) **DOI:10.1007/s11071-021-06370-x**.

[14] Pan, W., Li, X., Ling, L., Qu, H. Dynamic modeling and response analysis of rub-impact rotor system with squeeze film damper under maneuvering load. *Appl Math Model* 114 544-582 (2023) **DOI:10.1016/j.apm.2022.10.021**.

[15] Lin, J., Wu, B., Lu, X., Xu, J., Zhang, J., Dai, H. Numerical simulation of aero-engine rotor-blade-coating coupling system with rub-impact fault and its dynamic response. *Proc Int Conf Rotor Dyn* 56-75 (2023) **DOI:10.1007/978-3-031-40459-7_4**.

[16] Sousa, M.S., Cavallini, A.A., Steffen, V., Briend, Y., Chatelet, E., Dufour, R. Numerical and experimental investigation of rubbing existence in the context of a rotating machine under base excitation. *J Vib Acoust* 147 041001 (2025) **DOI:10.1115/1.4068108**.

[17] Yu, P., Chen, G., Li, L. Modal analysis strategy and nonlinear dynamic characteristics of complicated aero-engine dual-rotor system with rub-impact. *Chin J Aeronaut* 35 184-203 (2022) **DOI:10.1115/1.4068108**.

[18] Yu, P., Guo, C., Cun, W., Mohan, Y. Modal characteristics and calculation method for flexible rotor system with rubbing constraint. *Acta Aeronaut Astronaut Sin* 41 224029-224029 (2020) **DOI:10.1016/j.cja.2020.10.031**.

[19] Fei, Z. *Research on finite element modeling and dynamic behaviors of complex multi-rotor coupled systems*, PhD Thesis. J Zhejiang Uni, Zhejiang (2013).

[20] Cheng, M., Meng, G., Wu, B. Nonlinear dynamics of a rotor-ball bearing system with Alford force. *J Vib Control* 18 17-27 (2012) **DOI:10.1177/1077546311405701**.

[21] Zhang, X., Yang, Y., Ma, H., Shi, M., Wang, P. A novel diagnosis indicator for rub-impact of rotor system via energy method. *Mech Syst Signal Process* 185 109825 (2023) **DOI:10.1016/j.ymssp.2022.109825**.

Received: 2025-06-09, revised: 2025-08-26, accepted: 2025-10-01 *as Original Scientific Paper.*

Data availability *The data supporting the study's findings are included in the paper.*

Author contribution *Peixun Tang: Data curation, Writing – original draft, Writing – review & editing; Peixun Tang: Formal analysis; Xiaojing Ma: Formal analysis; Xi Liu: Formal analysis; Peixun Tang: Validation; Zhengminqing Li: Validation.*

Dinamika dvorotorskih sistemov letalskih motorjev pri različnih letalnih položajih in sočasnih torno-udarnih stikih

Povzetek *Letala z visoko okretnostjo povzročajo izjemne obremenitve letalskih motorjev, kar lahko sproži uničujoče trke med rotorjem in statorjem ter tako predstavlja resno grožnjo varnosti leta. V tej študiji je bil vzpostavljen model rotorja z ležaji in diski s štirimi prostostnimi stopnjami za sistem z dvema diskoma, posebej zasnovan za simulacijo sklopljenih učinkov sočasnih trkov med rotorjem in statorjem obremenitvah v manevrih. Za primerjavo je bil izdelan tudi referenčni model brez trkov. Rešitve za oba modela so bile pridobljene z metodo Newmark-β. Za oceno vpliva manevrskih obremenitev na dinamične značilnosti sistema je bila izvedena parametrična analiza učinkov hkratnih trkov obeh diskov pri treh ključnih letalnih načinih – valjanju (rolling), nagibanju (pitching) in smernem zasuku (yawing). Raziskava ponuja pomembno teoretično osnovo za izboljšanje nadzora vibracij in izvedbo analiz odpovedi pri zasnovi motorjev bojnih letal ter tako prispeva k razvoju varnejših in zanesljivejših rotorskih sistemov.*

Ključne besede *dinamika rotorja, manevrski let, nelinearna ležajna sila, torno-udarni stik, nelinearne karakteristike*

Contents

9 770039 248001
ISSN 0039-2480

https://www.sv-jme.eu/